CHEMICAL SENSING EMPLOYING pH SENSITIVE EMERALDINE BASE THIN FILM FOR CARBON DIOXIDE DETECTION

Except where reference is made to the work of others, the work described in this dissertation is my own or was done in collaboration with my advisory committee. This dissertation does not include proprietary or classified information.

_____
Mihai Irimia-Vladu

Certificate of Approval:

_____
Aleksandr L. Simonian
Associate Professor
Mechanical Engineering Department
Auburn University

_____
Jeffrey W. Fergus, Chair
Associate Professor
Mechanical Engineering Department
Auburn University

_____
ZhongYang Cheng
Assistant Professor
Mechanical Engineering Department
Auburn University

_____
Curtis G. Shannon
Professor
Chemistry Department
Auburn University

_____
Stephen L. McFarland
Acting Dean
Graduate School

CHEMICAL SENSING EMPLOYING pH SENSITIVE EMERALDINE BASE THIN FILM FOR CARBON DIOXIDE DETECTION

Mihai Irimia-Vladu

A Dissertation

Submitted to

the Graduate Faculty of

Auburn University

in Partial Fulfillment of the

Requirements for the

Degree of

Doctor of Philosophy

Auburn, Alabama
August 7, 2006

CHEMICAL SENSING EMPLOYING pH SENSITIVE EMERALDINE BASE THIN FILM FOR CARBON DIOXIDE DETECTION

Mihai Irimia-Vladu

Permission is granted to Auburn University to make copies of this dissertation at its discretion, upon request of individuals or institutions and at their expense.
The author reserves all publication rights.

_____
Signature of Author

_____
Date

DISSERTATION ABSTRACT

CHEMICAL SENSING EMPLOYING pH SENSITIVE EMERALDINE BASE THIN FILM FOR CARBON DIOXIDE DETECTION

Mihai Irimia-Vladu

Doctor of Philosophy, August 7, 2006
(B.S. University of Craiova, Romania, 1997)

194 Typed Pages

Directed by Jeffrey W. Fergus

Respiration, or CO_2 evolution, is a universal indicator for all the biological activities. Among many potential applications, the measurement of CO_2 evolution has been found to be a rapid and nondestructive means for examining microbial contamination of food.

The sensor developed in this work consists of a thin emeraldine base-polyaniline (EB-PAni) film. In the first half of the project the effect of carbon dioxide over the conductivity of a composite film of emeraldine base polyaniline and poly(vinyl alcohol) in N-methyl pyrrolidone (NMP) respectively was tested. Argon gas or mixture of argon and 5% CO_2 were circulated through the glass cell containing the polymer film deposited on interdigitated electrode and exposed to specific humidity levels fixed by aqueous supersaturated salt solutions. In the second half of the project, a thin emeraldine base film

in NMP was directly deposited on interdigitated electrode and the respective sensor inserted in water. Carbonic acid solutions of various pHs were generated by bubbling specific mixtures of carbon dioxide and argon. Conductivity measurements were performed by impedance spectroscopy throughout the project. The sensing mechanism is based on intermediate stages of the transformation of the emeraldine base polyaniline to a conductive salt type (ES-PAni). This EB-ES transformation is the consequence of the exposure of EB-PAni to a protonic acid and is accompanied by a change in the conductivity of the polymer film. Carbonic acid, unfortunately, is a very weak acid and is unable to induce a conductivity change, but the intermediate steps that predetermine this transformation are detected by impedance spectroscopy even when the overall conductivity of the film is unchanged.

The composite thin film developed in the first part of the project showed poor sensing characteristics: limited dynamic range, drift, instability and slow time response. However, the sensor design employed in the second half of this work, coupled with impedance spectroscopy measurements, revealed valuable information about conduction mechanisms at pH levels were the overall conductivity of the film remained unchanged.

Typical impedance spectra for the emeraldine thin films for a frequency sweep between 3.2 E7 to 1 Hz shows a single semicircle. The overall conductivity of the film (5×10^{-4} S/cm) does not change when CO_2 is bubbled through the water in which the sensor is immersed, but an additional semicircle starts to appear at low (less than 200 Hz) frequency corresponding to lowering the pH of the solution below 5.0. The original semicircle diminishes in size but maintains its initial peak frequency. The EB film is very sensitive to pH changes, therefore an additional semicircle appears in unpurified argon

gas due to the reduction of the pH of water solution to 4.65. The same mechanism is displayed in hydrochloric acid solutions of various pH. The formation of the second semicircle depends on the initial conductivity of the emeraldine base film, a film displaying an initial conductivity of 4.8×10^{-3} S/cm forming the second semicircle at a pH of 5.85. The appearance of the second semicircle is most likely due to a preferential protonation in the insulating matrix of the polymer film. The overall conductivity of the film increases when the level of protonation in the insulating portion of the film reached a level close to the protonation level in the scattered metallic islands, allowing the electron-hopping mechanism to became active.

The sensor output is stable and reproducible even after 11 months passed from the polymer film deposition.

ACKNOWLEDGEMENTS

The author expresses his gratefulness to Dr. Jeffrey W. Fergus for all his academic guidance, help and encouragement for the pursuit of this degree.

The author also likes to convey thanks to Dr. Zhong. Y. Cheng, Dr. Aleksandr Simonian, Dr. Curtis Shannon and Dr. Eric Bakker for many insightful suggestions and kind help.

Acknowledgements are due to Mr. Roy Howard and Ms. Shirley Lyles for their unconditional support and patience, and to all the friends and colleagues who assisted the author in various ways during his years of studies.

Most importantly, the author pays tribute to his wife, Marina for her encouragement and continuous support throughout his education, to his son, Cristian for bringing happiness in his family life, and to his parents, grandparents and in-laws for help and continuous support.

Finally, the author would like to acknowledge the financial support of this work from the Materials Research and Education Center.

Style manual or journal used:
Synthetic Metals

Computer Software used:
Microsoft Word, Microsoft Excel, DataThief

TABLE OF CONTENTS

LIST OF FIGURES xi
LIST OF TABLES xiv
1. INTRODUCTION AND RESEARCH OBJECTIVES 1
1.1. Safety Issues Faced in Food Chain Industry 1
1.2. Carbon Dioxide Evolution Rate Measurement 2
1.3. Classification of CO_2 Sensors 3
1.3.1. Electrochemical Techniques 3
1.3.1.1. Potentiometric Type CO_2 Sensors: Description 3
1.3.1.2. Amperometric Type CO_2 Sensors 16
1.3.1.2.1. Reducing Specie; Electrode Material 18
1.3.1.2.2. Gas Permeable Membrane 20
1.3.1.2.3. Electron Transfer Studies 24
1.3.1.2.4. Reduction of O_2 and CO_2 at Micro-electrodes 25
1.3.1.2.5. Characteristic Values Reported 26
1.3.1.2.6. Conclusions 27
1.3.1.3. Conductometric Type CO_2 Sensors 27
1.3.1.4. Coulometric Type CO_2 Sensors 30
1.3.2. Spectroscopic Techniques 34
1.3.3. Other Methods of Detection 37
1.4. Conductive Polymers as Carbon Dioxide Sensors 39
1.4.1. Conductive Polymers: Description 39
1.4.2. Insulator to Metal Transition Process 40
1.4.3. Polyaniline: Description 43
1.5. Impedance Spectroscopy: Description 58
1.6. Project Objective 63
2. EXPERIMENTAL SECTION 64
2.1. Suspended Sensor 64
2.1.1. Conductive Polymer Preparation 64
2.1.2. Polymer Film Deposition and Interrogation 66
2.1.3. Experimental Setup 67

2.1.4. Experimental Conditions for Material Analysis 69
2.2. Immersed Sensor 72
2.2.1. Conductive Polymer Preparation 72
2.2.2. Polymer Film Deposition and Interrogation 72
2.2.3. Experimental Setup 73
2.2.4. Measurement Conditions 74
3. RESULTS AND DISCUSSION 77
3.1. Suspended Sensor 77
3.1.1. Experimental Results 77
3.1.2. Sensor Performance Evaluation 86
3.1.3. Comparative Results 87
3.1.4. Materials Characterization 89
3.1.4.1. FTIR Spectroscopy Characterization 89
3.1.4.2. Differential Scanning Calorimetry Characterization 95
3.1.4.3. X-Ray Diffraction Characterization 96
3.1.4.4. UV-Visible Spectrophotometry Characterization 100
3.1.4.5. Materials Characterization Discussion 101
3.1.5. Possible Explanations for Poor Performance 103
3.1.5.1. Tautomerism 103
3.1.5.2. Limited Protonation in Emeraldine Base 105
3.1.5.3. Limited Amount of Water in PVA Matrix 107
3.2. Immersed Sensor 109
3.2.1. Experimental Results 109
3.2.1.1. Conductivity Response in Hydrochloric Acid Solutions 111
3.2.1.2. Conductivity Response in Carbonic Acid Solutions 122
3.2.2. Complexation Effect Study 126
3.2.3. Response of the Sensor in Ar-CO_2 mixtures 132
3.2.4. Conclusions 138
4. FUTURE WORK 140
5. REFERENCES 142
6. APPENDIX 162

LIST OF FIGURES

Figure 1. First generation Severinghaus type carbon dioxide sensor. 5
Figure 2. Miniaturized version of the Severinghaus-type CO_2 sensor employing liquid ion exchange membrane. 9
Figure 3. Iridium oxide tip miniaturized Severinghaus type CO_2 sensor. 14
Figure 4. Sensing concept of the amperometric CO_2 sensor. 18
Figure 5. Schematic of the electrical diagram for ISFET. 30
Figure 6. Schematic of the coulometric carbon dioxide sensor. 31
Figure 7. Oxidation of a fully reduced aniline repeat unit. 44
Figure 8. Polyaniline in various oxidation states. 46
Figure 9. The resonance-stabilized form of the emeraldine salt polymer. 48
Figure 10. Protonation induced charge unpairing in polyaniline. The counterion display is omitted from the schematic. 50
Figure 11. Self doping of emeraldine base. 51
Figure 12. a) Schematic representation of the acid-base and redox reactions between different forms of polyaniline; b) Thermodynamical stability domains of the pH for the different forms of polyaniline. 56
Figure 13. Impedance plotted as a planar vector using rectangular and polar coordinates. 59
Figure 14. The sketch of the interdigitated electrode. 66
Figure 15. The setup utilized in conductivity measurements for suspended sensor. 67
Figure 16. The equivalent circuit schematic associated with the measured data in the suspended sensor case; This circuit will also be employed in the immersed sensor case. 69
Figure 17. Experimental setup for the conductivity measurements in the immersed sensor case. 73
Figure 18. Equivalent circuit schematic for the immersed sensor case. 74
Figure 19. The CO_2 detection mechanism. 77
Figure 20. Impedance spectra recorded by Impedance Gain Phase Analyzer 78
Figure 21. Resistance of the composite film in Ar and Ar + 5% CO_2 in a fixed humidity level of RH ~ 30% (cycle 1 in Table 4). 80
Figure 22. Trend of the resistance response of the composite film in Ar and Ar + 5% CO_2 at a fixed humidity level of ~ 30%. 81
Figure 23. Logarithm of resistance versus relative humidity in argon and Ar + 5% CO_2 for the composite polymeric film. The film was tested more than once in both magnesium and sodium chloride respectively. Each particular cycle was circled for the ease of visualization. 82
Figure 24. Resistance difference between Ar and Ar + 5% CO_2 (logarithmic scale). 83
Figure 25. Response time (t_{90}) reached by the composite film for ~60% RH (cycle 2 in Table 4). 84

Figure 26. Comparison between FTIR spectra of emeraldine base without heat treatment and heat treated at various temperatures for 1 hour in helium atmosphere. 90
Figure 27. Schematic of crosslinking process. 92
Figure 28. DSC thermogram of emeraldine base held isothermal for 30 minutes at 100ºC and ramped up 20ºC/min to 400ºC. 96
Figure 29. X-ray diffraction of emeraldine base treated at various temperatures. 97
Figure 30. UV-Visible spectrum of emeraldine base samples treated for one hour at various temperatures in helium atmosphere. 101
Figure 31. Schematic of the tautomerism process 105
Figure 32. Doping percentage as a function of pH of protonating solution for the class I of emeraldine base 106
Figure 33. Percent water absorbed in poly (vinyl alcohol)-NMP plasticized film, at various humidity levels. 108
Figure 34. Impedance spectra in pure water and water where pure CO_2 was bubbled. .. 110
Figure 35. Total resistance of emeraldine base thin film vs. pH in aqueous HCl solutions. 111
Figure 36. Comparison of the conductivity responses as a function of pH for the two classes of emeraldine base: the EB-I reported by MacDiarmid [161] and the EB-II employed in the current project. 113
Figure 37. Comparison of the doping percentage vs. pH responses for the two classes of emeraldine base reported in the literature: MacDiarmid [161] and Jozefowicz [234]; The data points shown on the graph belong to MacDiarmid, being reproduced by DataThief software close to the one originally published. 114
Figure 38. The formation and evolution of the second semicircle with variation of pH level. 115
Figure 39. Appearance of the second semicircle as a horizontal line at pH=5.03 and its subsequent evolution with decreasing pH level. 115
Figure 40. Resistance variation of the NMP-plasticized emeraldine base thin film with time at different pH levels, showing the onset of conductivity change at pH = 2.25. 116
Figure 41. Titration curve of hydrochloric acid in water and resistance response ($R_{high\ frequency}$) of the emeraldine film as a function of hydrochloric acid concentration. 117
Figure 42. Capacitance as a function of pH associated with the sensor response in hydrochloric acid. 118
Figure 43. Capacitance vs. square root of time for the emeraldine base thin film equilibrated for various times in pH = 1.75 119
Figure 44: Capacitance vs. square root of time for the emeraldine base thin film equilibrated for various times in pH = 1.11 120
Figure 45. Impedance as a function of pH of hydrochloric acid solution for two fixed frequencies. 121
Figure 46. Sensor resistance in alternating cycles involving alternating bubbling of CO_2, purified and unpurified Ar through water. Graph labels:

"H_2O"- pure water exposed to room atmosphere air, "CO_2", "Ar purified" and "Ar-unpurified"- bubbling of respective gas in pure water. The equivalent circuit model gives the data points on graph. 123
Figure 47. Sensor resistance in alternating cycles involving alternating bubbling of CO_2, purified and unpurified Ar through water. Graph labels: "H_2O"- pure water exposed to room atmosphere air, "CO_2", "Ar purified" and "Ar-unpurified"- bubbling of respective gas in pure water. The geometrical intercept gives the data points on graph. 125
Figure 48. Sensor resistance as a function of pH, in alternating cycles involving alternating bubbling of CO_2, purified and unpurified Ar through water. 126
Figure 49. FTIR spectrum of the dried emeraldine base thin film. 128
Figure 50. Comparison of the FTIR spectra between the dried film and the film immersed for 10 minutes in carbonic acid solution of pH = 3.95. 129
Figure 51. Comparison of the FTIR spectra for emeraldine base treated in HCl solution of pH = 3.88 and 1.75. 130
Figure 52. FTIR spectrum of the EB film treated in pH = 1.11. 131
Figure 53. Comparison of the FTIR spectra between the films equilibrated in water and in carbonic acid solution of pH = 3.95 for 10 minutes. The spectra is recorded after the acid-base treatment of the film was accomplished. 132
Figure 54. Resistance of emeraldine base thin film as a function of pH of carbonic acid, generated through bubbling of various mixtures of carbon dioxide and argon in deionized water. 134
Figure 55. The appearance of the second semicircle at a pH of 5.85, generated by bubbling a mixture of Ar-0.015% CO_2 for 30 minutes in pure deionized water 135
Figure 56. The high frequency resistance of the emeraldine thin film as a function of carbon dioxide concentration in Ar-CO_2 mixture (black) and pH response of solution to bubbling carbon dioxide (red) 136
Figure 57. Impedance of emeraldine base thin film for two fixed frequencies as a function of carbon dioxide concentration in argon-CO_2 mixture; a correlation between the carbon dioxide concentration and pH generated in pure water is displayed in Figure 56. 137

LIST OF TABLES

Table 1. Reduction elements and cathode materials employed in amperometric CO_2 sensors design. 20
Table 2. Conductivity increase produced by an increase in relative humidity for emeraldine base sample equilibrated at pH = 6.0; *For the sample whose conductivity increased by several orders of magnitude the author, W.R. Salanek estimated that a response was governed by the preparation procedure which allowed for virtually removal of all the water during the dynamic pumping. The latter data represented a personal communication of W.R. Salanek to the authors of reference [192]. 54
Table 3. Alternative methods of fabrication employed. 8, 12, 24 represent the polymerization time (hours); the numbers in regular type indicates air and bold type indicates N_2; *-indicates that PVA with two different molecular weights (13000-23000 or 89000-98000) were used; **- indicates that PVA with three different molecular weights (13000-23000, 89000-98000 or 124-186000) were used. 65
Table 4. Measured values for the suspended sensor. 79
Table 5. Characteristic peaks and vibrational modes assigned to emeraldine base 91
Table 6. Full width at half maxima and peak half width over peak height for emeraldine base samples heat-treated at various temperatures. 98

1. INTRODUCTION AND RESEARCH OBJECTIVES

1.1. Safety Issues Faced in Food Chain Industry

The current research represents a part of a project developed by Auburn University to respond to the problems that arise in the U.S. food supply chain. The science and engineering developed through integration of sensor and information technologies will help accurately and rapidly identify and characterize the nature of the food contamination. The envisioned integrated system is expected to deliver information not only for the detection of real-time contamination (*e.g.* bacterial, chemical and surface) but also for the traceability and inventory of the product (time-temperature control).

The food industry currently relies upon end-product testing for bacterial measurements. This consists of laboratory analysis of a sample taken from the production line, having the shortest time necessary for the identification of microbial contamination of six hours. The severity of microbial contamination, providing an answer to whether the food is suitable for consumption is assessed after 48 hours of laboratory analysis. This lengthy time interval is necessary to multiply the number of bacteria to detectable levels of 10^4-10^8 colony forming units/ml [1,2]. During this two-day interval, millions of pounds of infested food products have been already distributed, sold and consumed without the problem being even detected. The most needed piece of information to the food industry is when, where and how the problem occurs. The sooner the problem

source is identified, the prompter is the action taken, the less is the product waste and the safer is the food distributed to consumers.

1.2. Carbon Dioxide Evolution Rate Measurement

Respiration or CO_2 evolution represents a universal indicator for all biological activities, rendering the determination of CO_2 evolution rate a useful indicator for most of the biological activities. The determination of CO_2 evolution rate has been used over the years for the evaluation of living microbial biomass in soils [3,4], pesticide damage on soil microorganisms [5], decomposition of leaf litter [6], toxic effect of trace metals on microbial populations [7,8], detection of microorganisms in blood cultures and specimens and examination of contaminated bottled juices [9,10].

Precise and rapid determination of microbial contamination in packaged food is often necessary for food sample analysis. The most widely employed technique for the evaluation of microbial contamination of food is the total plate count (TPC), a lengthy method that requires at least 48 hours to produce the results [11,12]. Alternatively, the CO_2 evolution rate, which is correlated with the real time microbial activity of contaminated food, was determined with a commercial IR-CO_2 analyzer, [13,14] and with a microrespirometer [15]. The results of the latter methods have showed a good correlation with the values provided by the conventional TPC method through the cultural and sensory scores. Nevertheless, in spite of a very good correlation with published data, both system are inadequate for miniaturization.

1.3. Classification of CO_2 Sensors

1.3.1. Electrochemical Techniques

The electrochemical detection of carbon dioxide comprises potentiometric, amperometric, conductometric, capacitive and coulometric techniques. A further classification can be done according to the absorption place of carbon dioxide: in a solid or in a liquid material. However, the amperometric, potentiometric and conductometric electrochemical techniques involving absorption in solid ceramic materials require a high operating temperature, in the range of 300-1100°C [16,17] and do not represent therefore a competitor for the room temperature carbon dioxide detection sought in the present project.

Therefore, under this section will be discussed just the liquid based carbon dioxide sensors since they work at room temperature and represent a reason for comparison with the emeraldine base carbon dioxide sensor developed herein.

1.3.1.1. Potentiometric Type CO_2 Sensors: Description

The first attempt to build a carbon dioxide sensor based on a liquid electrolyte was made by Stow *et al.* [18] in 1957, but an improved version of the sensor was proposed by Severinghaus *et al.* [19] one year later. Following this discovery, other reports of improved function sensors working on Severinghaus principle occurred over the years [19,20-31]. In the potentiometric mode, a voltage corresponding to the desired chemical concentration or activity (*i.e.* in this case p_{CO2}) is measured with the sensitivity of the potentiometric sensors governed by the Nernst equation (*i.e.* equation (1) below):

$$E = \frac{RT}{nF} \ln \frac{p_{CO_2}^{\ I}}{p_{CO_2}^{\ II}} \quad (1)$$

where: E is the actual reversible potential of the electrode measured in volts; n is the charge number of the electrode reaction; F is Faraday constant (*i.e*. 96500C/mole); R = 8.314 J/mole×K is universal gas constant; T is the absolute temperature in Kelvin; p_{CO2}^{I} and p_{CO2}^{II} represent the extra and intra cellular concentration of carbon dioxide respectively. Cai and Reimers [31] showed that an effectively constant reference potential can be guaranteed by using moderately high concentration of bicarbonate (*i.e.* 10^{-3} to 10^{-2} HCO_3^-) in the internal electrolyte reservoir.

The carbon dioxide gas diffuses through a hydrophobic gas permeable membrane (*i.e.* typically ~20 μm thick) into a thin electrolyte layer (*e.g.* water or $NaHCO_3$) trapped between the membrane and the tip of a flat surface or a bulb pH electrode, until the equilibrium is established on both sides of the membrane, as schematically displayed in Figure 1 adapted from reference [19]. An Ag/AgCl reference electrode in contact with sodium hydrogen carbonate solution completes the electrical circuit to the pH working electrode. The potential difference between the two electrodes is measured by a standard high impedance voltage amplifier and display system. The most employed material for the gas permeable membrane is silicone rubber. This membrane material allows easy diffusion of carbon dioxide into the internal solution, where part of it dissolves and form CO_2(aq) [26,28,30].

The set of chemical reactions involving carbon dioxide hydration within the thin electrolyte layer are presented below, along with their respective constant of reaction.

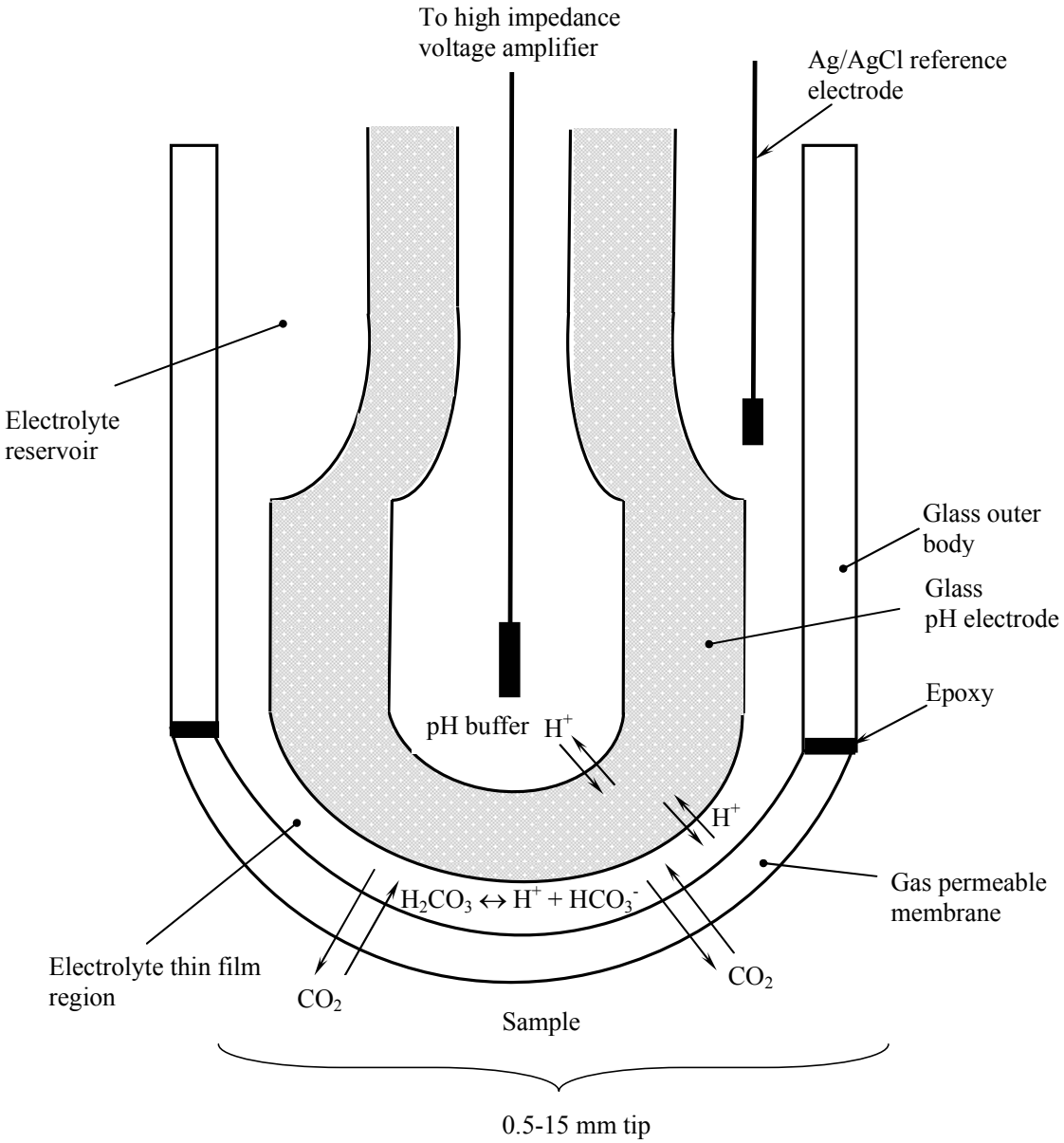

Figure 1. First generation Severinghaus type carbon dioxide sensor.

$$CO_2(aq) = p_{CO2} \times K_H \tag{2}$$

where $K_H = 30 \times 10^{-3}$ M/atm is Henry's constant [26]. The dissolved CO_2 reacts with either water or hydroxide ions, according to the reactions (3) and (4) below and forms carbonic acid and carbonium ion respectively [26,28,30].

$$CO_2\,(aq) + H_2O \leftrightarrow H_2CO_3\,(aq) \tag{3}$$

with $K_S = \frac{H_2CO_3(aq)}{CO_2(aq)} = 2.6 \times 10^{-3}$ M/atm

$$CO_2\,(aq) + OH^- \leftrightarrow HCO_3^- \tag{4}$$

Both the carbonic acid and carbonium ion dissociate pH dependently (according to reactions (5) and (6) below) [26,28,30].

$$H_2CO_3 \leftrightarrow HCO_3^- + H^+ \tag{5}$$

where $K_1 = \frac{[H^+]\times[HCO_3^-]}{[H_2CO_3]} = 1.72 \times 10^{-4}$ M/atm is the first dissociation constant for carbonic acid.

$$HCO_3^- \leftrightarrow CO_3^{2-} + H^+ \tag{6}$$

where $K_2 = \frac{[H^+]\times[CO_3^{2-}]}{[HCO_3^-]} = 5.59 \times 10^{-11}$ M/atm is the second dissociation constant for carbonic acid.

To account for the fact that CO_2(aq) is in equilibrium with H_2CO_3(aq), the first equilibrium is normally given by:

$$K_1 = \frac{[H^+]\times[HCO_3^-]}{[CO_2(aq)]} = 4.47 \times 10^{-7}\ \text{M/atm} \tag{7}$$

If we write the dissociation constants K_1 and K_2 in terms of chemical activity of each species present, and assuming that Henry's solubility law holds in the thin film layer, it can be shown [19,20,31] that the carbon dioxide partial pressure p_{CO2} in the thin electrolyte film is given by

$$p_{CO2} = \frac{a_{H^+}{}^2 + a_{Na^+}a_{H^+} - K_W}{\alpha K_1\left(1 + 2\frac{K_2}{a_{H^+}}\right)} \tag{8}$$

where $K_W = a_{H^+}\, a_{OH^-} = 10^{-14}\ M^2$ is the ionic product of water and α is the solubility coefficient of carbon dioxide in the thin electrolyte layer. The above reaction (8) is valid when a thin layer of water fills the narrow space between the tip of the pH electrode and the membrane. However, the design employing a distilled water electrolyte produced an unstable sensor [18], presumably because of the pH shift induced by even a slight contamination of the distilled water electrolyte. Severinghaus *et al.* [19] have introduced 5-20 mM concentration of sodium hydrogen carbonate as an electrolyte in order to stabilize the pH and increase the sensitivity. Under this circumstance, apart from the above reactions (*i.e*. reactions (1) to (6)), sodium hydrogen carbonate dissociation occurs:

$$NaHCO_3 \leftrightarrow Na^+ + HCO_3^- \tag{9}$$

Therefore, equation (9) above simplifies to

$$p_{CO2} = \frac{a_{Na^+}\, a_{H^+}}{\alpha K_1} \tag{10}$$

Severinghaus also demonstrated that when the p_{CO2} in the hydrogen carbonate layer changed to a new value, then by observing that both a_{Na}^+ and K_1 are constants and cancel out when two a_{H}^+ values are inserted and by taking logarithm of both sides of equation (10), the relationship between the changes in p_{CO2} and the pH in bicarbonate solutions is given by:

$$\Delta \log p_{CO2} = -\Delta pH \tag{11}$$

with Δ standing for a change in logarithm of p_{CO2} and a change in pH.

In the bicarbonate layer, by definition:

$$\Delta pH = -\Delta \log a_{H}^+ \tag{12}$$

The sensitivity of the sensor (S) is defined by Severinghaus as:

$$S = \Delta \log p_{CO2} / \Delta pH \quad (13)$$

Thus, if S = -1 then each order of magnitude change in p_{CO2} will theoretically generate a one unit change in the pH of the bicarbonate solution which would be registered as a change in voltage of 61.5 mV at 37°C (*i.e.* human body temperature), as predicted by Nernst equation.

A problem associated with a detection set-up based on the above hydration reactions of carbon dioxide (*i.e.* reactions (3) and (5)) is that the attainment of equilibrium is very slow. In order to address this inconvenience, the carbonic anhydrase enzyme has been added to the electrolyte solution to speed-up the reaction [26,32-34]. Following the same principle as the so-called zinc-hydroxide mechanism of CO_2 catalysis in human blood, the carbonic anhydrase catalysis in aqueous media results in the formation of HCO_3^- and H^+ ions starting from water and carbon dioxide. In addition, being a very powerful catalyst, with a turnover of 10^6 reactions per second [26,28,32,33,35] carbonic anhydrase facilitates a short response time of the sensor.

The typical dimensions of the first generation Severinghaus-type potentiometric carbon dioxide sensors were 3-3.5 mm in length and 1-1.5 mm outside body diameter [19]. The first miniaturized version of the Severinghaus-type microelectrode appeared 16 years later [21]. A schematic of a potentiometric type CO_2 sensor of the most recent generation having an internal pH electrode with a liquid ion exchanger membrane (LIX) is presented below in Figure 2 [25,26,28,34,36]. The inner pH sensor with an ion exchange membrane tip is positioned within the shaft of the electrode, behind the gas-permeable membrane.

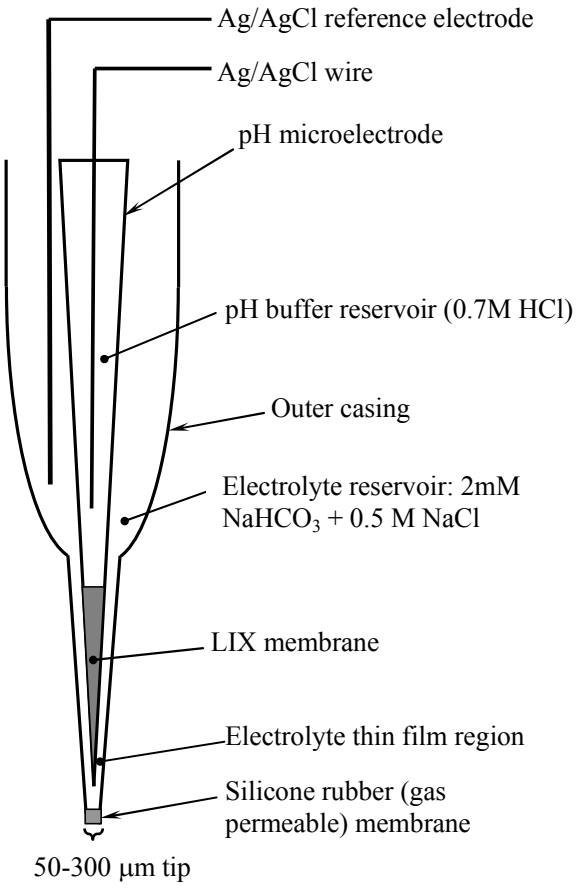

Figure 2. Miniaturized version of the Severinghaus-type CO_2 sensor employing liquid ion exchange membrane.

This arrangement requires an even smaller internal pH microelectrode tip, and the subsequent placement of the latter inside the shaft of the outer casing. Beyenal *et al.* [28] reported that merely 1 out of 10 microsensors built in their laboratory displays reliable calibration curves and is useful in further utilization. Other authors [31,34,36] used a somewhat larger sensor design, having an external tip diameter in the range of 50 to 300 μm, but these dimensions were not a result of the difficulty in achieving miniaturization. Zhao *et al.* [34] in fact showed that for a certain glass material, the ratio of the surface area of glass to the volume of solution (S/V), is inversely proportional to its tip diameter.

This ratio determines the extent to which the performance of a p_{CO2} microelectrode is influenced by chemicals leaked from the glass wall. Thus, the smaller the tip diameter, the larger the S/V and the greater the effect exerted by the glass material over the sensor performance. With this respect, Zhao *et al.* [34] showed that if the tip of the outer casing is less than 150 μm, then the performance of the microelectrodes depends on what type of glass materials is used to construct the inner pH microelectrode. In their study, Zhao *et al.* [34] reported that alumina silicate glass showed better results than Pyrex glass whereas the lead glass displayed the poorest results. The above mentioned group correlated these results to the greater weight loss of the lead glass (*i.e.* 3.6 mg/cm^2 measured after 6 hours exposure at 100°C to a 5% NaOH solution, compared to 1.4 mg/cm^2 for Pyrex and 0.35 mg/cm^2 for alumina silicate glass). When the tip of the outer electrode was further decreased to a value below 50 μm, the performance of the sensor decreased irrespective of the glass material used in fabrication of both the outer and inner pipette [34], the authors suggesting that other type of glass with high chemical stability being necessary to employ for further improvement of the system performance. Zhao *et al.* [34] conclusions are supported by Cai and Reimers [31]. In the latter study, a sensor stability of two weeks was reported for a sensor with 300 μm tip and the outer shaft made of lime glass (*i.e.* 1.1 mg/cm^2 weight loss). However, a large tip diameter is not necessarily good in all the aspects of detection, since it greatly improves the stability but reduces the response of the sensor up to 14 mV/decade of μatm p_{CO2} for the detection at low carbon dioxide partial pressure [34]. In an exactly opposite way, a small tip diameter improves the detection at low CO_2 partial pressure, but has a reduced lifetime to only several hours for a 4-10 μm tip [34]. Similar results were reported by other authors [20,25,28] which suggested that

the external tip of the sensor needs to be smaller than 20 μm, (*e.g.* a value of 2 μm being in fact reported by Hanstein *et al.* [26]) in order to improve the detection characteristics (sensitivity, selectivity, response time) at low CO_2 concentrations.

Initially was considered that the thickness of the gas selective membrane represented the rate limiting factor in achieving a good response time. Instead, studies performed by Cai *et al.* [31] and Beyenal *et al.* [28] show that the dissociation of H_2CO_3 is actually the rate limiting factor. Zhao *et al.* [34] shed more light into this problem, showing that in the presence of carbonic anhydrase, the hydration of the CO_2 gas represents the rate-limiting-step if the membrane thickness ranges between 15 and 35 μm. The carbon dioxide hydration equilibrium is displayed in the equation (14) below which represents the actual equilibrium between CO_2 and water, in fact the summation of equations (3) and (5) above in the case of reasonable assumption that the equilibrium concentration of H_2CO_3 and CO_3^{2-} is negligible [37]):

$$CO_2 + H_2O \leftrightarrow HCO_3^- + H^+ \quad (14)$$

All the measurements performed with membranes having dimensions within this interval resulted in obtaining identical response times for the sensor. Above 35 μm, the response of the sensor was governed by both diffusion and rate of hydration reaction, and it became completely dependent on the diffusion process through the membrane if the thickness exceeded 365 μm. The group did not employ membranes with thicknesses smaller than 15 μm, without mentioning the reason behind their choice.

The Severinghaus type potentiometric carbon dioxide sensors are relatively unstable, displaying a reproducibility and stability of only several days. Drifts ranging from mV/h [34] to 10 mV/h [21,25,28] were reported. In contrast with these initial

values, the improved Severinghaus type microelectrode for CO_2 detection display a lower drift, which is acceptable for practical applications. Published drift values in the literature are: 0.5 mV/h by Komada *et al.* [36], 0.2 mV/h by Cai and Reimers [31], 0.4 mV/h by Zhao *et al.* [34]. The slopes of the calibration curves reported for the latest generation miniaturized potentiometric type carbon dioxide sensors were reported in the range of 56 to 80 mV/decade of μatm p_{CO2} [25-31,33,34], in fact double in value than the reported slopes for the first miniaturized Severinghaus-type potentiometric CO_2 sensor (35 to 45 mV/decade of μatm p_{CO2} for the latter [21-24]). Several authors [28,30,33,34] have showed that lower values of the calibration curve slopes belong to aged electrodes and higher values to the fresh ones.

The lowest CO_2 partial pressure detected with improved miniaturized Severinghaus-type CO_2 sensors was respectively reported as 6.37×10^{-4} atm by Beyenal *et al.* [28], 5.78×10^{-4} atm by Cai and Reimers [31], 4×10^{-5} atm by Hanstein *et al.* [26], 2×10^{-5} atm by Cammaroto *et al.* [33], 2×10^{-4} atm by Zhao and Cai [34], compared to 2.63×10^{-2} atm as reported by Caflisch and Carter [21] for the first generation of miniaturized Severinghaus type CO_2 microelectrode.

However, another problem that arises because of miniaturization is that the small volume of carbonic anhydrase solution (less than 10 μl) renders the solution susceptible to changes in compositions due to exposure to the pH microelectrode and Ag/AgCl wire. The composition of the solution inside the pH microelectrode (the H^+ selective buffer) is extremely important since a more acidic buffer than the electrolyte buffer solution will lead to the leak of the protons from the inner pH microelectrode solution into the electrolyte solution containing anhydrase. This proton leak may change just slightly the

concentration of the anhydrase solution, but enough to create a drift since the enzyme displayed an increase in activity with increasing pH up to pH = 10 [35]. In order to address this issue, Hanstein *et al.* [26] introduced an excess quantity of sodium hydrogen carbonate ($NaHCO_3$) in order to fix the pH to a value around 8.3, in conformity to Henderson-Hasselbalch equation (15) below, in fact a rearrangement of equation (5) above. The pH value of 8.3, being different from both pK_1 and pK_2, warranted a sufficient sensitivity to carbon dioxide:

$$pH = pK_1 + \log [HCO_3^-] / [H_2CO_3] \quad (15)$$

Since the first report of a potentiometric type CO_2 sensor [19], the research focused mainly on the improvement of the working electrode functions [26-28,30,31,34,36,38-40]. So far, the most employed pH microelectrodes consisted of glass (*i.e*. alumina glass [34], lead glass [34], Pyrex glass [34], lime glass [31], borosilicate glass [26]) or Sb-SbO_x materials. Despite their good sensitivity, selectivity and stability, the shortcomings displayed by glass electrodes rest in their difficulty to miniaturize and sometimes unsuitability for measurement inside the solid food products due mainly to their fragile configuration. On the other hand the Sb-SbO_x working electrodes suffer from oxygen interference and a subsequent drift. Due to these disadvantages, the development of new reliable materials to substitute for the glass (*i.e.* alumina silicate, Pyrex, lima, lead) or Sb-SbO_x became an urgent necessity.

Iridium oxide was proposed as a potential substitute. The sensors developed using this novel material showed a very good dynamic range and a negligible drift [27,28,30, 39,40]. As an advantage, the sensors having the tips made of iridium oxide showed no need for the liquid ion exchanger membrane, the iridium oxide being actually grown on

the tip of the iridium inner sensor as schematically showed in Figure 3 adapted from reference [28]. In this configuration, they displayed improved stability and response time [28,30,34,39]. A drift of 0.03 mV/h, in fact 10 times smaller than the lowest reported drift among the sensors employing liquid ion selective membrane on their tip was reported [28,39].

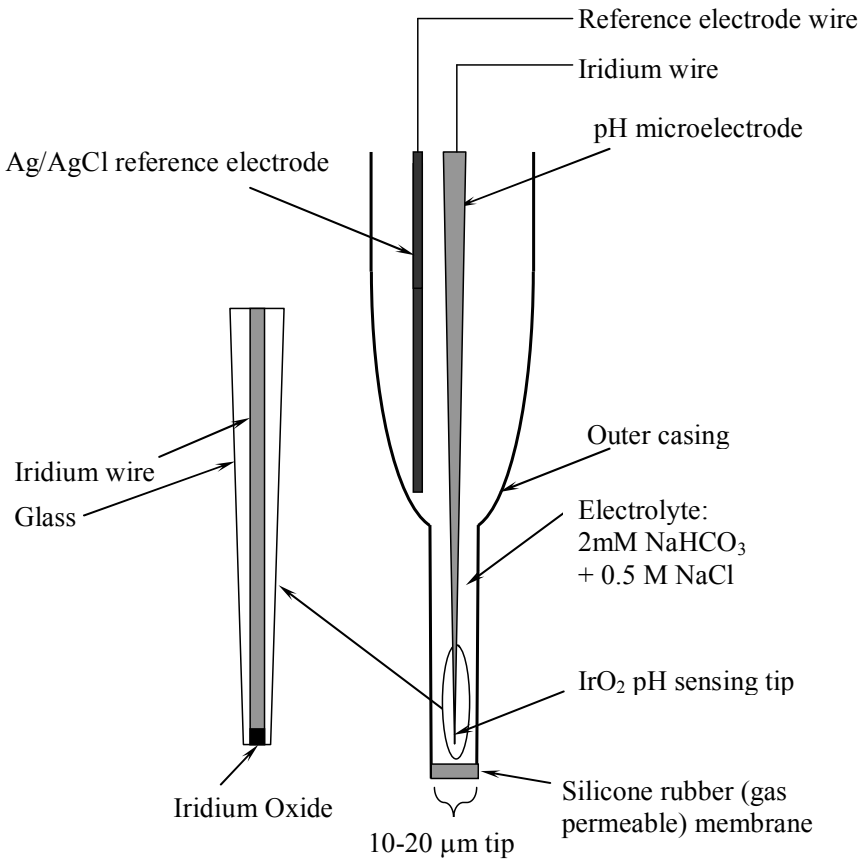

Figure 3. Iridium oxide tip miniaturized Severinghaus type CO_2 sensor.

The range of response times have been reported in seconds or minutes. Generally the response time was placed in the range of minutes [28,31,33] but reports placing it in the range of seconds also appeared [25,26]. Thus de Beer *et al.* [25] reported "between 10

seconds and few minutes", while Hanstein *et al.* [26] reported an interval between 18 and 63 seconds, with a mean of 43 seconds. However, the response time falls in the range of 1 to 3 minutes in most of the reports. The difference in the response time can be associated with many different factors: the composition of the internal electrolyte, the nature of the gas selective membrane, and the dimension of the tip of the sensor. In addition, the way to calculate the response time is an important issue that is not yet standardized. Generally, it is calculated as the time elapsed from the beginning of the measurement to the point when the signal reached 90% of the amplitude, but the interpretation of this interval remains at the authors' discretion. Moreover, the reported values represent sometimes an average of the measurements taken with different devices.

The potentiometric methods of detection require a very strict control over experimental variables (*i.e.* temperature and ionic strength) if one is concerned with accurate measurements. Due to the logarithmic scale of the Nernst equation (1), for the detection of a univalent ion, a one mV error generated during the reading of the electrode potential will result in a 4% error in concentration reported. In the case of a divalent ion, this error will be double. The potentiometric sensors, being actually pH dependent, display interference not only from ions but also from organic and inorganic acidic or basic volatile compounds (*e.g.* H_2S, NO_2, SO_2, benzoic, cinnamic), leading to an undesired potential change. In addition, the presence of microorganisms that could produce a pH shift represented another problem to consider in designing the potentiometric type sensors for carbon dioxide. Last but not least important is the inability of Severinghaus-type potentiometric sensors to perform extended time monitoring of carbon dioxide concentration. This fact is due to the bulk of electrolyte

which would theoretically play no part in the equilibration process and is envisioned to serve just as a reservoir and electrical conductor. All active processes take place only in the thin electrolyte layer at the tip of the pH microelectrode, and is therefore important to keep the sensor immersed in a stable reference gas or liquid solution between readings to allow in this way the sensor to work always from a stable pH reference point in the sodium bicarbonate layer and to return to the same point after the CO_2 measurement. If the sensor is maintained too long in a sample solution, the p_{CO2} in the bulk of the sodium bicarbonate electrolyte reservoir will begin to come into equilibrium with the p_{CO2} of the sample and this event will destroy the stability of the sensor.

1.3.1.2. Amperometric Type CO_2 Sensors

Another method used in the detection of carbon dioxide is the amperometric mode [33,41-71]. In the amperometric mode, the gas of interest is allowed to pass through a gas-permeable membrane and diffuse in the inner electrolyte solution until equilibrium is established on the both sides of the membrane. The formation of a metal salt (*e.g.* chloride, sulfate, phosphate, depending on the type of electrolyte employed) occurs due to the pH change induced by the carbon dioxide dissolution in the electrolyte. The metal salt can be reduced to the electrode through a quasi-reversible path, the current raised during the reduction process being proportional to CO_2 concentration in the electrolyte solution and therefore easily correlated to the CO_2 partial pressure in the analyte medium.

Evans *et al.* [46,47] showed that although the response of their sensor resulted from a pH change of the electrolyte, the chemistry involved, the nature of the response,

and the design of the sensor differ from the Severinghaus type carbon dioxide electrode. It was initially thought that since the current density is dependent upon the rate of reduction of Cu^{2+} ions at cathode, then the increase in the number of ions through increasing the concentration of copper diamine complex would increase the sensitivity of the device [46,47]. What was discovered in reality was actually much more complicated. A low concentration of the copper diamine complex (*i.e.* 2-3 mM) rendered a higher sensitivity towards carbon dioxide (up to maximum 10% CO_2), whereas a too high concentration (*i.e*. 50 mM) resulted in a limited current density due to the formation of a precipitate in the solution (identified as copper hydroxide). In the same time, a too low complex concentration (*i.e*. 0.5 mM) gave a non-linear current density vs. % CO_2 curve, with a short linear portion suitable for the detection of CO_2 concentrations less than 1%. However, the sensor showed poor stability mainly due to the strict requirement placed over the selection of copper diamine complex concentration. In designing a system to work on the same principle as presented by Evans *et al.* [46,47], Fasching *et al.* [50] chose non-volatile buffer substances N,N-bis(2-hydroxyethyl)-2-aminoethansulfoneacide, N-tris (hydroxymethyl) methyl-2-aminoethansulfoneacide, and N,N-bis (2-hydroxyethyl)glycine and showed that these ones form more stable ligand compounds with copper ions. The choice of the ligand is in fact more complex than just its volatile behavior. This is because the reaction of copper with hydroxyl ions results in the formation of copper hydroxide, according to the equation (16) below:

$$Cu^{2+} + 2OH^{-} \rightarrow Cu\,(OH)_2 \qquad (16)$$

The poor solubility of the copper hydroxide (1.6×10^{-19} mol/l) corroborated with the ease of crystallization can lead to a depletion of the free copper in the electrolyte and

degradation of the sensor reproducibility and stability. The formation of copper hydroxide is favored by high free ion concentrations at pHs greater than 7, therefore in order to keep the Cu^{2+} concentration in solution low, Fasching *et al.* [50] proposed the use of ligands with almost complete complex formation at higher pHs. Dissociation of copper complexes that takes place in the pH range between 7.7 and 6 resulted in the release of unbounded copper ions, corresponding to a p_{CO2} in the range of 10^{-3} atm up to one atm. A schematic of an amperometric sensor of the latest generation developed by Fasching *et al.* [50] is presented below in Figure 4 adapted from reference [50].

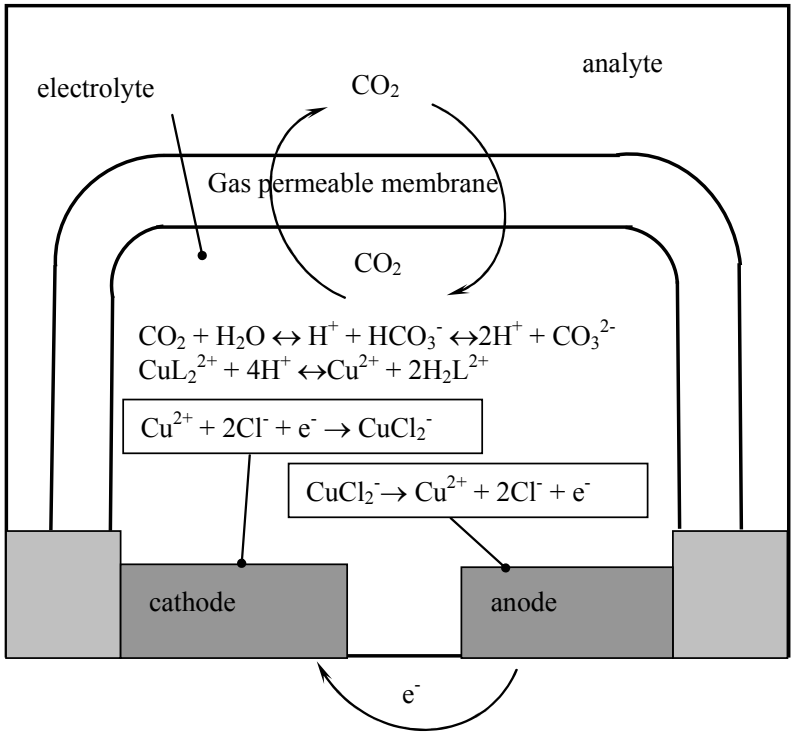

Figure 4. Sensing concept of the amperometric CO_2 sensor.

1.3.1.2.1. Reducing Specie; Electrode Material

The first report about the reduction of carbon dioxide at platinum electrode dates more than 40 years [55,56]. Carbon dioxide represented in fact the species that was in

most of the cases directly reduced [41,43,45,49,52-57,62]. Unfortunately, CO_2 is not electroactive over a larger potential range, and CO_2 reduction wave overlaps with H^+ reduction in aqueous solutions [41,46-48]. Due to this inconvenience, aprotic solvents (*e.g.* DMSO, N,N-dimethylformamide, acetonitrile) were investigated [41,43,45,51-53,57]. Wadhawan *et al.* [70] showed that compared to water, DMSO offers the advantage of a significantly greater solubility of CO_2, corroborated with the ability to withstand wider cathodic potential until the solvent breakdown occurs. Detailed information about the cathode material and reduction element as well as the respective reference is presented in the Table 1.

Table 1. Reduction elements and cathode materials employed in amperometric CO_2 sensors design.

Reduction Element	Cathode Materials	Reference
Carbon Dioxide	Mercury	53
Carbon Dioxide	Gold	52,53
Carbon Dioxide	Gold microdisc (ϕ = 10 μm)	52
Carbon Dioxide	Amalgamated gold	52
Carbon Dioxide	Amalgamated platinum electrode	52,55,56
Carbon Dioxide	Platinum	57
Carbon Dioxide	Thin film platinum	45
Carbon Dioxide	Platinum microdisc sealed in glass	43
Cu^{2+}	Miniaturized platinum cathode	50
Cu^{2+}	PTFE-sprayed-platinum porous electrode	46,47
Hydrogen	Platinum Oxide	41
Carbon Dioxide	Rhodium	62
Carbon Dioxide	Miniaturized rhodium (thickness = 60 nm)	49
Carbon Dioxide	Silver	41
Hydrogen	Ruthenium Oxide	48

1.3.1.2.2. Gas Permeable Membrane

The gas permeable membrane that allows easy diffusion of carbon dioxide from the analyte medium into the inner electrolyte solution is in most of the cases fabricated from silicone rubber, but Teflon, gold-coated Teflon and platinum oxide sputtered PTFE have also been employed [41,43,45,49]. As an alternative to these hydrophobic membranes, Cammaroto *et al.* [33] employed an immobilized enzyme (carbonic anhydrase) coupled with a redox mediator (p-benzoquinone) which used CO_2 as a

substrate, replacing in this way the electrolyte with a suspension of carbonic anhydrase in Tris-HCl buffer of pH = 8.3.

Qian *et al.* [43] found that oxygen presence in the solvent generated a prewave on the voltammogram of CO_2 reduction while causing a successively increasing of the peak-shaped current, which could rise up to ten times as much as the normal limiting current. This increase suggested complicated changes in the overall reaction. The source of oxygen could be either the oxygen gas dissolved in the liquid electrolyte or that contained in the gas sample to be detected. Therefore, since the oxygen interference could not be corrected by simple mathematics the purpose of the amperometric sensor designers was to avoid the presence of oxygen in the electrolyte by shielding the working electrode from O_2 interference. Simultaneous electrochemical detection of carbon dioxide and oxygen in nonaqueous solutions like DMSO or acetonitrile was challenged by the easier reduction displayed by the oxygen compared to carbon dioxide in those solvents [41,45,46]. Due to the easy reduction of oxygen in aprotic solvents, it is therefore impossible to detect the concentration of a small percentage of CO_2 in the presence of a much larger O_2 generated current. The oxygen interference is caused by the proximity of the reduction potentials of the two gases, and the overlapping of the reduction waves in aprotic solvents occurs at far less negative potentials as compared to aqueous electrolytes [42,45,46]. At those negative potentials necessary for CO_2 reduction, the reduction product of O_2 is a superoxide ion that interferes with CO_2 measurement and accumulates inside the solution [41,42]. In aqueous solvents however, no oxygen interference is expected if the potential of the cathode is controlled to an appropriate value (0.15 and 0.22 V vs. Ag/AgCl for potassium chloride and potassium bromide electrolyte solutions

respectively) [47]. Until now, three attempts were made to circumvent this superoxide interference effect by designing gas-phase O_2-CO_2 sensors using macro-cathodes.

In first of these attempts, Albery *et al.* [42] employed double membrane-double solvent layer sensor. The outer gold metallized membrane where O_2 was reduced in an aqueous electrolyte layer buffered at pH = 5 was polarized at -0.7 V. The current raised after O_2 reduction at gold metallized membrane was proportional to O_2 concentration, the O_2 filtering offered by the membrane being estimated at 99%. The carbon dioxide passed through the outer membrane, through the first layer of electrolyte and through another Teflon membrane, reaching an inner compartment composed of DMSO and silver macro-cathode as electrolyte/electrode system respectively. The CO_2 was reduced to $CO_2^{\cdot -}$ at silver electrode. The construction itself was however complicated and led to a slow response time of the sensor due to a double membrane barrier. In addition, Hahn [20] communicated in his review paper that no other group could reproduce Albery *et al.* [42] results.

In a second attempt, the electrochemical filter technique for O_2 was not followed any longer and a pulse titration technique employed [68-71] instead. Unfortunately, the set-up proposed by Albery *et al.* [68,69] was suitable only for gas phase detection and the gold macrocathode (*i.e.* 1.5 mm in diameter) using a pulse titration technique, was not suitable for miniaturization and involved a complex set of chemical reaction in the electrolyte layer [68,69]. The set of chemical reactions proposed by Roberts *et al.* [72] is in accordance with Albery *et al.* [68,69] as well as other groups finding [70,71]:

1) The reductive pulse that lasts typically 200 ms [20,69] performed at a potential where CO_2 reduction is inactive:

$$O_2 + e^- \rightarrow O^{2.-} \quad (17)$$

2) The titration step in which some of the O^{2-} reacts with any CO_2 present:

$$2\ O^{2-} + 2\ CO^{2-} \rightarrow C_2O_6^{2-} + O_2 \quad (18)$$

3) The recovery step (oxidation of the untitrated O^{2-} back to O_2), accomplished by switching the electrode to an oxidizing potential (typically lasts 350 ms);

$$O^{2-} \rightarrow O_2 + e^- \quad (19)$$

The difference between the generated and the recovered O_2 is a measure of the concentration of CO_2 in electrolyte. Unfortunately, the reduction pathway exemplified in the reactions (17)-(19) above has the shortcoming of regenerating O_2, which is further reduced during the first voltage pulse, leading to an increase of the observed overall O_2 reduction signal. This event makes necessary a complex set of mathematical model to deconvolute the true O_2 and CO_2 concentrations [69].

The third attempt to solve the superoxide interference problem was performed by Qian *et al.* [43]. The group employed a porous hydrophobic platinum catalyzed Teflon membrane electrode to remove oxygen in the first step and performed a measurement of CO_2 at a platinum microdisc in a following step, the system designed consisting therefore in a two separate amperometric sensors combined. Qian *et al.* [43] showed that the first membrane electrode completely consumes the oxygen, allowing only the carbon dioxide to reach the second amperometric sensor consisting of DMSO and platinum micro disk of 60 μm diameter. As with the other two methods attempted, this third one was also suited only for gaseous samples analysis. Due to the different transport times of the two gases, the overall system designed by Qian *et al.* [43] displayed a 90% change in O_2 and CO_2 in 15 and 35 seconds respectively and could not be employed in breath-by-breath analysis

that required a sensor with a response time less than 0.1 second. As an improvement to the setup proposed by Qian *et al*. [43], Hahn *et al.* [65-67] reported a sensor capable to measure simultaneously O_2 and CO_2 at unshielded gold microdisc cathodes in DMSO electrolyte, creating in this way a single amperometric sensor cell. The current generated after the carbon dioxide reduction was obtained by subtracting the O_2 background current from the total current. The authors showed that the reduction of each specific gas was independent of the amount of the other, and the reduction took place at different potentials making the system display minimal interference.

1.3.1.2.3. Electron Transfer Studies

The attention of electrochemists focused towards understanding the nature of the electron transfer process between reducing specie and cathode material. Sawyer's group [52,53] employed chronopotentiometry to extract information about the reaction occurring at electrode in amperometric carbon dioxide sensors. In chronopotentiometry, a constant current is passed through an electrolytic cell and the potential of the working electrode is monitored. The variation of this potential with time takes the form of a wave, and information about the reactions occurring at the electrode can be obtained from the shape and duration of this wave. This analysis led the group conclude that the gold electrode allowed just one electron reduction whereas the platinum electrode gave two electrons. In a later study, Eggins *et al.* [57] confirmed the nature of one electron reduction for gold cathode, suggested by Sawyer's group [52,53]. Haynes *et al.* [53] suggested that the reduction at mercury electrode is a diffusion controlled one electron overall reduction process, dependent also on the applied potential. Thus one electron per

mole of CO_2 is consumed at less negative potentials (-2.3 V vs. SCE) and two electrons per mole of CO_2 are consumed at more negative potentials (-2.5 V vs. SCE). The two-electron value is believed to result from catalytic solvent reduction by an intermediate species at the more negative applied potential. All these studies (*i.e.* [52,53,57]) were consistent in concluding that whether or not water was present in the aprotic system employed, the reduction of carbon dioxide involved the production of $CO_2^{\cdot -}$ in the first step, followed thereafter by a multitude of competing possibilities. These various pathways that followed the $CO_2^{\cdot -}$ generation depend strongly on the experimental factors like current density and diffusion layer concentration and thickness, leading to uncertainty in extrapolating the macro scale electrolysis results to the micro scale and vice-versa.

1.3.1.2.4. Reduction of O_2 and CO_2 at Micro-electrodes

The most important difficulties encountered in designing an amperometric sensor for carbon dioxide detection were represented by the instability of the electrolyte and the overlapping of the reduction potentials of oxygen and carbon dioxide. In addition, the electrode dimension represented a factor of influence. With this respect, Hahn [20] showed that the CO_2 reduction waves completely disappear in the presence of oxygen at large size electrodes. Moreover, Zhou *et al.* [45] reported that microelectrodes are preferable over the regular size electrodes. The microelectrodes display a much smaller ohmic drop over the electrolyte, making the measurements possible even using highly resistive non-aqueous media [20,40,58,70]. The microelectrodes also display a reduced capacitive component of the total current, which leads to an increase of the signal-to-

noise ratio in transient faradaic measurements. Finally, the steady states of mass transfer are rapidly established, which makes the microelectrodes convenient for performing steady state current measurements. On the other hand, the response profile of the CO_2 microsensors depends on the thickness of the diffusion-limiting electrolyte thin layer on the microelectrode surface. The use of microelectrodes was later shown to be necessary for the simultaneous detection of CO_2 and O_2 since it was believed that the kinetics of the intermediate reactions that preceded the formation of the peroxy dicarbonate anion was outrun by the much faster diffusional loss at the electrode-electrolyte interface [20,65-67]. By employing miniaturized electrodes the current signal that arises at cathode is independent of the presence of another gas. Regarding the material choice for the miniaturized electrodes, Hahn *et al.* [65-67] described gold as a better reductive element than the investigated platinum or glassy carbon disc for the same 10 μm diameter. On the other hand Zhou *et al.* [71] proposed a platinum cathode microdisc of 60 μm diameter.

1.3.1.2.5. Characteristic Values Reported

Zhou *et al.* [45] reported the lower detection limit as 0.4% CO_2 but other groups recorded even lower values: 0.1% by Fasching *et al.* [50], 0.04-0.1% and 0.025% by Ishiji *et al.* [41,48]. The response time of the carbon dioxide amperometric sensor is much lower compared to that of potentiometric counterparts. Response times ranging from 10-50 seconds [33,45,46] to 2 minutes [50] were reported, but also a very low value of only 5 seconds reported by Cammoroto *et al.* [33] in a configuration including carbonic anhydrase as a catalyst of the CO_2 hydration reaction. The sensor stability was reported in the range of hours [45], days [50] or even weeks [41].

1.3.1.2.6. Conclusions

Because the electrode reactions in amperometric mode are not fully reversible, but at most quasi reversible [46,47,50], the overall electrochemical CO_2 process consumes CO_2 from the sample. Consequently, any liquid or gas sample displaying the same CO_2 partial pressure will register different output when analyzed with the same amperometric sensor. There is therefore a so-called "liquid-gas difference" for the amperometric mode of detection of carbon dioxide and this is a major disadvantage of the amperometric mode over the rival potentiometric Severinghaus-type technique. However, this issue was somewhat resolved in the configuration employing micro-electrodes for carbon dioxide reduction, since they consume a negligible small quantity of analyte in which they are measuring and also produce a minimal quantity of bi-products.

1.3.1.3. Conductometric Type CO_2 Sensors

Conductometry represents another electrochemical technique employed for carbon dioxide sensing in which the conductance of the solution rather than the electric potential or current is measured [37, 73-80]. The conductance is a function of the pH of the solution and therefore dependent on CO_2 partial pressure.

The very first attempt to make use of the conductance of an electrolyte and to correlate this result with carbon dioxide concentration belonged to Cain *et al.* [73], who sought to extract information about the content of carbon in steel. The method employed by the group consisted of passage of the carbon dioxide gas resulted after the direct combustion of a sample of steel into a $Ba(OH)_2$ solution of known electrical resistance.

The absorption of carbon dioxide gas in the solution resulted in precipitation of barium according to the equation (20) and a subsequent increase in electrical resistance that could be correlated with the amount of gas dissolved and therefore to the initial content of carbon in the sample metal.

$$Ba(OH)_2 + CO_2 = BaCO_3 + H_2O \quad (20)$$

A similar approach was used by Holm-Jensen [74] to determine the CO_2 concentration in air by employing a solution of barium hydroxide and measure its change in conductivity as a result of a passage of a stream of air. Other authors [75,76] introduced the measurement of the conductance of the deionized water after the absorption of carbon dioxide in order to determine the amount of gas.

Lis *et al.* [77] reported a CO_2 sensor working on the principle of electrical conductivity by performing the measurement of the gas dissolved into a potassium hydroxide solution. Nevertheless, the sensor was rather big, with the dimensions in centimeters and required a very long preparation time prior to use (*i.e.* 2 weeks of treatment in distilled water) to clean the impurities on the glassy sensing head.

In one of the first attempts to measure carbon dioxide dissolved in liquid sample, Himpler *et al.* [37] employed a thin layer of water separated from the analyte sample by a dialysis membrane. The set-up represented actually a modified Severinghaus type sensor in which the conductance of solution was measured instead of a pH response as a result of carbon dioxide hydrolysis in aqueous electrolyte. By doing this, the problem of analyte depletion was eliminated, since the Severinghaus-type sensor does not necessitate the existence of an infinite sample reservoir of carbon dioxide. The one minute response time of the sensor depended on the kinetics of the hydrolysis of CO_2 in the thin water layer.

This response time is comparable to the response time of the first generation miniaturized Severinghaus-type potentiometric carbon dioxide sensor [21-24] and the sensitivity covered the analytical range of interest for blood analysis. However, Himpler *et al.* [37] detected a slow increase in conductance with time of exposure at the same carbon dioxide partial pressure. Proving that this small drift was not caused by the inadequate sample mixing or slow responding electronics, the group suggested that the problem might have been generated by the diffusion within the unstirred thin water layer inside the membrane. Another disadvantage of the development was that the time required for the sensor to detect a low to high CO_2 concentration transition was shorter than the reversed way.

Bruckenstein and Symanski [78] solved the drift problem by introducing a thick ion-exchanger layer bed separated from the thin water layer through a thin screen. The square of the conductance of the solution was then proportional to the carbon dioxide partial pressure in the water layer. The sensor responded to a range of concentrations of CO_2 from 0.45 to 5%. Unfortunately, the design showed unacceptable sensitivity to movement due probably to segregation or shifting of the particles composing the ion-exchanger bed. As a disadvantage, it was shown that the lighter anion-exchanger resin beads (responsible for HCO_3^- removal), which composed the ion-exchanger bed settled more slowly time than the heavier cation-exchanger beads. As a result, the conductance slowly increased in time due to a longer time required for carbon dioxide to diffuse down inside the ion-exchanger bed in order to be consumed [78].

One of the first reports regarding the use of polymers conductivity for CO_2 detection belongs by Saikai *et al.* [81] who employed a mixture of solid polyethylene

glycol and alkali carbonate. The sensor developed had a CO_2 dependent conductivity with a trade off in the lower detection limit, which could not be lowered below 0.5% CO_2.

A disadvantage of the conductometric method is the lack of selectivity of the system if more than one species is involved in the detection mechanism. Attempts to miniaturize the conductometric sensors showed that the stability is greatly affected by the dissolution of the thin electrolyte water layer with the easily volatile species presented as impurities on the sensor walls [37,79,80].

1.3.1.4. Coulometric Type CO_2 Sensors

Coulometric titration [23,24,82-92] to measure the pH of the solution represents another electrochemical technique employed for carbon dioxide detection. The design of ISFET follows the same principle as MOSFET (metal oxide field effect transistor), with only difference, that the metal gate of the MOSFET is replaced by a metal of a reference electrode, while the liquid in which this electrode is present creates the contact with the gate insulator. Both devices have characteristic the same electrical circuit, displayed in Figure 5.

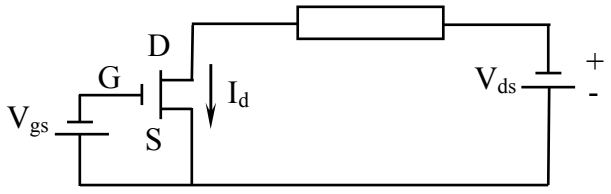

Figure 5. Schematic of the electrical diagram for ISFET.

A coulometric sensor is in fact an integrated sensor-actuator device that measures the pH changes induced to an electrolyte solution (*e.g.* water) by ions generation (*i.e.*

either H^+ or OH^- depending on the electrochemical reaction) at a generating actuator (*e.g.* a coulometric gold electrode) with the aid of a sensor (*i.e.* a pH sensing ion sensitive field effect transistor, ISFET). A schematic of a coulometric sensor is displayed in Figure 6 adapted from reference [84].

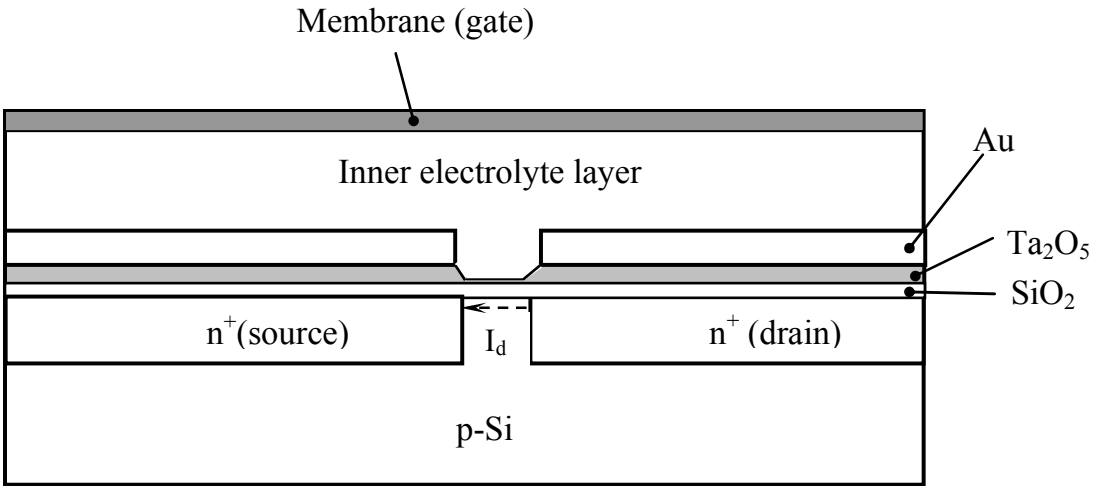

Figure 6. Schematic of the coulometric carbon dioxide sensor.

The coulometry allows one to develop a fixed relation between the coulombs applied to the actuator and the amount of generated ions, provided that the following conditions are fulfilled:

1) The stoichiometry of the electrode reaction is known;
2) No side reaction occur in the system;
3) The current efficiency of the electrode reactions approaches 100%.

The ions generated at the actuator can be considered as the titrant, with which a coulometric titration can be accomplished. In this way, the pH-sensitive ISFET is used as the indicator electrode for the detection of the end-point of the titration curve. The main advantage of the system is that it is suitable for performing acid-base titrations in nanoliter ranges in time of seconds. Another appealing feature of coulometry is that the

output of the sensor is provided by its own dimensions and not by the sensitivity of the working electrode, therefore a one time calibration is expected to be sufficient for an envisioned long time stability of the sensor.

A problem associated with the naturally occurring titration of carbon dioxide is the slow nature of it. Both reactions, the one involving carbonic acid formation and the following one involving carbon dioxide titration with hydroxyl ions are slow-a complete equilibrium occurring in about 5 minutes. However, a back titration if employed can speed up the reactions, mainly because the speed of the titration reaction of carbon dioxide with hydroxyl ions (*i.e.* reaction (4) above) is pH dependent. To do this, the excess of hydroxyl ions is introduced into electrolyte (*i.e.* carbonate) solution, raising the pH to about 10.5 to 11 pH units, values at which the reaction of CO_2 with OH^- is accomplished in few seconds, consuming all the carbon dioxide. The excess OH^- is now titrated in a regular way and the protons generated gave information about the amount of carbon dioxide originally present in solution.

In one of the first studies involving the latter method, Van der Schoot and Bergveld [84] presented an ISFET based potentiometric CO_2 sensor having a relatively good stability over a period of seven weeks. The drift reported (*i.e.* 0.05 mV/day) is much lower than the drift characteristic to usual potentiometric sensors.

The membrane thickness has a great influence over the response time of a coulometric sensor [84,91]. The presence of the membrane is necessary because the gate insulators materials normally used in ISFET preparation undergo surface ion exchange process especially due to H^+ presence that makes them prone to drift especially in the presence of alkali metal ions [91]. In order to solve this issue, membranes are chosen

from materials able to incorporate ionophores. By doing this, the interface of membrane to solution displays a potential selectivity for some ionic specie of interest, while preserving the permeability toward neutral specie (*i.e.* weak acids and bases, water vapors, CO_2, O_2, organic molecules).

Unfortunately, problems appear in this configuration due to the hydrophilicity of the membrane that accumulates a fragmented water layer on the surface, permitting some acid base reactions between neutral specie to take place at the interface and alter the potential. An alternative remedy to this problem has been proposed by Van den Vlekkert *et al.* [92] who introduced a thin water buffer layer between the gate insulator and the polymeric membrane. However, this set-up was not amenable to miniaturization because of the restricted buffer capacity of the layer and the subsequent leak due to high osmotic pressure. A viable solution nevertheless is the introduction of a thin Ag/AgCl or AgCl layer to the membrane surface to eliminate the neutral specie pH mediated sensitivity [93,94].

Coulometric sensors, as well as the other type of liquid based carbon dioxide sensors briefly described above (*i.e.* potentiometric, amperometric, conductometric), despite the very good achievements with respect to the response time and sensitivity, lack long term reliability mainly due to the existence of a liquid solution. The incorporation of a liquid, not only complicates the cell design and severely restricts the miniaturization but also affects the durability and integration of the sensor with microelectronic interrogation devices.

1.3.2. Spectroscopic Techniques

Most of the sensor designs based on spectroscopic techniques employ optical fibers [95-115]. This development is possible since carbon dioxide displays a strong infrared absorption band extending from 4.2 to 4.4 μm. Optical CO_2 sensors are divided into two categories. One is based on the optical detection of a color change in a pH indicator dye, mostly employed being thymolsulfonphthalein (thymol blue) and phenolsulfonphthalein (phenol red) [96,102-105,107,109,111]. The other configuration works on the principle of the CO_2 induced fluorescence change of a luminescent dye such as 1-hydroxypyrene trisulfonate [95-97,102,114].

The spectroscopic techniques involving dye-solvent solutions and optical fibers are advantageous if one is concerned with simultaneous determination of oxygen and carbon dioxide. The absorption bands in the visible region of the two elements do not overlap, providing no cross-interference between the two gases [101]. In addition to this, the major advantage of the optical fiber based detection rests in the ability to detect virtually the full range of carbon dioxide partial pressures, from almost zero to one atm.

Optical fibers mode of detection was employed also in conjunction with microdialysis technique [102], the system developed being able to concomitantly monitor hydrogen, oxygen and carbon dioxide partial pressures in blood and buffer solutions [102]. The system employed closed loops of micro-flow streams of reagents in microliter per minute, a simple optical system and a method of achieving steady microliter per minute flow rates, proved to have an excellent resolution in the range of interest for oxygen and carbon dioxide for medical applications. The above approach offered also a

response time of only 4.8 min, 1.8 min, and 2.1 min for p_H, p_{CO2}, and p_{O2} measurement respectively [102].

A response time of only 40 seconds and a dynamic range covering all carbon dioxide concentrations (from virtually 0% to 100%) was reported for a configuration consisting of a carbonic anhydrase introduced into the immobilized phosphate buffer layer placed at the distal end of an optical fiber [96]. In this configuration the measuring principle rests on a CO_2-modulated proton transfer from the inner buffer to the photo excited tris[2-(2-pyrazinyl) thiazole] ruthenium(II) cation, immobilized onto an anionic dextran gel.

A solid state carbon dioxide sensor based on colorimetric detection principle comprises a dye immobilized in a water-immiscible polymer film or plastic material (polymer + plasticizer) [96,103-113,115]. The role of plasticizer is to ensure the diffusion of carbon dioxide in and out of the solid compound. The difficulty in achieving such a configuration is represented by the incorporation of water into the solid material employed (*i.e.* plastic or polymer film), to serve as a medium where the carbon dioxide hydration reactions take place. The nonpolar, hydrophobic nature of both the polymer and plastic medium impedes the incorporation of water. In addition, the solid medium should be designed in such a way to display little or no leaching of any of the sensing components. The above inconveniences can be circumvented to some degree by using a phase-transfer agent. Mills *et al.* [107] employing a sensor with a phase transfer agent, obtained a very low response time (less than 3 seconds) but at the same time they noticed that prolonged use of the sensing films lead to a deterioration of the sensing element.

Rocchia *et al.* [112] used a different approach for their carbon dioxide sensor working in diffuse-reflectance FTIR mode. Instead of using a plasticizer and a reference dye, the group introduced an amine-modified silica gel that interacted with carbon dioxide and created carbamates species, which were successively detected by infrared spectroscopy. However the setup was not developed as a portable device and in addition the repeatability of the sensing mechanisms was questionable, since the silica gel needed reheating at temperatures greater than 40ºC to liberate the bound carbon dioxide.

A very low response time of only one second was reported for a configuration employing the color change mechanism of a covalently immobilized dye in silicone rubbers [104]. This type of sensor is capable of measuring carbon dioxide both in gases (to which they respond with a t_{90} of 0.1 to 1 s) and in aqueous sample solutions (with t_{90} ranging from 2 to 8 min). The authors attribute the longer response time in water sample to the presence of water-filled micro droplets in the membrane, which constitute a reservoir for the gas-equilibrated sample. However, the sensor design needed careful storage and a preparation procedure (*i.e.* water equilibration) before use in aqueous sample.

Unfortunately, the spectroscopic techniques are not well suited for the determination of CO_2 partial pressure in liquids due to interference from other absorbing species, such as water vapor and carbon monoxide [101,104]. In addition, the achievement of equilibrium of carbon dioxide hydration and dehydration reactions is slow, leading to the necessity of inserting the carbonic anhydrase enzyme as a reaction catalyst. However, as already mentioned in the electrochemical techniques section, carbonic anhydrase solution becomes unstable due to the presence of microorganisms,

leading to a slow and undesirable pH shift. For the systems employing dye and solvent, some authors [101,104] observed the existence of a small signal drift caused by a small evaporation of the solvent and tried to circumvent it by simple replacement of the dye-solvent solution with a fresh one at regular time intervals. Moreover, for detection of carbon dioxide in liquid media, these types of sensors were reported to have a lower response time when measured virtually low to high CO_2 variation compared to the reversed way [96,110].

1.3.3. Other Methods of Detection

Quarts crystal microbalance (QCM) [116-123] and surface acoustic wave (SAW) devices [124-128] have been also employed for carbon dioxide detection.

The QCM method works on the principle of a quartz crystal oscillating frequency monitoring, subsequent to carbon dioxide interaction with the crystal coating. The technique takes advantage of the reactivity of carbon dioxide with amines, imines or zeolites at room temperature. However, the last two classes of compounds showed unsatisfactory results since zeolites displayed adherence problem with the crystal surface, whereas imines proved unsuitable due to degradation in time [116-123]. Among the amines, the N,N,N',N'-tetrakis(-2-hydroxyethyl) (THEED) showed good response [120-123]. However, this coating displayed low stability in time (*i.e.* the oscillating frequency changed in time, and consequently the sensitivity towards CO_2 fluctuated) and in addition presented interference from other volatile species (*i.e.* SO_2, NH_3). The tetramethylammonium fluoride tetrahydrate (TMAF) coating on the other hand displayed a better stability, but in the same time a lower sensitivity than THEED [120-123].

Surface acoustic wave sensors employ polymer coatings capable to absorb carbon dioxide and change the oscillating frequency Δf of the SAW device according to the equation (21)

$$\Delta f = (k_1 + k_2)\, f_0^2\, m/A \qquad (21)$$

where: f_0 is the operating frequency, k_1 and k_2 are material constants and m/A is the film mass per unit area.

The SAW devices were reported to work at room temperature [127-128], although an operating temperature in the range of 70 to 100 ºC offered higher sensitivity [124-126]. However, the room temperature detection is severely interfered by humidity and difficulty in finding an appropriate polymeric material to allow a high partition coefficient between the gas phase and the sensor surface. In fact Grate *et al.* [129] showed that the working principle is more complex than just a simple mass change of the coating. The above-mentioned group identified the swelling-induced modulus change effect as a major contribution to SAW vapor response. Therefore, the SAW sensor responses to gas vapors of interest are in reality multiplied beyond the effect of vapor mass alone. Grate *et al.* [129] compared the partition coefficients of the same vapor detected by SAW and by gas-liquid chromatography (GLC) and found always that partition coefficient in SAW case, K_{SAW} was greater than $K_{GLC,}$ sometimes by 4-6 times. Ruling out all the other possible influencing factors (*i.e.* volume, density, temperature change, *etc.*), the group concluded that the only factor that could explain such a difference is the dynamic modulus variation. Therefore, in selecting a material for a SAW device, the choice of material with high dynamic modulus is preferable in order to obtain the greatest potential for modulus effects.

Nevertheless, the main difficulty in devising polymeric materials for CO_2 detection is represented by the lack of discrimination displayed by these materials with respect to other interfering gases and water vapor. Thus, silicon based polymers such as poly (γ-amino propyl ethoxy / propyl ethoxy silane) (PAPP) and poly (γ-amino propyl ethoxy / octadecyl ethoxy silane) (PAPO) have been employed in order to reduce the interference from water vapor [117]. Other coatings containing silicon compounds (*e.g.* amino propyl trimethoxy silane (AMO) and propyl trimethoxy silane (PTMS)) have been used in different CO_2 types of sensors based on capacitance response [130]. In addition, mixtures of polymers have been employed to improve the sensor performance [128].

1.4. Conductive Polymers as Carbon Dioxide Sensors

1.4.1. Conductive Polymers: Description

Conducting polymers are polymers that can be modified in such a way that their electrical conductivity varies over several orders of magnitude. Alan MacDiarmid, Hideki Shirakawa and Alan Heeger discovered the conductive polymers almost 30 years ago and shown that they can be doped over the full range from insulator to the metal state [131].

The classical saturated polymers, in which all of the four valence electrons of carbon are used in covalent bonds, appear in the form of insulating materials and therefore are uninteresting from the point of view of electronic materials. Conjugated polymers however, have an electronic configuration that is fundamentally different. In the latter case, the chemical bonding leads to one unpaired electron (*i.e.* the π-electron) per atom bonding. This property becomes further interesting because the π-bonding in which the carbon orbitals are in sp^2p_z configuration and in which the orbitals of adjacent

carbon atoms along the chemical backbone overlap, leads to electron delocalization along the polymer chain. The conductivity achieved through the doping or charge injection is due to the introduction of charge carriers into the π-electron system that leads to the π-electron delocalization and the movement of electric charge along the polymer chains.

1.4.2. Insulator to Metal Transition Process

The first two conductive polymers discovered were sulfur nitride, $(-SN-)_n$ [132-134] and polyacetylene, $(-CH-)_n$ [131], but the latter one turn out to be the one extensively investigated. In polyacetylene, each carbon atom is linked through a σ-bond to each of the two neighboring carbon atoms and the single hydrogen atom in the repeated unit cell. Moreover, the hydrogen atoms overlap laterally through a π-bond, leading thus to a structure with one π-electron available for conduction for each carbon atom of the polymer backbone. This ideal structure of polyacetylene with equal length of the carbon-carbon bond would imply the existence of a metallic state. In reality, due to Peierls instability, the polyacetylene structure is dimerized [131,135-143], leading to a structure that has characteristic the existence of two carbon atoms per repeat unit $(-CH=CH-)_n$.

A consequence of this arrangement is the division of the initial π-band into two bands: π and π^*. Since only two electrons (spin up and spin down) are allowed to fill each band, the consequence is the attainment of fully occupancy of the π-band and an empty π^*-band. The energy gap between the highest occupied level in the π-band and the lowest unoccupied level in the π^*-band represents in this way the energy gap (E_g) that has to be

overcome in order to make the polymer conductive [131,135-142]. The existence of the energy gap between a lower fully occupied band and an upper empty band represent a characteristic feature of the insulators or semiconductors materials. This energy gap of potentially conductive polymers depends upon the molecular structure of the repeat unit and therefore gives the chemists the possibility to perform its control by design at the molecular level. In addition, the discovery of non-linear excitations in this class of conductive polymers, (*i.e.* solitons and confined soliton pairs (polarons and bi-polarons) allowed the interconnection between electronic and chemical structure [131,135-158].

There are in fact several methods through which conductive polymers can increase their conductivity:

1) Electrochemical doping;
2) Chemical doping;
3) Photo-excitation;
4) Charge injection at the metal-insulator-semiconductor interface.

However, the reversible doping in conductive polymers that allows a full control of conductivity at the entire range from insulators to the metal state can be achieved by chemical and electrochemical doping [131,135-142,146,159-172]. The conductivity achieved through photo-excitation and charge injection at the metal-semiconductor interface is just transient and lasts as long as the electrical or optical doping stimuli remain active. Wegner *et al.* [140] proposed a general equation of the doping process in conductive polymers:

$$P_n \leftrightarrow P_n^{\cdot+} A^- \leftrightarrow P_n^{2+} 2A^- \qquad (22)$$

for the oxidation reaction, the reverse reaction standing for the reduction process. P_n is defined as a periodic segment of a polymer chain that exchanges a full charge with either a redox partner (*i.e.* in the chemical doping) or with the electrode of an electrochemical cell (*i.e.* in the electrochemical doping) and is thereby transferred to its hypothetical first or second redox state [140,173,174]. This charge transfer process leads to the formation of a cation (anion for the reversed reaction) in the first redox reaction and dication (dianion) for the second electron transfer.

The ion radical is called "soliton" in the case of movement free and independent of each other of both the charge and spin along a single chain without being subjected to relaxation or trapping. This ion radical is instead denominated as "polaron" when it is linked to an elastic bond distortion and consequently cannot move without exchange of energy. The ion radical that appears because of the second redox reaction is called "bipolaron" and it is subjected to disproportionation according to reaction (23) below:

$$2\ P_n^{\cdot+} \leftrightarrow P_n^{0} + P_n^{2+} \tag{23}$$

depending on the temperature and the type of binding to the appropriate counterion.

During the doping process, the electrochemical potential (Fermi level) is moved either by a redox reaction or by an acid-base reaction into an energy region where there is a high density of electronic states. In the same time charge neutrality is maintained by the introduction of the counter-ions in the vicinity of the chain, rendering the conductive polymers salt-type characteristics [131,134-144,145,146,156-159,161-164,166,167,169, 171,173]. After the doping process, the electrical conductivity results from the existence of charge carriers (introduced through the doping process) and from the ability of those carriers to travel along the "highway" of overlapped π-orbitals.

In conclusion, the doped conjugated conducting polymers have good conductivity characteristics primary due to the following reasons:

1) The doping process results in an introduction of carriers into the electronic structure. Moreover, since every repeat unit represents a potential redox site, the conductive polymers can be doped either p-type (oxidized) or n-type (reduced) to a high charge carriers density [131,135-142,144-146,152,155,156,159,161-164,166,167,169, 171,173].

2) Charge carrier delocalization and its respective mobility along the polymer backbone are developed due to the attraction of an electron in one repeat unit to the nuclei of the neighboring units. This process of delocalization and the subsequent two-dimensional mobility of charge carriers along the polymer's chemical backbone are extended also in three dimensions through inter-chain electron transfer [131,135-142, 144-146,152,155-159,161-164,166,167,169,171,173].

This group of conductive polymers has been employed for the detection of CO_2 [81,175-181], and represent a solution for the detection of carbon dioxide at room temperature.

1.4.3. Polyaniline: Description

Among the conductive polymers, one of the most investigated is polyaniline [145, 157-159,161,162,164,167,182-184]. MacDiarmid *et al.* [160-162] proposed that the reduced form of a repeat unit in polyaniline contains two benzenoid rings, (*e.g.* 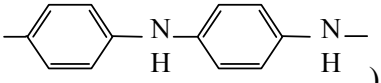), whereas the oxidized form of the repeat unit contains one

benzenoid ring and one quinoid ring (*e.g.* 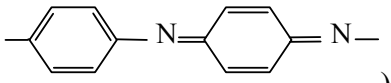), with none of these two in the form presented above carrying any electric charge. The transformation of a fully reduced into a fully oxidized repeat unit involves oxidation (*i.e.* loss of a hydrogen atom, in fact an electron and a proton), as schematically showed in Figure 7-adapted from reference [160].

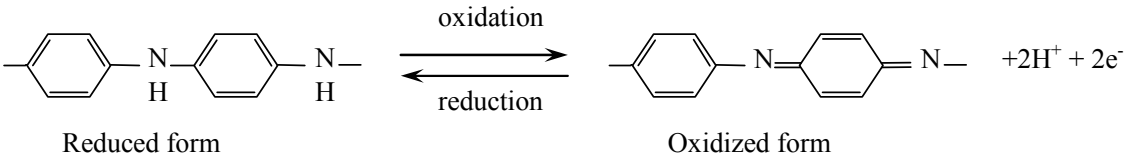

Figure 7. Oxidation of a fully reduced aniline repeat unit.

Chiang *et al.* [160] summarized the set of possible repeat units that could be found in polyaniline:

1) Unprotonated repeat units:

a) Completely reduced unprotonated polyaniline base repeat unit (1A)

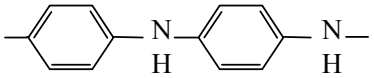

b) Completely oxidized unprotonated polyaniline base repeat unit (2A)

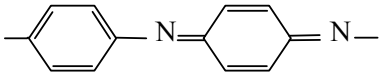

2) Protonated repeat units:

a) Completely reduced monoprotonated polyaniline salt repeat unit (1S')

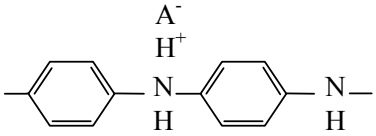

b) Completely reduced diprotonated polyaniline salt repeat unit (1S'')

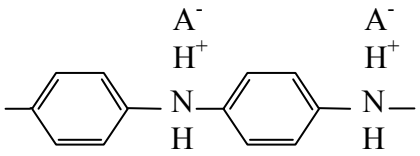

c) Completely oxidized monoprotonated polyaniline salt repeat unit (2S')

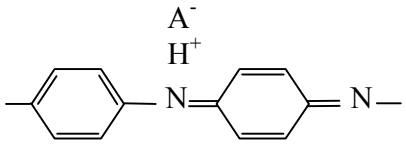

d) Completely oxidized diprotonated polyaniline salt repeat unit (2S'')

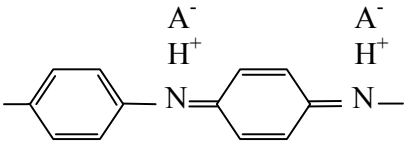

Polyaniline forms a wide range of oxidation states, from fully reduced form (leucoemeraldine) up to the fully oxidized form (pernigraniline). The leucoemeraldine chains of polyaniline consists of aromatic benzenoid rings, which are bonded to amine nitrogens, with each of the amines bonded to only one hydrogen atom. On the other hand, the pernigraniline form is composed of alternating benzenoid and quinoid rings, which are bonded only to imine nitrogens, with no hydrogen atoms bonding to the chain. The half-oxidized form of polyaniline is referred as emeraldine, and consists of an equal number of oxidized and reduced units (1:1 ratio of amine: imine nitrogens) and 3:1 ratio of benzenoid: quinoid rings.

A schematic of three-oxidation forms of polyaniline is presented in Figure 8.

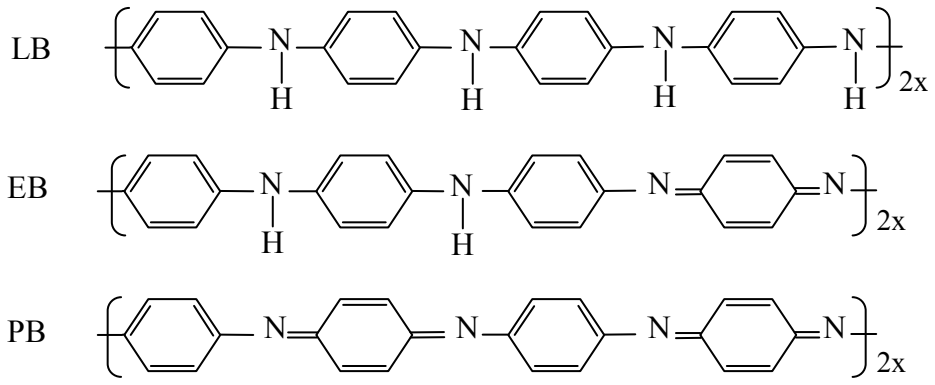

Figure 8. Polyaniline in various oxidation states.

In reality, polyaniline exists in more than three forms of oxidations. About 100 years ago, Green and Woodhead [185] were able to synthesize, isolate and analyze five distinct forms of polyaniline base, showing that the minimum number of $(C_6H_4)N$ groups necessary to permit an interconversion between those forms is eight. The above five specie were synthesized by Green and Woodhead [185] by means of chemical oxidation or reduction with agents having characteristic standard reduction potentials. Green and Woodhead [185] showed that in fact this polymer could exist in a continuum of oxidation states ranging all the way from fully reduced to a fully oxidized material

Depending on the pH of the protonating solution and the prior history of the sample (*i.e.* the degree of oxidation induced by the fabrication method), every polyaniline can undergo protonation to some extent. Huang *et al.* [162] showed that the extent of protonation decreases with increasing the extent of oxidation in the chemical backbone, thus pernigraniline shows little or essentially no protonation in acidic solution of pH greater than 1. Therefore, theoretically speaking, all the possible forms in which the polyaniline exists can be converted to their corresponding mono or diprotonated salt by treatment with an acid of appropriate strength [160-162]. However, studies performed on

the properties of the resulting salts showed that only emeraldine base could achieve a metallic-like conductivity when reaching its protonated salt form [160-162,167,172]. The chemical environment renders the emeraldine conductive through the protonation of imine nitrogen and/or deprotonation of amine nitrogen sites. Besides, protonation studies performed over the polyaniline base powders [157,158,160-169,171,186] showed that in spite of the fact that the amine nitrogen atoms present a greater base strength than the imine nitrogen counterparts, almost all of the imine nitrogen atoms protonate first. This preferential protonation of imine nitrogen atoms in emeraldine base is probably due to the better resonance stabilized structure that results in polymer chain.

MacDiarmid *et al.* [164,168,182] showed that an emeraldine sample prepared in air has 60% of the sites in oxidized form, whereas a sample prepared under inert atmosphere displays just 40% oxidized sites. It appears therefore that an increase in the number of oxidized sites would conduct to an increase in protonation and a higher conductivity. However, this is not the case, and as stated above, a sample oxidized in excess of 50% displays a lower conductivity than a sample 50% oxidized [164]. The same argument is valid for a sample substantially more reduced (*e.g.* prepared in air, with 40% oxidized sites). An explanation of this lower conductivity of emeraldine salts displaying a ratio of reduced to oxidized units different that one would rest in the generation of internal redox processes that occur in order to maximize the extent of conjugation in the delocalized polysemiquinone radical cations [182]. The latter radical cations would therefore localize and form metallic islands, whereas the excess oxidized and reduced groups would thus migrate and localize in the insulating beaches [182].

For a fully protonated, resonance-stabilized emeraldine salt chain, MacDiarmid *et al.* [160-162] have showed that all nitrogen atoms, all carbon-nitrogen bonds and all the C_6H_4 rings would be identical. Thus, all the nitrogen atoms in the ring would bear a + 0.5 electric charge, all the nitrogen atoms would be intermediate between an amine nitrogen and an imine nitrogen, all the C-N bonds would be intermediate between a single and a double bond and finally all the C_6H_4 rings would be intermediate between benzenoid and quinoid rings. Figure 9-adapted from reference [162]-depicts the resonance-stabilized form of emeraldine salt as proposed by Huang *et al.* [162]. In such a stabilized form, the highly conjugated π–electron system creates the premises for recording the metallic-like conductivities (up to 400 S/cm) for the emeraldine salt [183,184,187-189].

In addition, Paul *et al.* [186] and MacDiarmid *et al.* [160-162] showed that the maximum conductivity of the emeraldine salt polymer occurs when all the imine nitrogen units in the chain are in the (2S'') form above exemplified. On the other hand, if the protonated form of emeraldine salt occurs in the monoprotonated amine nitrogen site (1S''), then the conjugation will be severely interrupted, and the resonance stabilization of the backbone affected [160-162,166,186,190].

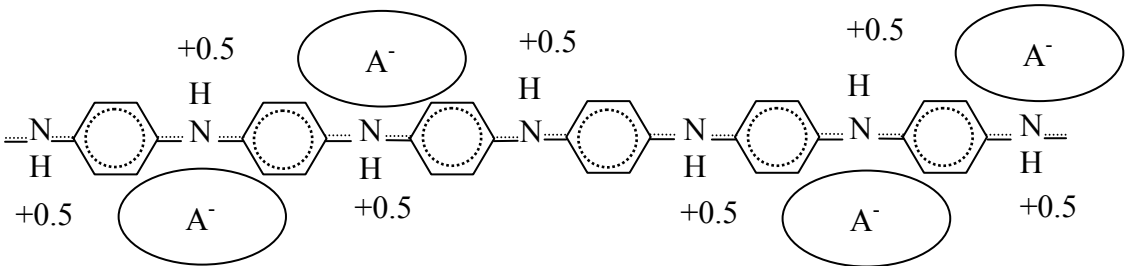

Figure 9. The resonance-stabilized form of the emeraldine salt polymer.

The sequence of structural changes in the emeraldine form of polyaniline after doping with a protonating acid is depicted in Figure 10-adapted from reference [137]- with all the steps briefly mentioned in the insert. During the doping process, the alternating polymer-like chemical structure of insulating emeraldine base is transformed by the proton-induced spin unpairing mechanism into a chemical structure with only one unpaired spin per repeat unit but with no change in the number of electrons [146,147,149, 150,160-162]. The outcome of this process is the formation of a polaron lattice that has a smaller repeat unit compared to the original emeraldine base and which allows the delocalization of the π-electrons along the chemical backbone and thus metallic-like conductivity.

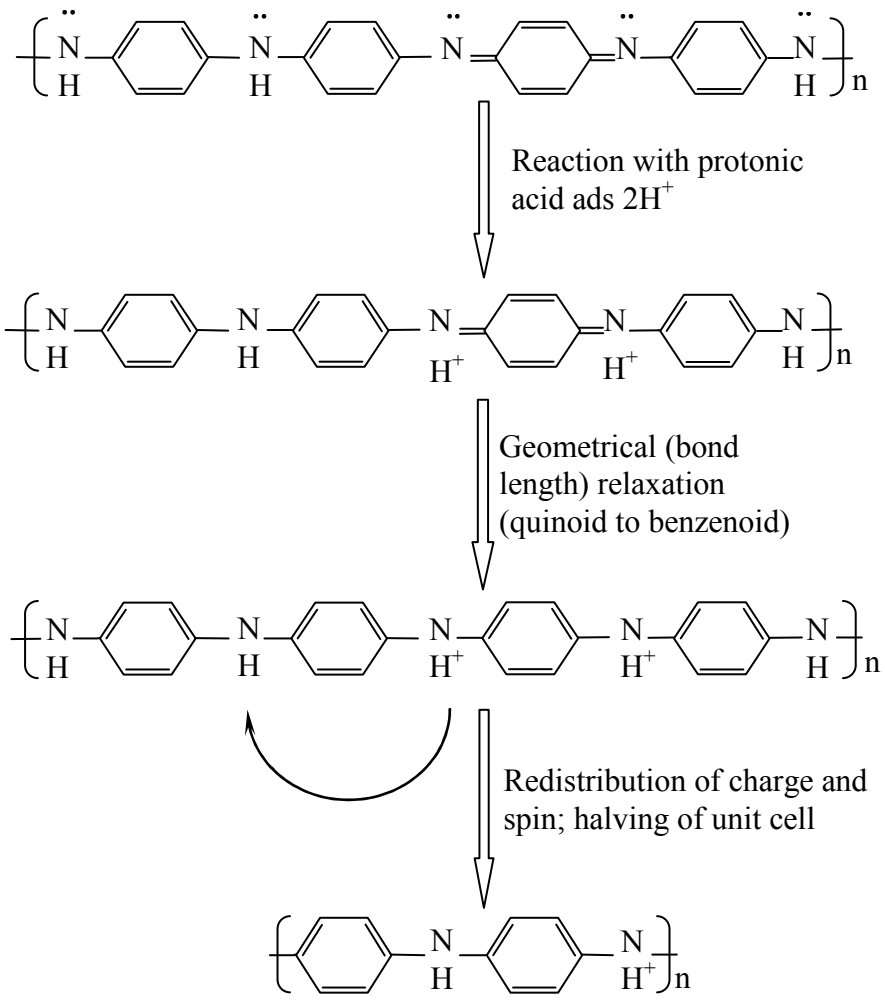

Figure 10. Protonation induced charge unpairing in polyaniline. The counterion display is omitted from the schematic.

Studies over the properties displayed by the emeraldine resulted after different methods of preparation revealed that there are two distinct classes [222-224]:

1) Class I is characteristic to emeraldine generated from solution in the protonated salt form (ES-I), and then converted to the respective unprotonated base form (EB-I) through treatment with a strong base. This class of emeraldine polymers displays substantial crystallinity in the ES-I form but is essentially amorphous in the EB-I form.

2) Class II materials are obtained when the polymer is synthesized in the unprotonated base form (EB-II) and subsequently transformed to the protonated salt (ES-II) through treatment with a strong acid. The polymer displays crystalline behavior in the salt form, with a different crystal structure than ES-I, and a partially crystalline structure in the non-protonated, EB-II form. In addition, the EB-II crystal structure can be generated by dissolving the EB-I type in an appropriate solvent (*e.g.* tetrahydrofuran (THF), dymethyl sulfoxyde (DMSO) or N-methyl-2-pyrrolidone (NMP) and casting a film from the respective solution.

Polyaniline was proposed by Ogura *et al*. [175] as a material able to undergo variation in conductivity in response to a change in both the concentration of CO_2 and humidity of the surrounding atmosphere. Water vapor, in fact, affects the doping and chemical structure of conducting polymers [191-195], which results in a change in conductivity, therefore allowing for the use of conductive polymers as humidity sensors [196-199]. A schematic of self-doping of polyaniline occurring in the presence of water is presented Figure 11-adapted from [175], following a mechanism proposed by Ogura *et al.* [175,177] in the case of a polyaniline derivative.

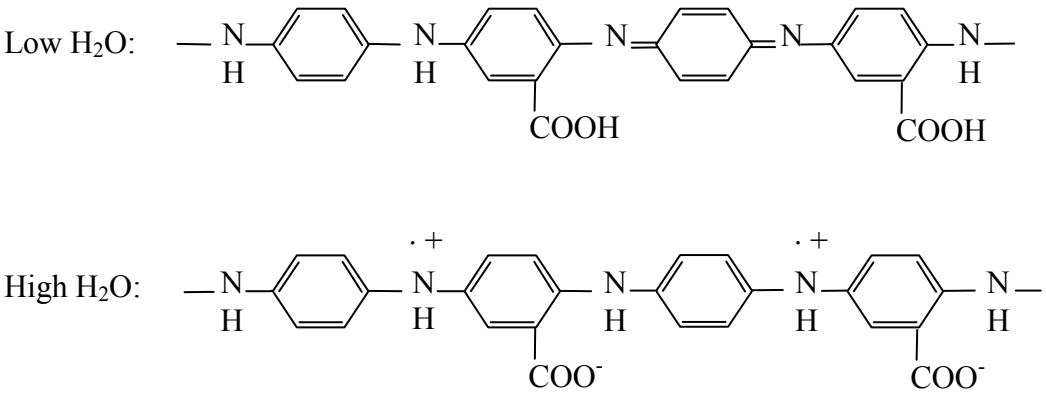

Figure 11. Self doping of emeraldine base.

The influence of water on polyaniline has been investigated in studies performed on polyaniline derivatives like poly(*o*-phenilene diamine) PoPD, poly(*o*-aminophenol) PoAP, poly(m-phenilene diamine) (PmPD) and poly(*o*-toluidine) PoTD. In all the above cases the variation of conductivity of polyaniline derivative polymers as a function of water vapor is not linear. The linearity can be achieved in some particular cases if the polyaniline derivatives are added to poly(vinyl alcohol), generating thereafter a composite polymer mixture [175,177-180,195,198-203]. Ogura *et al.* [198] suggested that a linear response of the polymeric mixtures appeared when the polyaniline derivatives displayed fibrillar morphology, whereas non-linear response was produced by a granular morphology. The growth of fibril-like structure was possible due to a higher solubility of some polyaniline derivatives in their respective solvent (*e.g.* DMSO). In addition, the fibril-like morphology allowed for a greater dispersion of water within the polymer composite [198,199].

An interesting observation was that the polyaniline derivatives provided the sensitivity to water vapor concentration although they were minor constituents in the polymer composite [175,177-180,198-200,204,205]. For example, additions of just 0.23-0.28 vol.% polyaniline to PVA provided a linear response and the response became non-linear when more than 4.3 vol.% polyaniline was added [199]. In addition to this property, the conductivity of the composite polymer changed by 1 to 2 orders of magnitude when the relative humidity increased from 11% to 98% [175,177,196,198, 199].

Another study performed by Ogura *et al*. [199] on different polyaniline derivatives revealed that composite polymers in which the water molecules were strongly

bound to the PVA were less affected by the variations of external humidity. Ogura suggested that this property aroused because the conductivity of the polymer was dependent on interaction between a protonic acid (*e.g.* toluene-*p*-sulfonic acid) and polyaniline. During this interaction, the weakly bound water molecules promoted the protonation of imine-nitrogen sites and produced a subsequent increase in conductivity. A decrease in humidity reduced the amount of weakly bound water molecules in the composite matrix chains, an event that was followed by a subsequent decrease in protonation and electrical conductivity. In the extreme cases when the external humidity level was very low, all the water became strongly bound to the PVA and polyaniline formed the insulating emeraldine base. Ogura *et al.* [199] showed that the conductivity loss was less prominent for the polyaniline derivatives that displayed strong attraction to water molecules, rendering these composites a lesser dependence of their conductivity to the relative humidity. With this respect, Ogura *et al.* [175,177-180] showed that for a desirable output of the sensor, the water molecules should be as much bound as possible to the PVA matrix.

Travers *et al*. [191-193] and Angelopoulos *et al.* [194] on the other hand, attempted to explain the effect of water on electrical conductivity of polyaniline. The above-mentioned groups also observed an increase in conductivity of both "dried" and "exposed to water" emeraldine base that was suddenly exposed to higher level of water vapor pressure. The increase in conductivity was found to be dependent upon the pH level at which the emeraldine base was previously equilibrated. In Table 2 are presented the published values, for emeraldine base samples equilibrated at pH = 6.0.

Table 2. Conductivity increase produced by an increase in relative humidity for emeraldine base sample equilibrated at pH = 6.0; *For the sample whose conductivity increased by several orders of magnitude the author, W.R. Salanek estimated that a response was governed by the preparation procedure which allowed for virtually removal of all the water during the dynamic pumping. The latter data represented a personal communication of W.R. Salanek to the authors of reference [192].

Conductivity Change	**RH Change**	**Reference**
Several orders of magnitude	N/A*	Reference 6 in 192
1-2 orders of magnitude	11% to 98%	175,177,196,198,199
1.5 orders of magnitude	0 to 100%	191
62%	0 to 65%	192
17%	0 to 17%	194
22%	0 to 17%	192
25%	21% to 42%	192

Studies performed over the magnetic, optical and transport properties of polyaniline [145,161,163,165,172,174,190,206] described the material as composed of segregated metallic islands (*i.e.* ~250 Å diameter) embedded in an insulating matrix. Angelopoulos *et al.* [194] noticed a rapid increase in conductivity upon exposure to water vapor followed by a slow decrease in conductivity under dynamic vacuum, and ascribed the event to the above mentioned morphology. Angelopoulos has proposed that when emeraldine base is exposed to humidity, the absorbed water decreases the insulating interparticle resistance before diffusing slowly within the metallic islands, the latter step being responsible later for only a minor increase in conductivity. During the dynamic pumping, however, the water in the interparticle region is replenished as nearly as fast as it is removed, leading to a slow increase in resistivity during the drying step.

However, the model proposed by Angelopoulos *et al.* [194] would imply a necessity of different kinetics for the absorption and desorption process of water

molecules in polyaniline, otherwise the time response of the electrical conductivity of the material would be identical in both stages (*i.e.* exposure to water and dynamic pumping). This shortcoming of the theory proposed by Angelopoulos leads to the idea that the bound and free water molecules play a role in this process. Travers *et al.* [191-193] attempted to explain the mechanism through which the presence of water molecules favors conduction in polyaniline, but do not explain why the conductivity change is fast in the adsorption and slow in the desorption process.

Following the model and notation proposed by MacDiarmid, Travers *et al.* [191-193] ascribed the reduced forms of polyaniline (*i.e.* the 1A and 1S sites) to NH and NH_2^+ sites respectively, and the oxidized forms (*i.e.* the 2A and 2S sites) to N= and NH^+= sites. The cross-over between forms in the same group of oxidation state (*i.e.* between the reduced forms and oxidized forms respectively) follows acid base reactions with characteristic constants pK_1 and pK_2 respectively, as it is schematically presented in Figure 12- adapted from [191,192].

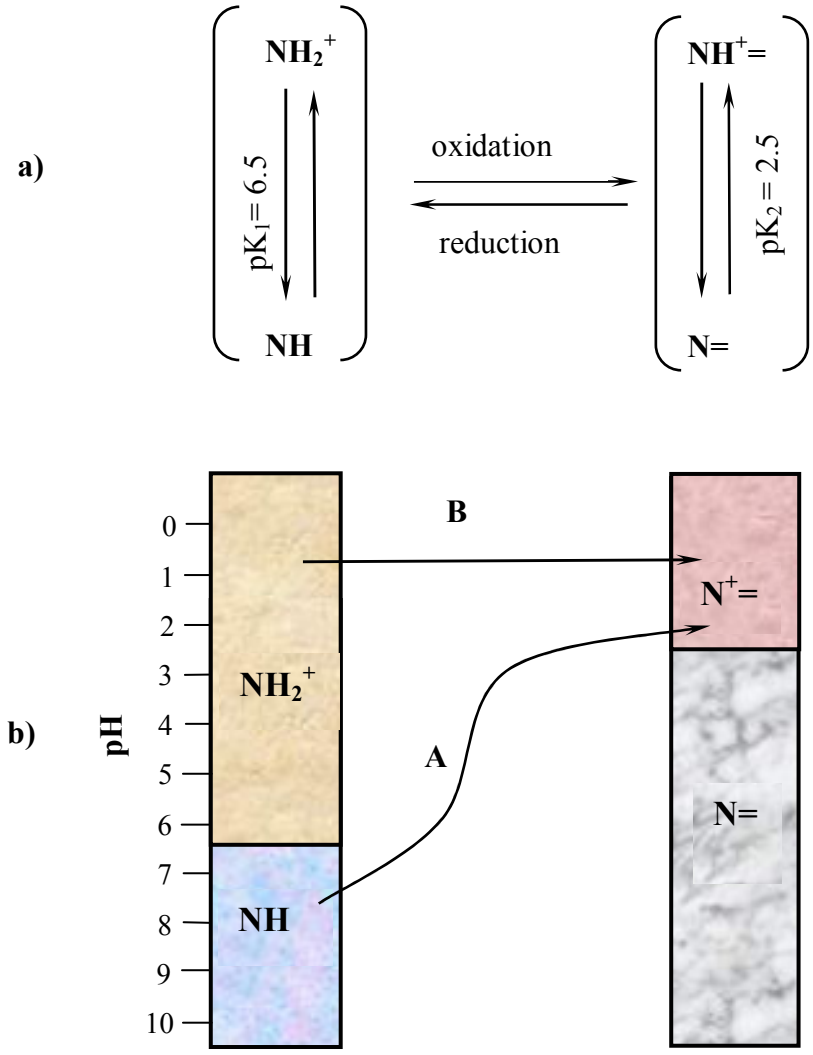

Figure 12. a) Schematic representation of the acid-base and redox reactions between different forms of polyaniline; b) Thermodynamical stability domains of the pH for the different forms of polyaniline.

The reduced form 1 is then a mixture of sites NH and NH_2^+, and the oxidized form 2 is a mixture of sites N= and NH^+=. The relative weight proportion between sites in the same form is governed by the pH at which the sample was previously equilibrated. Regarding the weight ratio of the two forms (*i.e.* 1 to 2), this is dependent upon the sample preparation procedure (*i.e.* amount of oxidant introduced, the place of preparation and time of mixing of the polymerization ingredients). All the latter conditions influence

the relative ratio of the reduced to oxidized sites. In summary, an emeraldine sample displays all the above sites enumerated by Travers and Nechtschein [191,192] in a proportion dependent upon both the redox state and the pH of the medium in which the sample was equilibrated prior to the conductivity measurements.

The process of conduction in polyaniline consists of an electron transfer, *i.e.* an electron removal from either site of the reduced form 1 (*i.e.* NH and NH_2^+) and its subsequent transfer to a site of the oxidized form, 2 (*i.e.* N= and NH^+=). Figure 12b displays the two possible routes of the electron transfer. If the electron follows the route A, then the process consists of a pure electron transfer:

-at the origin site:

$$NH - e^- \rightarrow NH^+= \quad (24)$$

-at the destination site:

$$NH^+= + e^- \rightarrow NH \quad (25)$$

Unfortunately, the origin and destination sites in the route A do not lie under the same pH domain and therefore, the thermodynamical instability makes the electron transfer process followed by route A highly improbable. Route B displays both sites under the same domain for a pH level below 2.5, therefore corresponding to the same thermodynamical stability. However, in this case, the protonation level of the two sites is different and the site NH_2^+ cannot lose an electron without losing a proton. The necessary proton in the electron transfer reaction of route B is borrowed from the water molecules near the NH_2^+ sites:

$$NH_2^+ + H_2O \rightarrow NH + H_3O^+ \quad (26)$$

Then the electron is removed from the NH site as described above, such that the water molecules help just unpin the charge carried by the NH_2^+ sites by temporarily accepting a proton. The conduction based mechanism proposed by Travers and Nechtschein [191,192] rests therefore in electron hopping between localized states, with a proton exchange-assisted conduction of electrons, (denominated by the group as "PEACE").

However, even though it seems to explain reasonably well the conduction mechanism in emeraldine base under the influence of humidity, the theory proposed by Travers *et al.* [191,193] is challenged by the impedance spectroscopy study performed by Javadi *et al.* [207]. In the latter study, the conductivity of emeraldine base was investigated as a function of frequency and exposure to humidity in the range between D.C. and 10-10^{10} Hz. The conductivity was found independent of frequency, even though this range of frequency spans from below to above the frequency responsible for proton exchange within the polymer. This fact led Javadi *et al.* [207] to conclude that the PEACE mechanism is not suitable for explaining the conductivity-humidity dependence of emeraldine base. Comparing the mechanisms proposed by Angelopoulos and Javadi [194, 207] on the one hand and Travers and Nechtschein [191,192] on the other hand, MacDiarmid [182] considers that the more likely origin of the water influence over the electrical conductivity in emeraldine rests in the effect of water on the beaches between the metallic islands, although the mechanism of this process is not yet well understood.

1.5. Impedance Spectroscopy: Description

In the present project, the conductivity of the composite conductive polymer film was investigated using impedance spectroscopy, a technique employed also by Zuo *et al.*

[208] in the case of polyaniline. Impedance spectroscopy implies the application of a small perturbation in the form of either a potential or current. The perturbation is a single sine wave or a superposition of a number of sine waves with different frequencies. From the applied perturbation and the subsequent measured response, the magnitude of the impedance and phase shift is determined. Since the technique is called spectroscopy the parameters are measured as a function of frequency of the applied perturbation. The voltage excitation in the present case is of the form: $U(\omega) = U_0 \times e^{i\omega t}$ and the recorded A.C. current response of the form $I(\omega) = I_0 \times e^{i\omega t+\delta}$. The impedance $Z(\omega)$ is therefore defined as a sum of a real and an imaginary part according to the equation (27) below:

$$Z(w) = \frac{dU(w)}{dI(w)} = |Z|e^{i\theta} = |Z|\cos\theta + iZ\sin\theta = Z' + iZ'' \qquad (27)$$

An impedance $Z(w) = Z' + iZ''$ is a vector quantity and can be plotted in the plane with either polar or rectangular coordinates, as displayed in Figure 13.

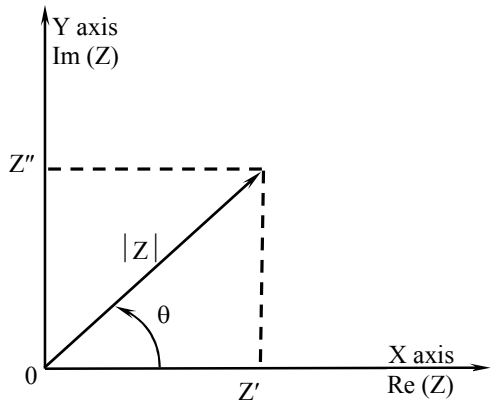

Figure 13. Impedance plotted as a planar vector using rectangular and polar coordinates.

The system is further described based on series and/or parallel circuits in terms of resistance, capacitance, constant phase element, Warburg element, inductance, *etc*.

Impedance spectroscopy helps understanding the processes that occur at interfaces, especially the changes in physical properties of the system (*i.e.* crystallographic, mechanical, compositional, electrical) as well as changes in electrical properties (*i.e.* polarization) by their effects on the electrical conductivity of the system. Macdonald [209] showed that the distribution of interfaces is a particular feature of solid-state electrolytic cells, where the junction between the electrode and electrolyte is considerably more complex than in the case of aqueous cells. In addition, in the solid electrolyte case, each interface will polarize in its unique way when the system is subjected to an applied potential difference. The rate at which a polarized region changes when the applied voltage is reversed is characteristic feature of each type of interface: slow for chemical reactions at the triple phase contacts between atmosphere, electrode and electrolyte, and relatively faster across the grain boundaries in the polycrystalline electrodes [209].

Impedance spectroscopy offers the advantage that the conductivity measurement is taken over a range of frequencies, which can allow for obtaining information on different conduction species and paths. These pieces of information are important in understanding and controlling the conduction mechanisms. Moreover, the results may indicate parameters, which should be used in a sensor interrogation for an optimum response. As an example, the results may show that higher sensitivity or better selectivity occurs if the measurement is made at a high frequency, fact that would require the presence of an oscillating circuit along with the sensor.

The parameters derived from an impedance spectroscopy spectrum fall generally into two categories:

1) Those pertinent only to material itself such as conductivity, dielectric constant, mobility of charges, equilibrium concentration of charged species and bulk-generation recombination rates;

2) Those pertinent to an electrode-material interface, such as absorption-reaction rate constants, capacitance of the interface region and diffusion coefficient of neutral species in the electrode.

Capitalizing on the advantages displayed by the impedance spectroscopy technique, however, can be difficult due to possible ambiguities in the results interpretation. This fact arises from the choice of the equivalent circuit, which consists of a sum of ideally lumped-constant properties. In reality, all electrolytic cells are distributed in space, and their microscopic properties may be in addition independently distributed, rendering the equivalent circuit ineffective in interpreting the electrical response. It is often found that $Z(\omega)$ cannot be well approximated by the impedance of an equivalent circuit containing only a finite number of ordinary lumped-constant elements (resistances, capacitances and inductances). Therefore, in order to take care of the distributed properties, the distributed impedance elements (so called constant phase elements-CPE) are introduced in the equivalent circuit. The resistance R in the equivalent circuit stands for the lump resistance of the conductive path, therefore a given resistor in the circuit may stand for either the bulk conductivity in the material or the chemical step associated with an electrode reaction. A capacitance and inductance can be attributed to regions of space charge polarization as well as with specific adsorption and electrocrystallization process at electrode. The CPE element can account for the distribution in space of the microscopic material properties, for distribution of the

conductive paths independently to one another and for the nonuniformity of the contact between electrodes and material. Macdonald [209] showed that an equivalent circuit involving only a finite number of ordinary lumped-constant elements could not adequately approximate the electrical impedance. Each particular CPE element has associated with it both resistor and capacitor values due to the resistance distribution over a specific material volume.

Impedance spectroscopy is the technique used in the current project to determine the electrical conductivity of the film and to assess the way this conductivity changes with time. The technique gives information on the way the electrical conductivity depends on CO_2 and H_2O partial pressures.

1.6. Project Objective

The objective of the current project is to evaluate the detection of carbon dioxide by measuring the conductivity change of the composite thin film of emeraldine base and poly(vinyl alcohol). In a first attempt, the results reported by Ogura *et al.* [175,177-180, 198,199] will be investigated, employing a sensor developed in a similar configuration. The assessment of the sensor performance will be accomplished by studying the effect displayed by CO_2 partial pressure on the transport properties, sensitivity, response time, selectivity and repeatability of polyaniline based thin film. In addition, the effect of the humidity level on the sensitivity and selectivity of the sensor will be evaluated. If the results of these studies will prove unsatisfactory, other routes to improve the sensor performance will be attempted with the aim of improving the CO_2 detection characteristics and in this way elucidating the possible applications of this sensor.

2. EXPERIMENTAL SECTION

2.1. Suspended Sensor

2.1.1. Conductive Polymer Preparation

The preparation method of the polymer composite follows closely the procedure reported by Ogura *et al.* [177]. Polyaniline was synthesized by mixing 100 mL of 0.15 M aniline solution and 100 mL of 0.1 M p-toluene sulfonic acid (TSA) solution containing 0.15 M $(NH_4)_2S_2O_8$, and continuously stirring the mixture for 8 hours. The resulting precipitate was separated by filtration through filter paper No. 1 (Watmann Int.), then rinsed several times, first with methanol and second with a solution of 0.1 M TSA. The precipitate was dried at room temperature under vacuum for a period of 24 hours to obtain a dark green powder, in the form of TSA-doped polyaniline. The dried cake collected from the filter paper was treated in 3% NH_4OH aqueous solution for 8 hours in order to be converted to the insulating emeraldine-base polyaniline form. The base solution was filtered through filter paper No.1 (Watmann Int.) and the resulting dark blue precipitate dried for 24 hours under vacuum at room temperature. The dried emeraldine base powder was collected from the filter paper and stored in a closed vial in a desiccator. A sample of emeraldine base was extracted from the stock polymer and a heat-treatment process performed. The heat-treatment process was accomplished in a vacuum oven (VWR Scientific Products, Model 1410M) by inserting the sample in the oven preheated at 365°C and keeping it isothermally for 1 hour in helium gas atmosphere.

Stock solutions of emeraldine base-polyaniline and poly (vinyl alcohol) were prepared by dissolving 1 mg of EB-PAni and 6 mg of PVA in 10 mL of N-methyl-pyrrolidone (NMP), respectively. Samples were extracted from the stock solutions and a polymer composite mixture in ratio 1 to 5, EB-PAni to PVA generated.

Alternative methods of fabrication were also investigated. Variations in the procedures include the polymerization time (8, 12 and 24 hours), the cover gas during the fabrication (in a fume hood in air or in glove box under nitrogen), the heat treatment of the emeraldine base powders (no heat-treatment or heat-treated for one hour at 365°C in helium atmosphere), the EB-NMP solution concentration (0.01%, 0.1% and 1%) and the EB-NMP to PVA-NMP ratio (1/5, 1/4, 1/2). The specific conditions used are summarized in Table 3. The sensor performance was essentially the same for all the fabrication conditions investigated.

Table 3. Alternative methods of fabrication employed. 8, 12, 24 represent the polymerization time (hours); the numbers in regular type indicates air and bold type indicates N_2; *-indicates that PVA with two different molecular weights (13000-23000 or 89000-98000) were used; **- indicates that PVA with three different molecular weights (13000-23000, 89000-98000 or 124-186000) were used.

Heat Treatment	EB-NMP concentration (%)	0.06% PVA-NMP			1% PVA-NMP		
		EB-NMP/PVA-NMP ratio			EB-NMP/PVA-NMP ratio		
		1/5	1/4	1/2	1/5	1/4	1/2
No HT	0.01	**8***,12,**24***	**8,24**	**8**,12,**24**	8	8	8
	0.1	8	-	8	-	-	-
	1	**8****,**24****	8, 24	**8,24**	**8****	-	**8**,24****
365°C	0.01	**8**,12,**24***	8	**8**,24	8	-	8
	0.1	-	-	8	8	-	-
	1	**8**,12,**24***	**8**, 24	8,24	**8****	8	**8,24**

2.1.2. Polymer Film Deposition and Interrogation

The electrode used for conductivity measurements was fabricated from titanium-gold sputtered in a comb-shape configuration on quartz substrate. The pattern consisted of a total number of 50 fingers, 25 on each side. A schematic of the sensor is presented in Figure 14 below. Each finger was 4 mm in length (f) and 200 nm in height (h) and presented an interdigitated space (d) of 40 μm to the adjacent fingers. Compared to the interdigitated electrode utilized in the current project, Ogura's group [177] comb-shaped microelectrode presented an interdigitated spacing of only 5 micrometers, which is about one order of magnitude smaller than that used in this work.

The interdigitated electrode was rigorously cleaned with acetone and distilled water and then introduced for a period of 30 min in "Piranha solution" (*i.e.* 3:1 ratio of 50% H_2SO_4 and 30% H_2O_2 aqueous solutions respectively), following a cleaning method reported by Revzin *et al.* [210].

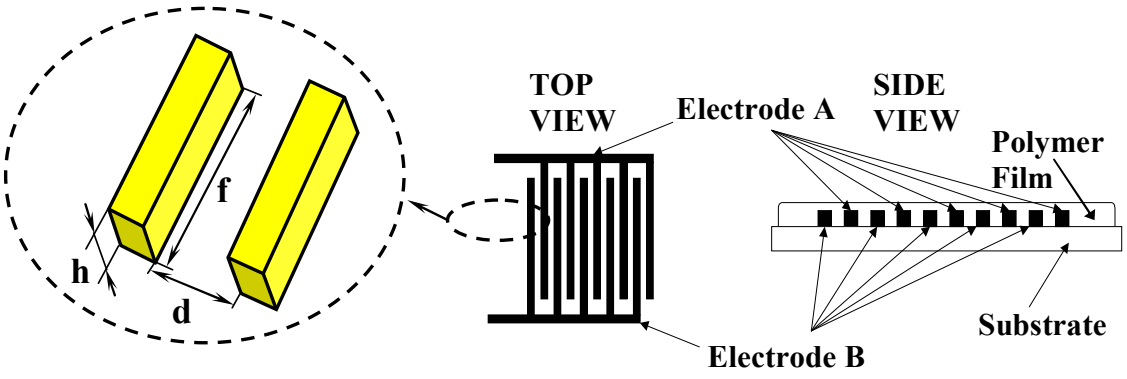

Figure 14. The sketch of the interdigitated electrode.

A quantity of 1 μL of stock solution was deposited on the interdigitated electrode in a dip-coating approach that was also followed by Ogura *et al.* [175,177-180,198,199].

The electrode having the polymer composite deposited was then placed inside a closed glass chamber and slowly dried under flowing argon gas atmosphere.

2.1.3. Experimental Setup

A schematic of the experimental arrangement is presented in Figure 15 . The glass chamber was partially filled with saturated solution of a salt that fixed the humidity level to a steady value. The humidity level fixed by supersaturated salt solution was displayed by the humidity sensor around the following means: ~60% for NaCl, ~30% for $MgCl_2$, ~4.5% for LiCl and ~1.5% for LiBr.

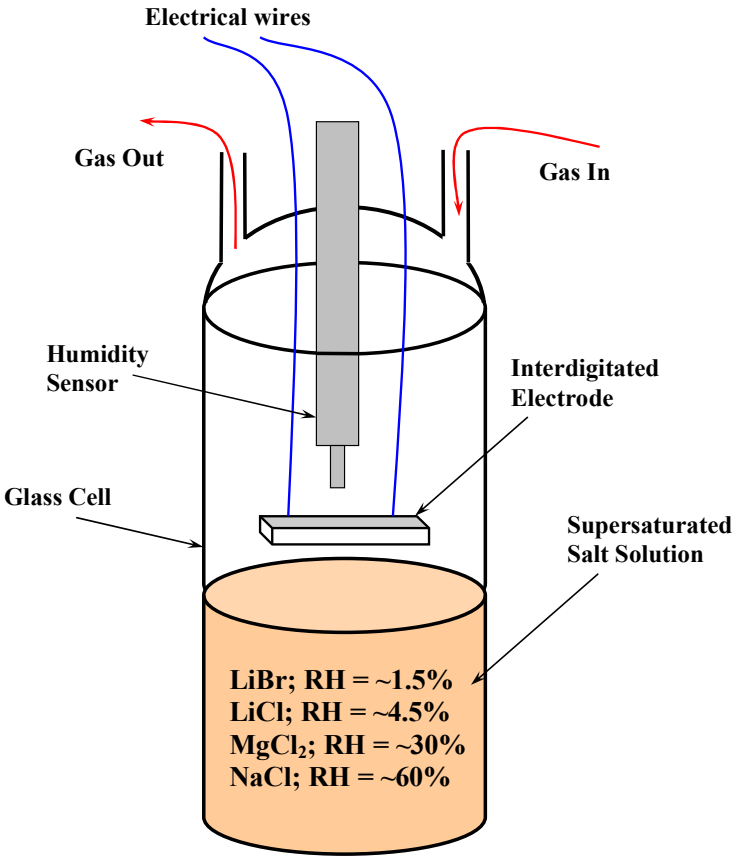

Figure 15. The setup utilized in conductivity measurements for suspended sensor.

The interdigitated electrode covered with the cast polymer composite film was connected with two alligator clips and suspended inside the glass chamber about two millimeters above the level of the supersaturated salt solution. All the time the relative humidity was monitored inside the glass chamber with a HMP35E humidity probe of Vaisala HM 138 humidity sensor (0.01 accuracy).

The other ends of wires were connected to the terminal of the Impedance Gain Phase Analyzer (Solartron model SI 1260) and the glass chamber was sealed. The first gas flowed inside the glass chamber was pure argon (99.9%, Air Gas Co.) and the impedance of the deposited polymer film measured by the impedance gain phase analyzer using a frequency range between 3.2×10^7 to 1 Hz. The measured data was fitted with the equivalent circuit displayed in Figure 16 and the conductivity of the film calculated inserting the total the resistance (*i.e.* $R = R_1 + R_2$) given by the equivalent circuit into equation (28):

$$\sigma = \frac{d}{49 \times h \times f \times R} \tag{28}$$

where f, h and d represent the finger length, height and interdigitated spacing respectively, given in Figure 14, and 49 represents the number of conductive paths between 50 fingers. The contribution to conductivity given by the material above the finger height and between the finger ends and the side of interdigitated electrode was neglected.

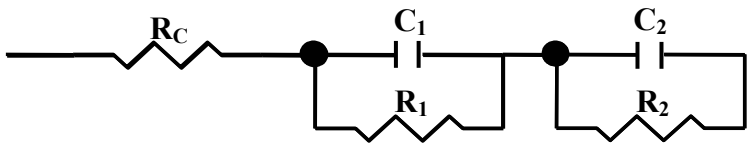

Figure 16. The equivalent circuit schematic associated with the measured data in the suspended sensor case; This circuit will also be employed in the immersed sensor case.

In Figure 16, R_1 and R_2 represents respectively the two variable resistances of the equivalent circuit that fits the measured data, whereas C_1 and C_2 represent the capacitances. The contact resistance R_C was kept constant at 4.5 ohm during the fittings.

Following the film resistance stabilization to a constant value, the flow of pure argon gas was suspended and a mixture of Ar + 5% CO_2 from a separate tank (Air Gas Co.) was flowed inside the glass chamber. The Ar + 5% CO_2 gas mixture was flowed until the resistance of the thin film stabilized to a new value, and then a new cycle was restarted by flowing pure argon gas.

2.1.4. Experimental Conditions for Material Analysis

Fourier transformed infrared spectroscopy (Perkin Elmer Spectrum GX FTIR Spectrometer) was performed on powdery samples of emeraldine base polyaniline in KBr mode. Equal portions of emeraldine base from the stock powder were distributed in individual vials and a heat treatment performed for each sample. The heat treatment consisted in maintaining each sample in oven for one hour in helium atmosphere at temperatures of 100°C, 150°C, 200°C, 250°C, 300°C or 365°C.

UV-Visible spectrophotometry analysis (CARY 3E UV-Visible Spectrophotometer) was performed by adding two drops of 3% emeraldine base polymer solution in NMP in a 10 mL cuvete of pure NMP.

Differential scanning calorimetry analysis (TA Instruments 2910 Differential Scanning Calorimeter) was performed on emeraldine base powder samples. The analyzed sample was kept isothermal for 30 minutes at 100°C and then ramped at 20°C/min to 400°C. After cooling down to the room temperature, a second run of the experiment was restarted in the same described conditions.

X-ray diffraction (Rigaku DMaxB Diffractometer) was performed on emeraldine base sample powders heat-treated for one hour in a helium atmosphere at temperatures of 100°C, 150°C, 175°C, 205°C, 225°C, 245°C, 275°C, 300°C or 365°C. The scan range (2θ) was 5-45° at a scan rate of 5° min^{-1}. To calculate the full width half maxima (FWHM) value, a horizontal base line was drawn at the base of the peak in each XRD spectrum and the horizontal width at half distance from the peak base to the peak crest measured. In calculating the half width over height value (HW/H), the ratio of half the width of the base line over the full height of the peak was computed. The peak height was considered as the length spanning from the base line to the peak crest.

For the assessment of the amount of water incorporated by poly(vinyl alcohol), three glass slides (Corning, 22 × 30 mm) were scrupulously cleaned with acetone, warm water and soap, rinsed with deionized water and then introduced for 30 minutes in a Petri dish containing Piranha solution. The Piranha solution was in the same concentration and ratio as the one used for interdigitated electrodes cleanup procedure [210]. The cleanup procedure was finalized through abundant deionized water rinse. The cleaned slides were placed on a clean Petri dish and dried at a temperature of 100°C for one hour on the top of a hot plate inside a fume hood. The glass slides were then removed from the heat source and a quantity of 1.5 mL of a solution of 0.06% PVA in NMP (*i.e.* to adhere

strictly to the concentration reported by Ogura *et al.* [175-180,196-199]) was deposited on each individual glass slide. The stock solution of PVA-NMP was previously generated following a method described by van Zandvoort *et al.* [211] by dissolving a quantity of 6 mg of PVA, MW = 13,000-23,000 in 10 ml NMP and heating this mixture to 80°C under continuous magnetic stirring until an optically clear solution was obtained. Attempts to dissolve PVA at any molecular weight in NMP without heating the mixture at a temperature of 80°C proved to be unsuccessful. Ogura *et al.* [175-180,196-199] had not indicated that such heating was performed. The slides having the PVA-NMP mixture were placed in an empty glass cell of the type depicted in Figure 15 and NMP-plasticized films of PVA produced by evaporation of NMP under flowing pure argon at room temperature for 24 hours. After the solvent evaporation, each glass slide was heated for one hour at a temperature of 70°C to remove any remained moisture in PVA. Each slide was then individually weighted and placed in a closed glass cell 2 mm above a supersaturated solution of $MgCl_2$ in water, in which a humidity of ~30% was established. At all times, pure argon gas was flowed in the glass cell, in order to reproduce as close at possible the humidity and gas flowing conditions encountered during the measurement taken with emeraldine base-PVA composite films. At regular time intervals, the glass slides were removed from the glass cell and weighted, the water absorption characteristic being generated for each individual slide in the respective humidity level. Each glass slide was then dried in an empty glass cell under argon gas flowing for 24 hours, dried at 70°C for one hour and weighted. The water absorption was then generated in other humidity levels fixed by NaCl and LiCl supersaturated solutions (~60% and ~4.5% relative humidity respectively).

2.2. Immersed Sensor

2.2.1. Conductive Polymer Preparation

Emeraldine base polyaniline MW = 5000 was purchased from Aldrich and treated in 3% NH_4OH aqueous solution for 8 hours. The solution was filtered through filter paper No.1 (Whatmann Int.) and washed with several portions of methanol and deionized water. The resulting precipitate was dried for 24 hours in vacuum oven at room temperature and the dried polymer collected in a closed vial and stored at room temperature in a dissecator. No heat treatment was performed on the emeraldine base powder. Stock solution of 3% emeraldine base in NMP (*i.e.* a concentration recommended by Zheng *et al.* [212]) was prepared by dissolving 0.3 mg emeraldine base in 10 mL NMP, and stirring the solution with a magnetic stirrer on the top of a magnetic plate at room temperature.

2.2.2. Polymer Film Deposition and Interrogation

The interdigitated electrode used for conductivity measurements was of the same type as the sensor employed in the suspended sensor measurements (*i.e.* Figure 14), only that the finger dimensions and interdigitated spacing differed. Each finger had a length (f) of 3 mm, height (h) of 120 nm and an interdigitated spacing (d) of 15 μm to the adjacent fingers. The interdigitated electrode cleaning and deposition procedures followed the same methods previously described in the suspended sensor case.

2.2.3. Experimental Setup

A schematic of the experimental arrangement is presented in Figure 17. The beaker was partially filled with pure deionized water. The interdigitated electrode covered with the cast polymer film was connected with two alligator clips and the working area immersed in water. The impedance measurement was performed on same Impedance Gain Phase Analyzer as in the suspended sensor case for an identical frequency sweep. In the immersed sensor case however, the detection of carbon dioxide was assessed by exposing the sensor to two different conditions: immersing it in pure water of measured pH ≅ 6.00 and in aqueous carbonic acid solutions of various pHs lower than 6, with the lowest pH measured 3.95. During the impedance measurements, the pH level of the aqueous solution was monitored inside the beaker with Accumet Research AR 50 pH meter (0.01 accuracy).

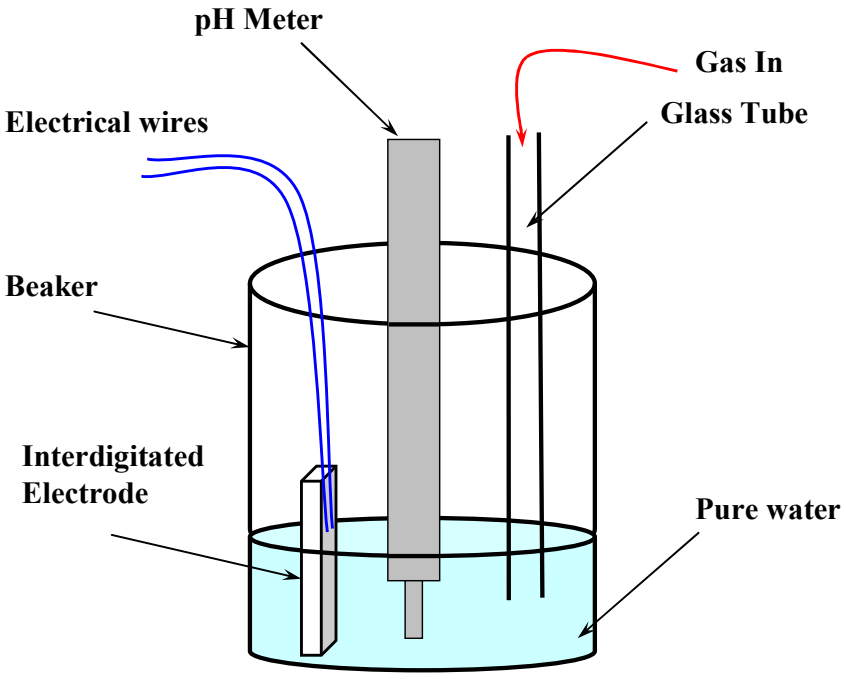

Figure 17. Experimental setup for the conductivity measurements in the immersed sensor case.

2.2.4. Measurement Conditions

The conductivity response as a function of pH of the protonating solution was performed by immersing the interdigitated electrode in a beaker containing aqueous hydrochloric solution of various pHs ranging from 6.00 to 0.25, with 0.25 pH units decrement. Impedance measurements were taken in this configuration and the value of the film total resistance extracted from the equivalent circuit fit.

In the immersed sensor case, the measured data is fitted with an equivalent circuit displayed in Figure 16 or in Figure 18. The conductivity of the film was calculated by inserting the total the resistance given by the equivalent circuit into equation (28).

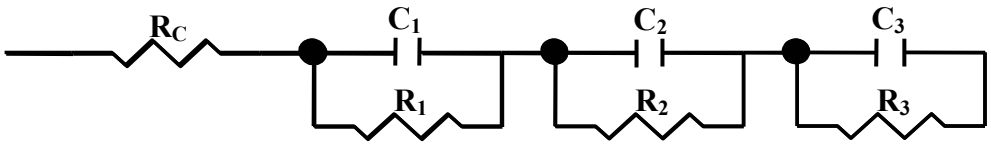

Figure 18**.** Equivalent circuit schematic for the immersed sensor case.

The equivalent circuit displayed in Figure 16 (two series of parallel R-C elements) was found suitable for fitting just a spectrum displaying a single semicircle, characteristic to a single conduction mechanism activated. This single mechanism was active between pH = 6.00 and pH = 5.03 exclusively for the sensor described in this project. The equivalent circuit presenting a sequence of three R-C elements, displayed in Figure 18 was used for fitting an impedance spectrum composed of two semicircles, characteristic to two conduction mechanisms based on electron-transfer. These two conduction mechanisms corresponded to a range of pHs between 5.03 and 0.25 inclusively. In this case, the total resistance of the polymer film was calculated by grouping the three individual resistances into two groups of resistances according to the capacitance range of

the respective element. The high frequency capacitance range was 10^{-7} F to 5×10^{-9} F and the low frequency capacitance range was 1×10^{-5} F to 10^{-7} F.

In the case of a spectrum displaying a single semicircle, in which case the equivalent circuit displayed in Figure 16 was employed, R_2 (also denominated $R_{low\ frequency}$) was taken as zero since there was no physical representation in the measured data for such a resistor. Therefore, the total resistance of the sensor was calculated as a summation of the two resistances given by the equivalent circuit, both of which were in the high frequency range. Following the impedance measurements in hydrochloric acid, the sensor was inserted for an hour in 3% aqueous solution of NH_4OH in order to convert the emeraldine salt to emeraldine base.

The assessment of the sensor response to carbon dioxide was accomplished by performing impedance measurements with the interdigitated electrode containing emeraldine thin film immersed in pure water or in pure water through which Ar + CO_2 mixture was bubbled (*i.e.* carbonic acid solution). In subsequent experiments, the impedance measurements were taken with the interdigitated electrode in pure water while bubbling purified or unpurified argon gas, or in carbonic acid solution with no bubbling performed during measurements. The purification of argon gas was performed through capturing the gas resulted by bubbling the argon directly from a gas cylinder (Air Gas Co. supplier, purity 99.9%) through a one molar solution of aqueous sodium hydroxide.

To evaluate the possibility that the carbonium ion induces complexation in imine sites, an emeraldine base film from the same stock solution was deposited on a glass slide, dried under vacuum at 45°C for 24 hours and then equilibrated in water for one hour. In this time, the film peeled off the glass slide. An FTIR measurement was taken

for this film and then the film was reintroduced in water where pure CO_2 was bubbled for 10 minutes, of measured pH = 3.95. The film was removed from water, tapped with Kim wipe to absorb the moisture and an FTIR measurement was taken immediately. The time spent by the film outside the carbonic acid solution before the FTIR spectrum was taken was less than 15 seconds, the time necessary for mounting the film in the FTIR holder.

In order to assess whether the lack of complexation of imine sites is due to the inherent NMP content in the film, an acid-base treatment was performed to the emeraldine film and the respective FTIR spectra collected at different pHs generated by HCl in water: starting from pH = 4 down to pH = 0.25 with 0.5 units decrement. The film was re-equilibrated in 3% NH_4OH for 30 minutes to convert the emeraldine salt to emeraldine base. The film was then removed from the ammonium hydroxide solution, rinsed with deionized water and equilibrated in water for 1 hour. An FTIR measurement was subsequently taken for this film after removal from water and also for the same film introduced in carbonic acid solution of measured pH = 3.95.

3. RESULTS AND DISCUSSION

3.1. Suspended Sensor

3.1.1. Experimental Results

The mechanism of CO_2 detection proposed by Ogura *et al.* [175,177-180] is displayed in Figure 19-adapted from reference [175]. The CO_2 reacts with water from PVA to create a carbonium ion (HCO_3^-) and protonates the polyaniline. Ogura reported that as the CO_2 partial pressure increases, the amount of protonation increases as well, leading to a higher electrical conductivity of the polymer film.

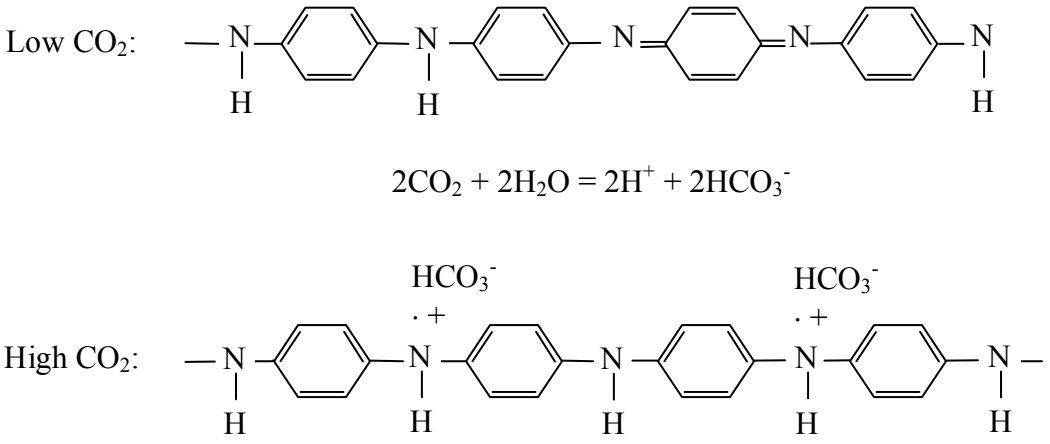

Figure 19. The CO_2 detection mechanism.

An example of conductivity measurement using impedance spectroscopy is presented in Figure 20, where the curve obtained is depicted as a depressed semicircle in the Z'-Z'' plot. The intercept of each semicircle with the horizontal axis represents the real part of the impedance recorded by the Impedance Gain Phase Analyzer, in fact the resistance of the emeraldine thin film in the respective measurement condition [209].

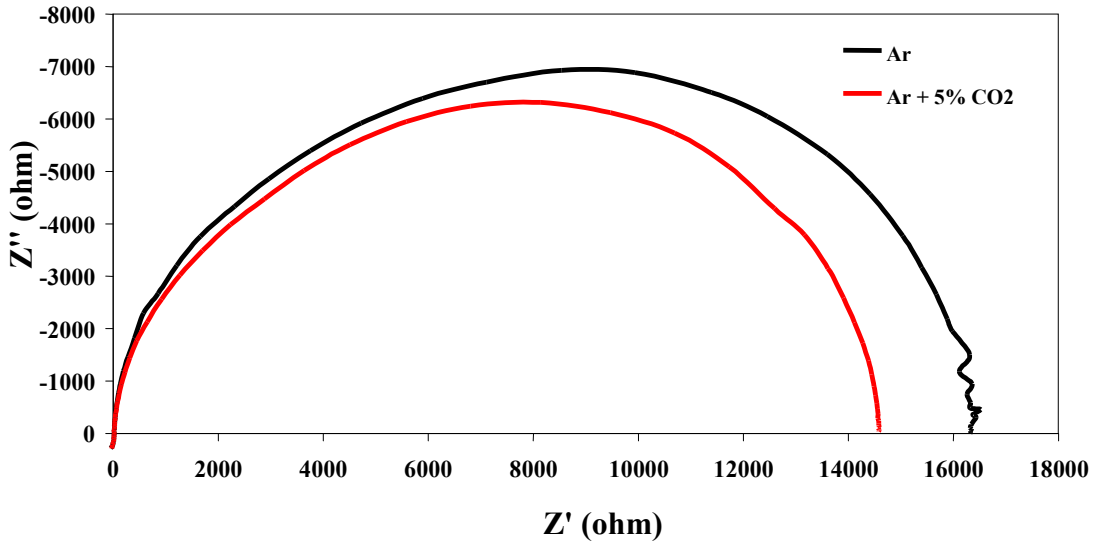

Figure 20. Impedance spectra recorded by Impedance Gain Phase Analyzer

The resistance variation during alternate flowing periods of argon and argon containing 5% carbon dioxide is shown in Figure 21. The resistance variation was plotted as a logarithm of the total resistance given by the equivalent circuit as a function of time. Graphs displaying the response of the sensor for the other cycles employed are attached in the appendix as Figure 21a-e. The stabilized resistances (*i.e.* plateau values), time and humidity values for the suspended sensor investigated are displayed in Table 4 for all the seven cycles (*i.e.* humidity levels) in which the sensor was tested.

Table 4. Measured values for the suspended sensor.

Cycle	Salt	Argon				Ar + 5% CO_2				ΔR/R (%)
		Time (min)	RH (%)	R (Ω)	LogR	Time (min)	RH (%)	R (Ω)	LogR	
1	$MgCl_2$	1131	31.55	19543.4	4.291	1491	32.44	18793.2	4.274	3.84
		1811	29.1	19678.9	4.294	3041	32.84	19230.9	4.284	2.28
		3373	29.87	20230.2	4.306	4720	31.11	19319.7	4.286	4.50
		4720	29.75	20137.2	4.304	5560	30.77	19498.4	4.29	3.17
		6173	29.85	20511.6	4.312	7013	30.4	19408.9	4.288	5.38
2	NaCl	2235	59.35	13867.6	4.142	3480	59.7	13001.7	4.114	6.24
		4500	59.22	14060.5	4.148	6405	59.85	13213.0	4.121	6.03
		7890	58.44	15205.5	4.182	9035	60.22	13931.6	4.144	8.38
		10835	58.15	15848.9	4.2	13805	59.72	14157.9	4.151	10.67
3	$MgCl_2$	2715	29.95	15848.9	4.2	1380	31.75	14962.4	4.175	5.59
		7005	29.74	16143.6	4.208	4065	30.87	15100.8	4.179	6.46
		12870	30.14	16943.4	4.229	9855	31.68	15310.9	4.185	9.64
4	LiCl	5730	3.67	21330.4	4.329	3180	4.26	18197.0	4.26	14.69
		10275	3.53	21379.6	4.33	7200	5.53	19543.4	4.291	8.59
		18690	3.34	21727.0	4.337	14490	4.55	19498.4	4.29	10.26
5	LiBr	8235	1.15	17060.8	4.232	5280	1.31	15310.9	4.185	10.26
		15250	1.13	17864.9	4.252	12480	1.24	16595.9	4.22	7.10
6	$MgCl_2$	7380	30.1	14157.9	4.151	4140	32.92	13273.9	4.123	6.24
		14505	30.44	14454.4	4.16	11265	32.02	13489.6	4.13	6.67
		21450	30.63	14927.9	4.174	17775	31.74	14028.1	4.147	6.03
7	NaCl	4110	59.55	11749.0	4.07	1590	60.03	11091.7	4.045	5.59
		7050	59.32	11995.0	4.079	5700	61.2	11091.7	4.045	7.53

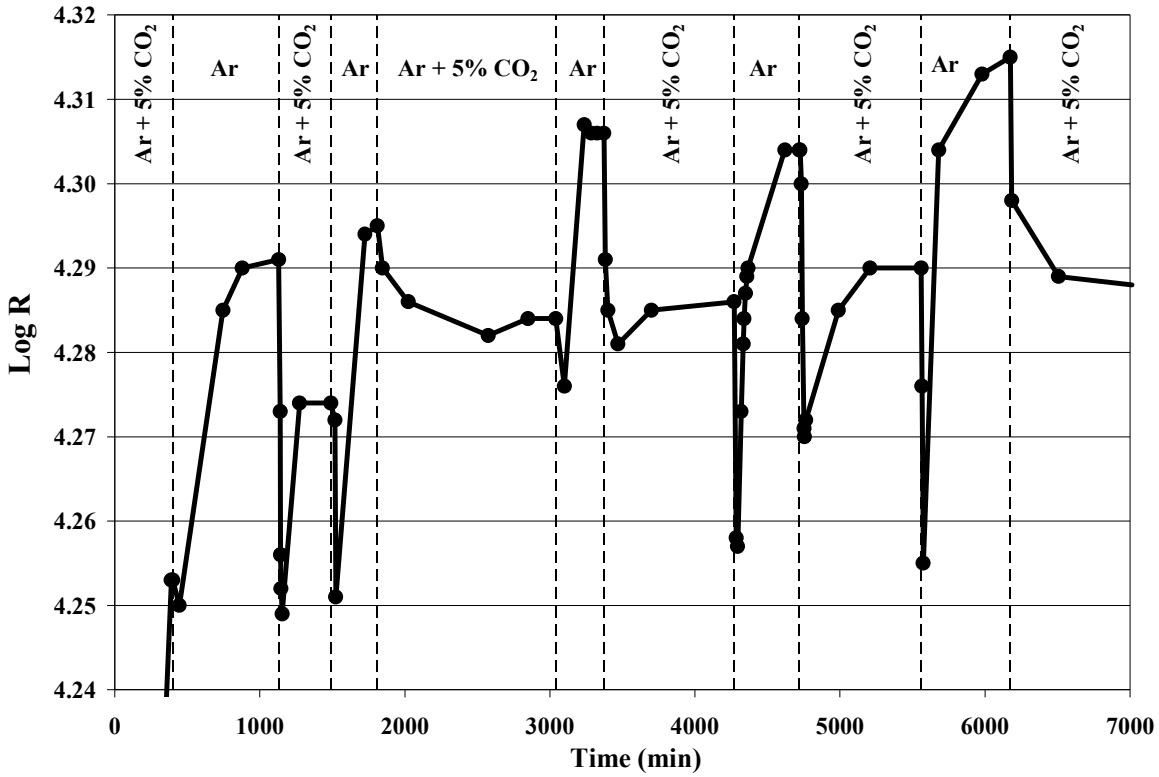

Figure 21. Resistance of the composite film in Ar and Ar + 5% CO_2 in a fixed humidity level of RH ~ 30% (cycle 1 in Table 4).

All these graphs (Figure 21 and Figure 21a-e) show that a change in flowing gas from Ar to Ar + 5% CO_2 resulted in a decrease of the composite film resistance, which according to Ogura *et al.* [175,177-180,198,199] could be explained by the inherent change of the emeraldine component of the composite film from the insulating emeraldine base to the conductive emeraldine salt following the reaction of carbon dioxide with water molecules provided by the PVA matrix. These graphs reveal also the undesirable drift of the sensor, in the way that the next measurement performed in the same gas resulted in a higher stabilized resistance. The drift was constant in the sense of resistance increasing with time, but the magnitude varied. The drift of the composite film

in the above-mentioned cycle 1 in Table 4 is presented in Figure 22. The drift was plotted as the logarithm of the average resistance of each plateau as a function of time.

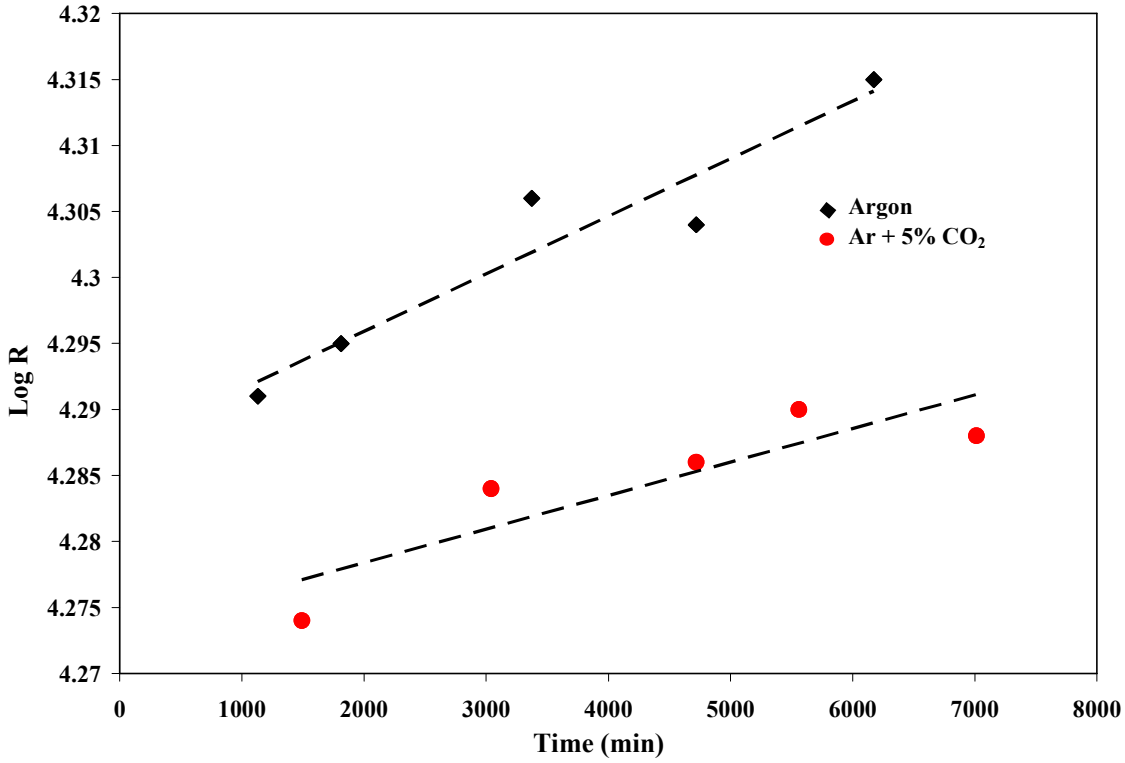

Figure 22. Trend of the resistance response of the composite film in Ar and Ar + 5% CO_2 at a fixed humidity level of ~ 30%.

The graphs of the resistance trend displayed by the sensor in the cases of other cycles employed are attached in appendix as Figure 22a-e. The drift had a greater magnitude in the case of argon gas flow than in argon containing 5% carbon dioxide.

Figure 21 together with Figure 21a in appendix show that immediately after the gas switch from one to another the film resistance recorded by the sensor sharply dropped. This event is visible only in these two figures since during the change, the line was disconnected from the controller and another line from the second cylinder connected, exposing in this way the glass cell with the room ambient. For the cycles 3 to

7 inclusively in Table 4, a second flow controller was calibrated and connected through a T switch, allowing identical flow rates to be passed through the test chamber, from the two cylinders. The event of sharp resistance drop was not recorded any more in the last five cycles.

Figure 23 displays the overall trend, for all the humidity conditions in which the sensor was tested. The overall trend is plotted as logarithm of the average resistance of each plateau as a function of relative humidity in all four humidity conditions: 1.5%, 4.5%, 30% and 60%. Figure 23 reveals that the resistance of the sensor does not stabilize to the same set of values when reverted to a humidity level already employed.

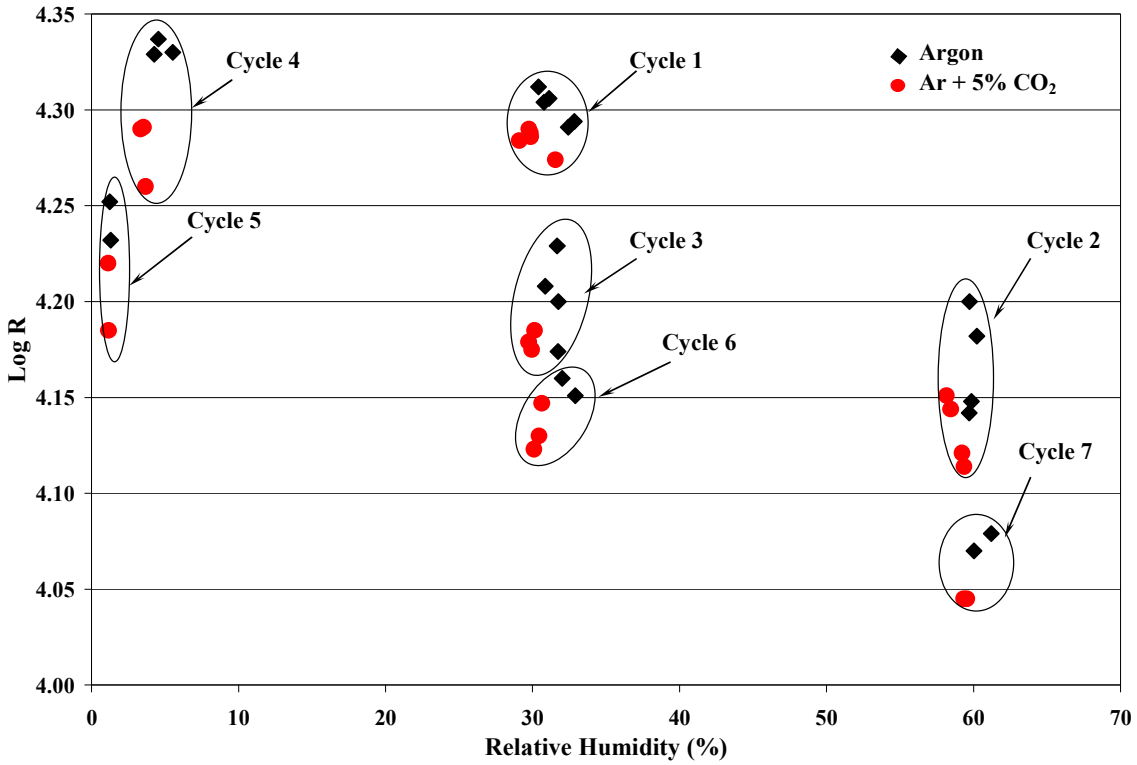

Figure 23. Logarithm of resistance versus relative humidity in argon and Ar + 5% CO_2 for the composite polymeric film. The film was tested more than once in both magnesium and sodium chloride respectively. Each particular cycle was circled for the ease of visualization.

Figure 24 displays the resistance difference between argon and argon containing 5% carbon dioxide. The resistance difference between argon and argon containing 5% carbon dioxide is plotted as a ratio of resistance difference in the two gases to the resistance displayed in argon, as a function of relative humidity.

The graph shows that the magnitude of response of the sensor is lower in the humidity level fixed near 30%. In this case, the ΔR/R response varies between 2.2% and 9.64%. In a humidity level of ~60%, the magnitude of response is placed between 5.59% to 10.67%. For a low relative humidity level fixed by LiCl and LiBr in the interval 1.1% to 4.5%, the magnitude of response is placed between 7.10% to 14.69%.

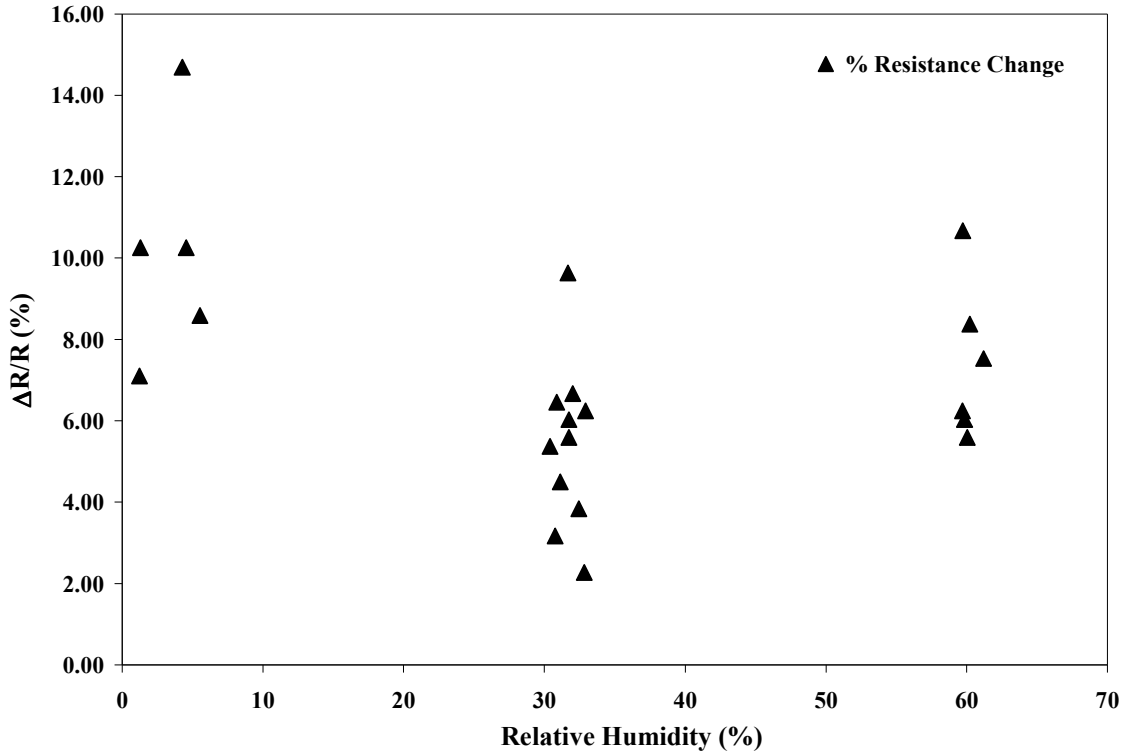

Figure 24. Resistance difference between Ar and Ar + 5% CO_2 (logarithmic scale).

A useful piece of information is the time necessary for the sensor to reach 90% of the response. An example of such variation is provided in Figure 25 for a humidity level

of ~30%. The 90% time response (t_{90}) was calculated as the time necessary for the sensor to reach 90% resistance between two adjacent plateaus (*i.e.* the one corresponding to argon gas and the other to Ar + 5% CO_2). This value was plotted as a function of number of gas reversal from argon to argon containing 5% carbon dioxide. Figure 25*a* in appendix shows an example of calculation of t_{90}.

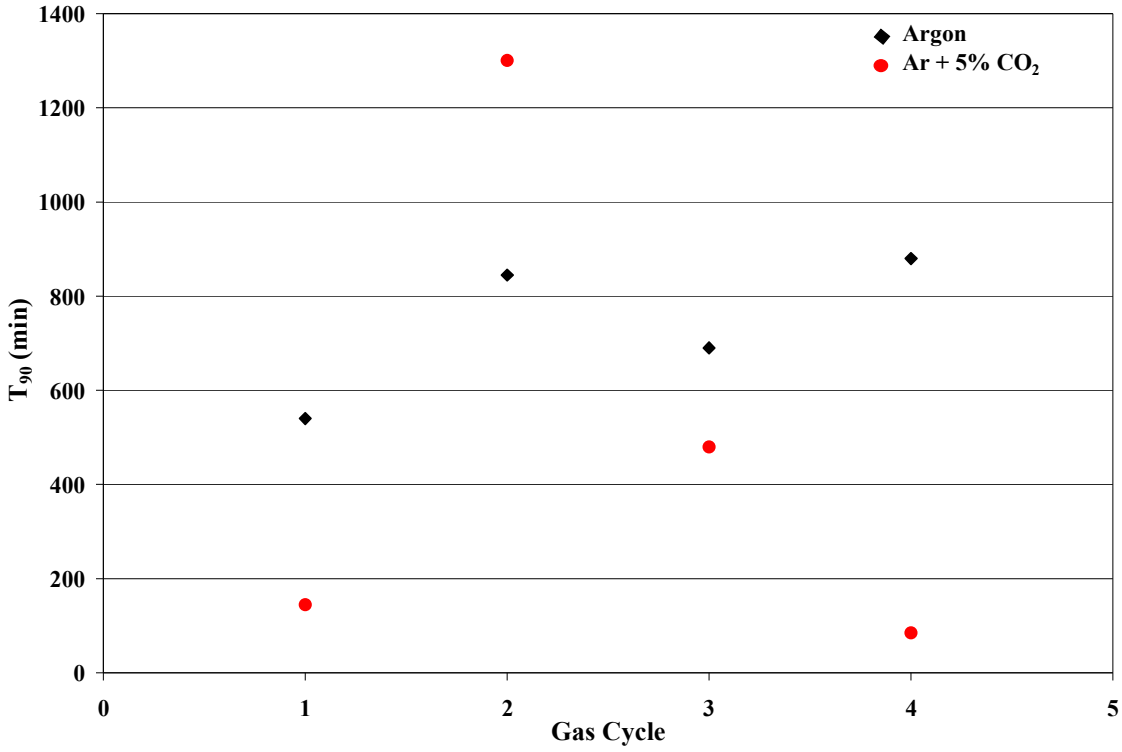

Figure 25. Response time (t_{90}) reached by the composite film for ~60% RH (cycle 2 in Table 4).

The inspection of the 90% response time data in Figure 25 and Figure 25a in appendix reveals that the change of gas from pure argon to argon containing 5% carbon dioxide resulted in a faster response (a shorter time necessary for the sensor to reach the plateau), even though there were exceptions in almost every humidity level. This fact complements the observation that the sensor output drifted. Otherwise, the faster

response during the exposure to carbon dioxide was not a surprise, this behavior being also observed by Ogura and his coworkers [175,177-180,198,199]. This phenomenon was ascribed by Ogura to the slow removal of the weakly bound water in the case of inert gas flow, which would prevent the resistance of the sensor to recover quickly the initial value. Travers *et al.* and Alix *et al.* [191,193] generated a similar observation pertinent to the existence of weakly and strongly bound water molecules in the polyaniline chains. However, the experimental method followed by Ogura *et al.* was different from the one in the present work, fact that permitted them to assign the behavior on the removal of the weakly bound water molecules from the composite polymer chain. The group used a vacuum pump to evacuate the chamber, allowing in a following step the admission of a specific amount of water vapor with carbon dioxide. Then the pressure in the glass cell was raised to one atm by admitting nitrogen and the measurement taken. This explanation offered by Ogura is not valid for the present work, since in the current project the polymer was not cycled between dry and wet states. Instead, the relative humidity was fixed by supersaturated salt solutions and just the gas flowed into the glass cell was changed between Ar to Ar + 5% CO_2. However, even in this work, the relative humidity varied between two gas flow conditions, in all the cases the relative humidity displayed in argon gas being higher up to 1.5% units than in the case of Ar + 5% CO_2. This difference was not due to the calibration of the flow controller since the flow rate was always the same (*e.g.* for the cycles 1 and 2 the same controller was employed, whereas in the cycles 3 to 7 two different controllers were utilized). In addition, the humidity sensor detected all the time a higher relative humidity when the gas from the cylinder containing 5% carbon dioxide was flowed through the glass cell.

The similarity of an apparently faster response time in the case of an exposure to a higher relative humidity, between this work and Angelopoulos [194], as well as the very slow response of the sensor (*i.e.* t_{90} that reached even 24 hours in this work when the sensor was exposed to just a percent variation in relative humidity and t_{90} that reached 10 hours in Angelopoulos *et al.* work [194] for a sensor cycled between dry state and ~17% relative humidity), suggest that in fact the sensor in this work detected just humidity variation.

Therefore, if in the current project the sensor did not detect a change in gas composition but just a humidity variation, the above models of dependence of emeraldine on relative humidity variation described by Angelopoulos *et al.* [194] and Travers *et al.* [191,192] could be well suited for an explanation of the poor results of the sensor in this work. In the same time, the same model, would explain Ogura's 1-1.5 order of magnitude response of their sensor. This magnitude response was detected by Travers *et al.* [191] as well as other authors (see reference 6 in 191). Salanek *et al.* obtained several orders of magnitude response in conductivity for a sample of emeraldine base with a specific fabrication history cycled between dry and wet states.

3.1.2. Sensor Performance Evaluation

In a similar work, Ogura *et al.* [177] reported a sensor able to detect CO_2 concentrations ranging from 50 to 10000 ppm (*i.e.* 0.005% up to 1% CO_2).

In the present work, the composite film was only tested for 5% CO_2 concentration. Since the decrease in the resistance of the film when changed from pure argon flowing conditions to argon containing 5% carbon dioxide, was placed in the range

of 2.2% to 14.6%, the composite film was not tested for carbon dioxide concentrations lower than 5%.

The purpose of the sensor is an important consideration in judging the response time. If the sensor is designated to monitor the food quality in a regular food package, a slow response time is acceptable. However, if the application involves sequential measurements, a fast response time in the range of seconds is required. Preliminary results showed that the sensor reached 90% of the response in a time of hours and the response was in most of the cases, faster when Ar + 5%CO_2 flowed through the glass chamber. At this stage of development, it is not clear which represented the factors that triggered a slow response time of the sensor and why the sensor response was apparently faster upon carbon dioxide exposure.

Preliminary results also showed that the sensor output was not stable, but drifted in time. The drift resulted in an increase of the composite polymer film resistance with time, but the values of the dynamic range fluctuated between the two conditions (Ar and Ar + 5% CO_2) and between different humidity cycles employed.

3.1.3. Comparative Results

Compared to the results reported by Ogura *et al.* [175,177] the sensor developed in the current project has less appealing features.

1) The 90% response of the sensor (t_{90}) in the current project (in the range of hours, up to more than 24 hours) is orders of magnitude larger than the respective values reported by Ogura *et al.* [175,177] (0.9 seconds for CO_2 flowing and 7.2 seconds for nitrogen).

2) The dynamic range of the sensor is much smaller (2.2 to 14.6% change in conductivity) between the two gases. In addition, the dynamic range is not stable, being arbitrarily smaller or greater between two similar flowing conditions and between different humidity levels employed. The sensor reported by Ogura *et al.* [175,177] presented a 1 to 1.5 order of magnitude increase in conductivity in response to carbon dioxide exposure.

3) The stability of the sensor is severely disrupted by drift. The sensor reported by Ogura *et al.* [175,177] was stable and presented a minimal drift over 35 days of testing.

The drift and variation of the dynamic range, slow response time and instability made the sensor developed in present work unsuitable for carbon dioxide monitoring applications. Given these unacceptable results, the focus of the subsequent development was aimed towards designing and testing of polyaniline films responsive to a concentration of CO_2 lower than 5%, and the quantification of the minimum concentration for a reliable response. In fact, the limited dynamic range of the sensor, the poor stability and slow response time provided suspicion that the sensor did not detect carbon dioxide at all, but in fact responded to humidity variations. The setup with the sensor immersed in water (*i.e.* the one to be employed in the following development of the project), along with the respective results, will clarify this issue. In the immersed sensor case, the amount of water to which the emeraldine base is exposed during carbon dioxide in and out stages will not be an influential factor on conductivity since the sensor being inserted in water is exposed to the same water level at all times.

3.1.4. Materials Characterization

Polymer characterization helps describing and understanding the structural and chemical modifications of the polymer film that accompany the conductivity changes. An extremely necessary piece of information is the determination of a change in intensity of the benzenoid to quinoid bands which provides information about the amount of protonation of imine nitrogen sites in the polymer backbone and therefore about the expected polymer conductivity.

3.1.4.1. FTIR Spectroscopy Characterization

A comparison of the FTIR spectra among emeraldine base powder not heat-treated and samples heat-treated for 1 hour at various temperatures in helium gas atmosphere is presented in Figure 26, with all the characteristic peaks marked on the graph. The spectra of samples heat-treated to temperatures intermediate between these two extremes are inserted in appendix as Figure 26a-e for a better visualization of the peaks.

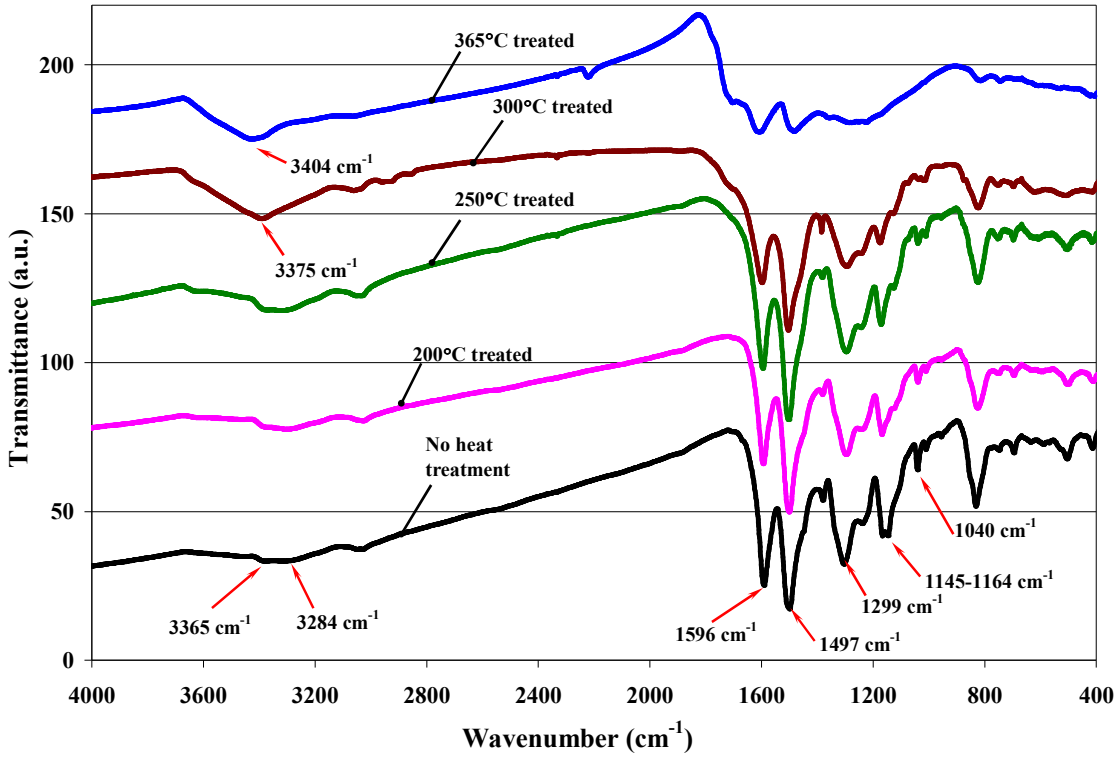

Figure 26. Comparison between FTIR spectra of emeraldine base without heat treatment and heat treated at various temperatures for 1 hour in helium atmosphere.

The peaks revealed by the FTIR spectra are displayed in Table 5 along with their respective vibrational mode already assigned in the literature [170,175,177,213-219].

The analysis of FTIR spectra reveals that emeraldine base suffers a gradual transformation as a result of heat-treatment over 250ºC. In fact, the analysis of the FTIR peaks demonstrates that subsequent to the treatment at temperatures higher than 250°C, the emeraldine powder becomes a mixture of leucoemeraldine and cross-linked emeraldine base.

Table 5. Characteristic peaks and vibrational modes assigned to emeraldine base

Peak (cm^{-1})	**Vibrational Mode**	**Reference**
3365	Free N-H stretching	212,213,216,217
3285	Interchain H bonded N-H	212,213,216,217
1590	C=C stretching-quinoid rings	170,175,177,212-218
1495	C=C stretching-benzenoid rings	170,175,177,212-218
1295	C-N stretching-aromatic amine	170,175,177,212,213,216-218
1145-1165	N=Q=N stretching	170,177,212-218
1040	Symmetric SO_2 stretching in	177

Scherr *et al.* [184] reported that emeraldine base cross-links if treated for 4 hours at 300°C and proposed that the cross-linking process is chemical in nature and occurs through a linkage between imine nitrogens that generate a phenazine-type structure. A schematic of the cross-linking proposed by Scherr *et al.* is presented in Figure 27- adapted from reference [184].

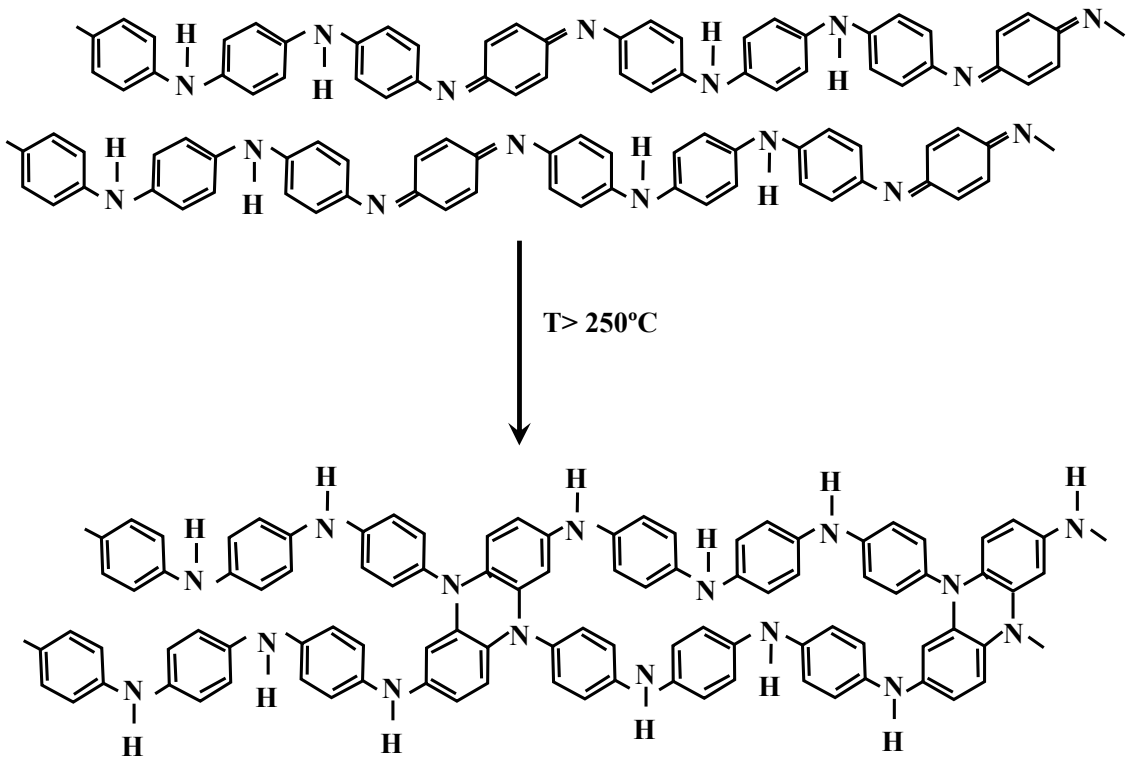

Figure 27. Schematic of the crosslinking process.

This behavior of cross-linked emeraldine was confirmed by Oh *et al.* [220] in a study aimed to identify the effects of cross-linking induced by both temperature and stretching in emeraldine base films. The latter report also revealed that the degree of cross-linking and the molecular weight of polyaniline employed have little effect on the conductivity in cross-linked polyaniline films. Chen *et al.* [215] also confirmed the chemical nature of cross-linking process occurring at temperatures of 150-300°C, showing that the process is responsible for the diminishing in the intensity of the peak centered at ~1160 cm^{-1} and attributed to N=Q=N stretching type vibration. In a following report, Milton and Monkman [221] reported that chemical cross-linking process rendered by treating the sample at temperatures greater than 180°C is responsible for the sample

hardening and insolubility in NMP. The latter group suggested that physical cross-links (chain entanglements) may also be present in a cross-linked sample. In a more recent report, Ding *et al.* [214] confirmed Milton and Monkman study showing that mainly the chemical cross-links between imine nitrogen sites accompanies the change in morphology of emeraldine base due to the thermal treatment performed in the range of 185-350°C. Ding *et al*. based their argument on the evidence of transformation of the multiple peaks centered at ~1160 cm^{-1} (*i.e.* peaks which are characteristic to a more ordered, resembling a partially crystalline structure) into a single peak of much lower intensity (*i.e.* a single peak representative to a fully amorphous structure. The chemical nature of cross-linking process, occurring through bonding between imine nitrogens, is consistent with the FTIR spectra in Figure 26. The multiple peaks having an infrared absorption in the range of ~1144-1165 cm^{-1} gradually diminish in intensity with increasing temperature and finally vanish for an emeraldine powder treated at a temperature of 365°C. In addition to the FTIR analysis, Ding et al. [214], Chen *et al* [215], Scherr *et al.* [184] and Monkman *et al.* [221] reported that once the emeraldine powder became cross-linked at high temperature, the powder could not be processed in appropriate solvents (*i.e.* DMSO or NMP) and strong acids (*i.e*. H_2SO_4). In this work, the powder heat treated at temperatures exceeding 250°C it is never completely soluble in NMP. The higher the heat-treatment temperature, the lower the solubility of the powder and less intense the blue color of the resulting solution. At heat temperatures over 300°C, the color of the solution obtained after the dissolution of the respective powder is no longer blue, (the color which appears after the dissolution of emeraldine base in NMP) but yellowish-brown, characteristic to the leucoemeraldine-NMP solution. In about 24

hours time, a residue of undissolved polymer sediments at the bottom of the flask. The dissolved polymer is actually the leucoemeraldine base (as determined by UV-visible spectrophotometry), whereas the undissolved one is presumably in the form of cross-linked emeraldine base.

The spectrum of emeraldine base for which no heat treatment was performed (*i.e*. the lower curve in Figure 26) displays two bands associated with N-H stretching vibrations: a broad band centered at ~3285 cm^{-1} associated with hydrogen bonded N-H stretching vibrations and a minor band centered at ~3365 cm^{-1} associated with non hydrogen bonded free N-H type stretching vibrations. These two values are in good agreement with the published values of ~3290 and ~3383 cm^{-1} respectively [212,213,216,217]. In contrast, the spectrum of leucoemeraldine base contains just the band at ~3383 cm^{-1}, which is characteristic to free, non-hydrogen bonded N-H stretching vibrations [212,213,216,217].

The sequence of spectra taken for emeraldine base powders after heat-treatment at temperatures higher than 250°C demonstrate the disappearance of the hydrogen bonded N-H stretching vibration band centered at ~3285 cm^{-1}, and the persistence of only one peak, at ~3365 cm^{-1}. In addition, the intensity of both quinoid and benzenoid bands is severely reduced, and the peaks broadened. The latter facts, together with the disappearance of the hydrogen bonded N-H stretching vibration, indicate that at temperatures exceeding 250°C, the emeraldine base undergoes a chemical transformation, being reduced to leucoemeraldine base. A similar discovery was reported by Mathew *et al.* [217,219].

Figure 26 shows that the peak centered at 1040 cm^{-1} due to the SO_2 symmetrical stretching vibration (*i.e*. the peak that shows the presence of TSA residue in the emeraldine chains) is severely reduced during the heat treatment until it finally disappears at treatments performed at temperatures exceeding 300°C. The removal of the TSA residue from the polymer chains by heating the polymer at 380°C represents the purpose of heat treatment performed by Ogura *et al.* [177] and is probably the only desirable effect of the high temperature exposure of the polymer.

3.1.4.2. Differential Scanning Calorimetry Characterization

The cross-linking of emeraldine base as a result of heat treatment can be unequivocally demonstrated through a DSC experiment similar to the one performed by Wei *et al.* [187]. The analyzed sample was kept isothermal for 30 minutes at 100°C and then ramped at 20°C/min to 400°C. After cooling down to the room temperature, a second run of the experiment was restarted in the same described conditions. Due to the isothermal held at 100°C, the temperature is displayed on graph starting with 115°C.

The DSC thermogram in Figure 28 shows that the emeraldine powder heated at 400ºC presents an exothermic peak centered at about 225ºC (~250ºC in Wei *et al.* experiment). The DSC thermogram taken right after cooling down the sample to the room temperature displays no exothermic peak, indicating that an irreversible process had taken place during the first run. A thermo gravimetric analysis (TGA) of the emeraldine polymer shows no major loss in the interval 200 to 300ºC, a fact revealed by many authors [150,159-161,164,165,169-171,173,184,187,190,212,213], therefore the thermal process that appears at ~225ºC can be attributed to the crosslinking of the polymer chains

as suggested by Wei *et al.* [197] and also other authors [184,213,215]. Emeraldine base should display a small endothermic peak in the range 200 to 250ºC due to the glass transition that takes place at a temperature in this interval [184,187,213,215], but this endothermic peak is offset by the large exothermic peak due to crosslinking of the polymer chain. With this respect, DSC is not a suitable technique to visualize the glass transition in emeraldine base, but the missing endothermic peak in the DSC spectrum suggests that the glass transition occurs in the vicinity of crosslinking temperature.

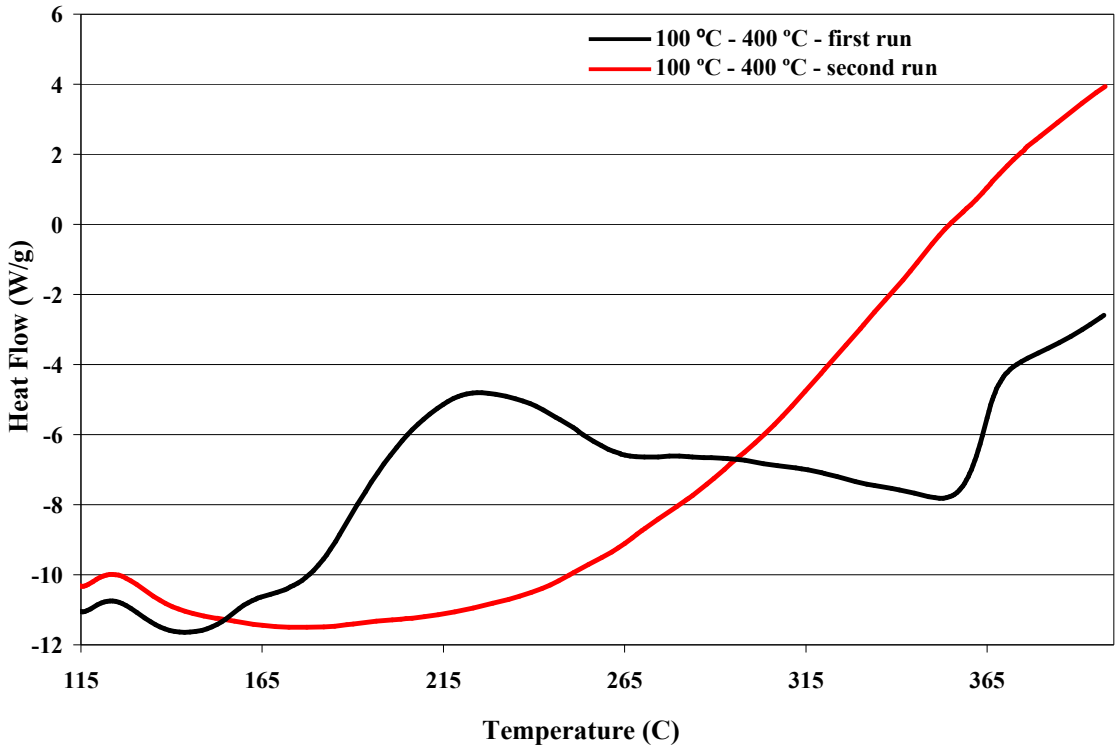

Figure 28. DSC thermogram of emeraldine base held isothermal for 30 minutes at 100ºC and ramped up 20ºC/min to 400ºC.

3.1.4.3. X-Ray Diffraction Characterization

The cross-linking phenomenon occurring at temperatures exceeding 250ºC is also shown in the X-ray diffraction pattern of the powder samples treated at various

temperatures for one hour in helium atmospheres. The peaks are indexed for the emeraldine base class I (EB-I) crystal structure, according to Jozefowicz *et al.* [206]. A comparison of XRD spectra between emeraldine base not heat treated and samples treated at various temperatures is presented in Figure 29. A calculation of the full width at half maxima (FWHM) as well as the ratio of half width over peak height (HW/H) is provided in Table 6. An example of calculating the FWHM and HW/H for an XRD spectrum of a sample heat treated at 100ºC for one hour in helium atmosphere is inserted in appendix (Figure 29a).

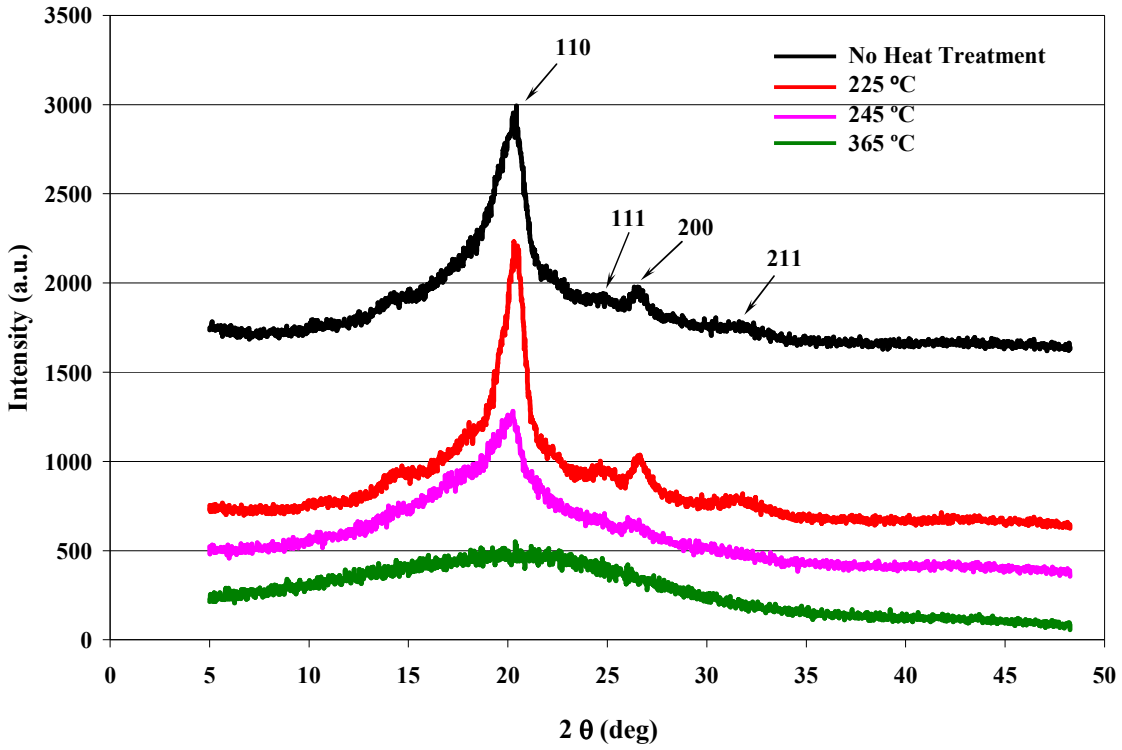

Figure 29. X-ray diffraction of emeraldine base treated at various temperatures.

Table 6. Full width at half maxima and peak half width over peak height for emeraldine base samples heat-treated at various temperatures.

Heat Temperature (ºC)	**FWHM**	**HW/H**
No Heat Treatment	2.3	0.58
100	2.2	0.57
145	2.1	0.5
175	1.9	0.48
205	1.7	0.49
225	1.6	0.47
245	1.8	0.59
275	1.9	0.64
300	2.5	0.68
365	14.1	0.98

If crystallinity is present in polyaniline powder samples, then the main crystalline peak should appear at an angle $2\theta \cong 19.5$ [212,222-224]. The crystalline structure in emeraldine base is not expected if the powder was originally prepared in the conductive salt (emeraldine salt) form and then converted to its corresponding insulating (emeraldine base) form through treatment with a strong base, which was in fact the case of the powder prepared in this work, following Ogura's method (*i.e.* EB-class I). According to Pouget *et al.* [222,223] and Jozefowicz *et al.* [224] crystallinity should be expected just in the case of emeraldine base powders directly synthesized in the base form (*i.e*. EB-class II), or respectively, emeraldine salts directly synthesized in the salt form (*i.e*. ES-class II).

Studying the structure of polypyrrole and the effect of dopant anion on crystallinity of the polymer, Warren *et al.* [225] found that the ratio of the peak half width to peak height (HW/H) of the X-rays diffraction peak reflects order in the polymer backbone. Thus, the smaller the value of the HW/H ratio, the higher the order. Studying the properties of a polyaniline film, Wei *et al.* [187] detected the same relationship between HW/H and order, and found that the value of the ratio HW/H decreased with increasing temperature, reached a minimum and then increased again as the temperature further increased. In their study, the X-Ray diffraction of emeraldine film (which inherently contains ~15% NMP that could not be removed by dynamic pumping) presented the lowest ratio HW/H at ~150°C, which was exactly in the vicinity of glass transition temperature for NMP plasticized emeraldine film. An NMP-free emeraldine base film, however, employed in the same study (prepared by performing a chemical treatment of the film to remove the residual NMP) resulted in a glass transition temperature of ~250°C and a maximum order of the polymer given by lowest HW/H ratio of the X-Ray diffraction peaks corresponding to that temperature.

Considering these, the values obtained in this work are in good agreement with the literature [187] since in this case the glass transition temperature fell in the interval 200 to 250°C, as proved by the DSC experiment. In Wei *et al.* experiment [187] the calculated HW/H ratio of EB film was 0.70 for a sample treated for one hour at 40°C, reached a minimum of 0.49 when treated for 1 hour at 150°C (*i.e.* the glass transition temperature) and then increased with further raise of heat temperature up to a value of 0.91 for a heat treatment of 30 minutes at 280°C.

However, the full width at half maxima (FWHM) is a more exact parameter for analysis of the degree of order in emeraldine base, especially in cases (as in this work) in which the EB-I polymer displays some finite degree of crystallinity. This is because the FWHM criterion does not have to take into account the deconvolution of the overlapping peaks when calculating the base width. The FWHM values displayed in Table 6 are also in agreement with the pattern reported by Wei *et al.* [187], the polymer displaying a maximum order at a temperature of ~225°C, therefore in the vicinity of its glass transition.

3.1.4.4. UV-Visible Spectrophotometry Characterization

UV-Visible spectrophotometry supports the argument introduced by Matthew *et al.* [217,219] regarding the transformation of emeraldine base in leucoemeraldine base during the high temperature treatment. The collected spectra taken for emeraldine base samples treated at various temperatures are presented on the same graph in Figure 30. The displays the two peaks of interest: a peak centered at ~328 nm due to a π-π^* absorption of benzenoid rings and a peak centered at ~630 nm due to exciton absorption of quinoid rings, in good agreement with values reported in the literature [154,166-173,183,217,226-229].

The emeraldine base to leucoemeraldine base transformation after treatment at temperatures exceeding 250ºC is proved by the gradual disappearance of the peak at centered at ~628 nm and the persistence instead of only the peak centered at ~328 nm. The sequence of the spectra show that with an increase in the heat treatment of the emeraldine powder, the polymer slowly transforms into its corresponding

leucoemeraldine base, the latter being shown in the literature as having characteristic just the peak centered at ~328 nm [151,154,212,215,217,227-229].

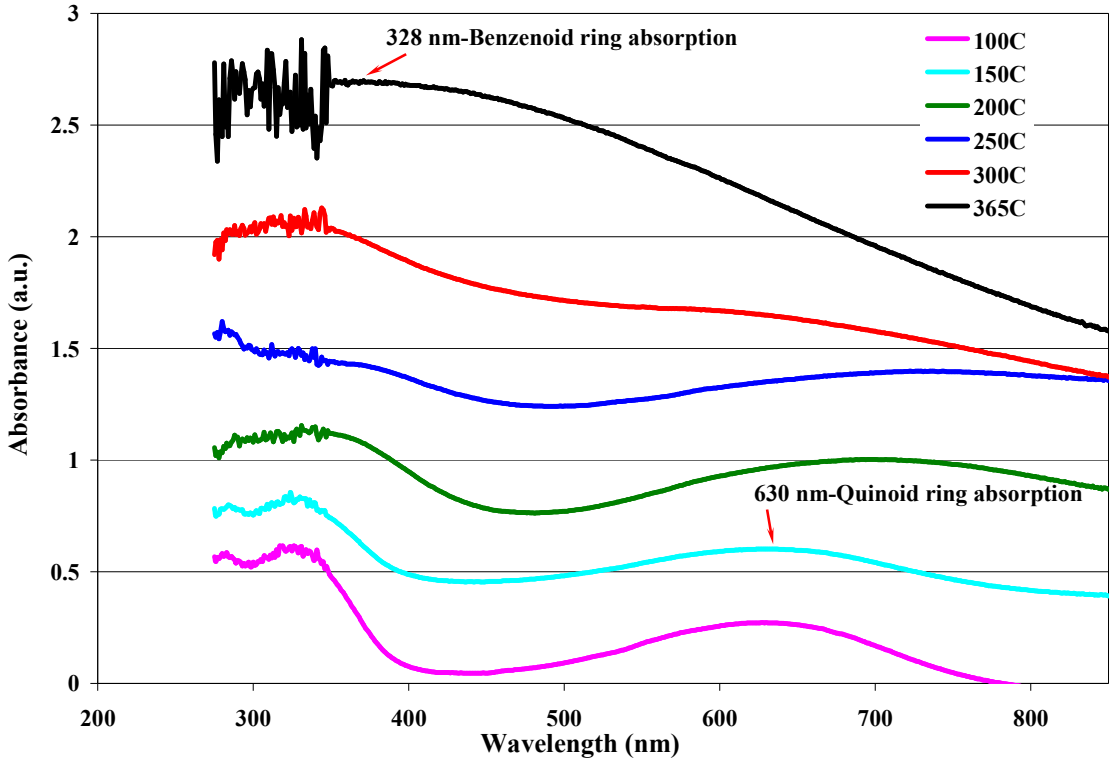

Figure 30. UV-Visible spectrum of emeraldine base samples treated for one hour at various temperatures in helium atmosphere.

3.1.4.5. Materials Characterization Discussion

All the material characterization techniques show that the heat-treatment process (employed by Ogura *et al.* [175-180,197,199] in their development of the emeraldine base CO_2 sensor) represents an unnecessary step. Unfortunately, the removal of the toluene sulfonic acid residue from the polymer chain is more than offset by the other undesirable transformations that concomitantly occur: the partial crosslinking of the polymer and the transformation of part of emeraldine base to leucoemeraldine base. These events might explain why the dynamic range of the sensor is very narrow.

The leucoemeraldine base is processable in NMP but the film deposited cannot be protonated and therefore it does not display an increase in conductivity in the presence of any protonating agent. Moreover, the cross-linked emeraldine base was reported in the literature to be virtually insoluble in NMP, therefore the proportion of true emeraldine base chains in the deposited polymer film is expected to be very low compared to the leucoemeraldine base chains.

The choice of toluene sulphonic acid as a protonating agent for emeraldine base is in fact not a good one. Studying the properties of methyl derivated emeraldine (poly *o*-toluidine), Jozefowicz *et al.* [230] showed that the existence of the CH_3 groups in the emeraldine chain leads to 5% increase in interchain separation and reduced interchain order. This slight increase is responsible for about three orders of magnitude decrease in room temperature conductivity of POT-ES compared to ES-I. X-ray data supports the theory that methyl groups lead to one dimensional electron localization in the poly *o*-toluidine chains, due to higher interchain separation, interchain zigzag and possible disorder generated by randomness in placement of the methyl groups. This random distribution of CH_3 units would further generate disorder in the ring tilt angle and position of the chlorine ions. Compared to POT-ES, the emeraldine salt, ES-I displays three dimensional electron delocalization within crystalline regions. MacDiarmid and Epstein [182] also support the theory of lower conductivity induced by the nature of the protonating agent by showing that bulky groups like dimethyl-sulphate (*i.e.* $(CH_3)_2SO_4$) induce lower Pauli susceptibility and two order of magnitude lower conductivity of the resulting emeraldine salt polymer compared to the emeraldine salt fabricated with HCl as the protonating agent. This difference in behavior is explained by MacDiarmid and

Epstein [182] by the presence of bulky methyl groups which would disrupt symmetry and increase localization of charge due to interchain separation. The authors consider that the charge localization is induced when the dimethyl-sulphate group is not attached to each nitrogen atom in the polymer, making possible in this way an uneven distribution of charge along the polymer chain.

Toluene sulphonic acid ($C_7H_8SO_3$) has an even bulkier functional group, the effect of doping of emeraldine with TSA leading to charge localization and implicitly a lower conductivity in the protonated emeraldine salt. It is therefore not clear why Ogura *et al.* [177] chose this protonating agent in their study. Moreover, the respective group finishes the fabrication procedure by a heat treatment in order to eliminate the residue from the emeraldine base chain. It would have been much easier to employ hydrochloric acid as in the classical method of fabrication proposed by MacDiarmid [160] and followed by most other groups over the years [144,148,149,152,156,158,159,169,181], which would not have necessitated any heat treatment, and therefore any ambiguity in the nature of the resulting material. MacDiarmid and Epstein [182] in fact suggested that hydrochloric acid is the most appropriate agent in polyaniline synthesis, since the residue being volatile, is easily removed under vacuum, unless one tries to study per se the properties of a specific agent-doped polyaniline, like TSA for example.

3.1.5. Possible Explanations for Poor Performance

3.1.5.1. Tautomerism

Tautomerism or hydrogen migration effect was discovered by Shimano and MacDiarmid [227,228] in a study aimed to elucidate the unexpected photoluminescence

properties of some emeraldine base films previously reported by Chen *et al.* [231] and Wan *et al.* [232]. Shimano and MacDiarmid proved that this phenomenon is activated by water absorption in the polymer film during the film casting or solution preparation process. Water absorption in NMP during the film cast and solvent evaporation stages leads to hydrogen migration in emeraldine chains if the relative humidity falls in the interval 43 and 57% or the NMP in which the emeraldine was dissolved previously absorbed between 9 and 18 vol.% H_2O. If at least one of the above conditions was fulfilled, the induced photoluminescence persists in the dry emeraldine film irrespective of the surrounding humidity level [227,228]. The existence of photoluminescence in cast emeraldine base films demonstrates that the films actually contain extended sequences of leucoemeraldine base, since only leucoemeraldine displays photoluminescence [227,228,231,232]. Tautomerism makes therefore the EB chains transform in sequences of EB-LB-PB. Only emeraldine base can be protonated, so the tautomerism leads to the generation of a polymer chains composed of segments than can be made conductive interrupted by segments than can never be made conductive (leucoemeraldine and pernigraniline). A schematic of the process is presented in Figure 31-adapted from reference [227].

Only the absorption of water between 9 and 18 vol.% in NMP could be responsible for tautomerism in this work, since the relative laboratory humidity measured with the humidity sensor was always in the range 34 to 37%, therefore outside the range suggested by Shimano and MacDiarmid [227,228] to be responsible for inducing tautomerism.

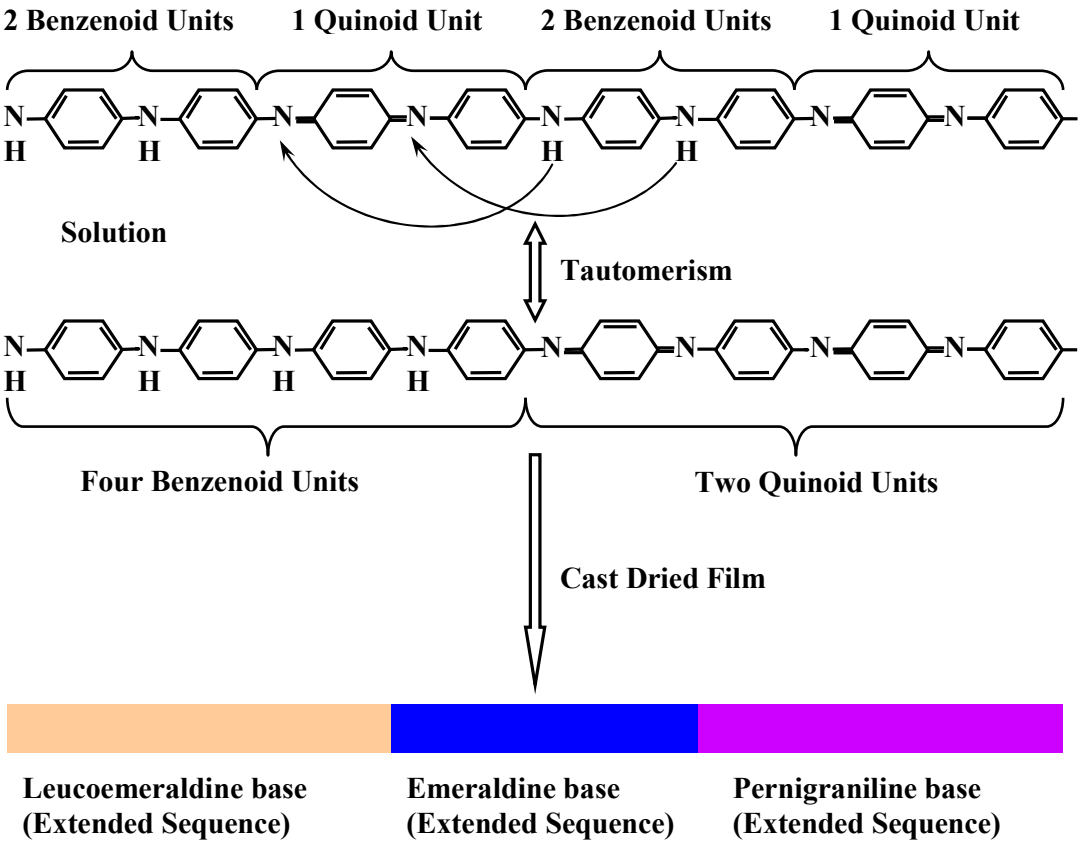

Figure 31. Schematic of the tautomerism process.

3.1.5.2. Limited Protonation in Emeraldine Base

MacDiarmid and co-workers [160-162], followed by Epstein *et al.* [233] and Jozefowicz *et al.* [234] showed that very little or virtually no protonation of emeraldine base occurs if the pH of the protonating bath is greater than 4. A supporting argument is presented in Figure 32-adapted from references [160,161], with the original experimental points collected by respective authors displayed on graph. The use of DataThief software helped generating the graph line close to the originally published line. The graph shows that emeraldine base is not protonated until the pH of the doping hydrochloric solution reaches the value of 4. The sample is in fact not significantly protonated even at a pH of

2, whereas a maximum protonation level is reached when the pH of the bath approaches zero. Reiss [235,236] considered that the method of calculating the doping percentage followed by authors in references [160] and [161] (*i.e.* chlorine uptake) was not free of experimental errors, either from a failure to reach the full equilibrium in the protonating bath, or from shifting of that equilibrium during the drying process of the sample. It is therefore reasonably to consider that higher errors occur at high pH values, where the chlorine uptake is smallest.

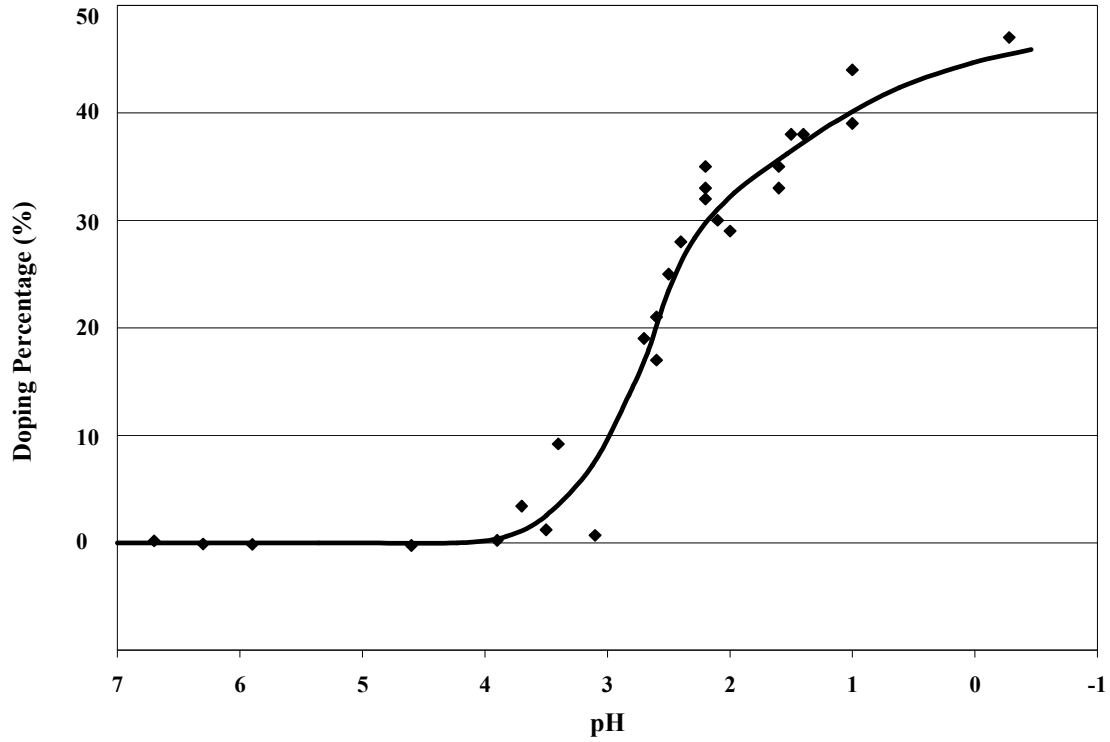

Figure 32. Doping percentage as a function of pH of protonating solution for the class I of emeraldine base.

To calculate the expected pH of a solution in which 100% carbon dioxide was bubbled, the series of equations (3) to (7) were used. Therefore,

$$K_1 = \frac{[H^+]\times[HCO_3^-]}{[CO_2(aq)]} = 4.47 \times 10^{-7}\ \text{M/atm} \qquad (7)$$

but the proton and bicarbonate concentrations are equal in carbonic acid solution more concentrated than 10^{-5} M [37] (*i.e.* p_{CO2} above 355 ppm), given:

$$K_1 = \frac{[H^+]^2}{[CO_2(aq)]} \tag{29}$$

Therefore in the above equation, $[CO_2(aq)]$ is the only unknown value for the pH calculation. To solve for this, the above equation (2) is employed:

$$CO_2(aq) = p_{CO2} \times K_H \tag{2}$$

where $K_H = 30 \times 10^{-3}$ M/atm is Henry's constant.

Finally, $[H^+]^2 = (K_1 \times K_H \times p_{CO2})$ and pH = - log $([H^+])$

For water in equilibrium with 100% rich CO_2 atmosphere (*i.e.* $p_{CO2} = 1$), plugging the values of K_1 and K_H in the above equation gives the pH = 3.936. At this pH level induced by bubbling 100% carbon dioxide in water, following the graph published by MacDiarmid [160,161] and reproduced in Figure 32, EB is virtually not protonated and therefore does not display any perceptible increase in conductivity.

3.1.5.3. Limited Amount of Water in PVA Matrix

Other possible explanation for such large discrepancies between the results in this work and Ogura *et al.* may be due to the amount of water incorporated by poly(vinyl alcohol). A graph showing the amount of water absorbed measured by mass gain is presented in Figure 33.

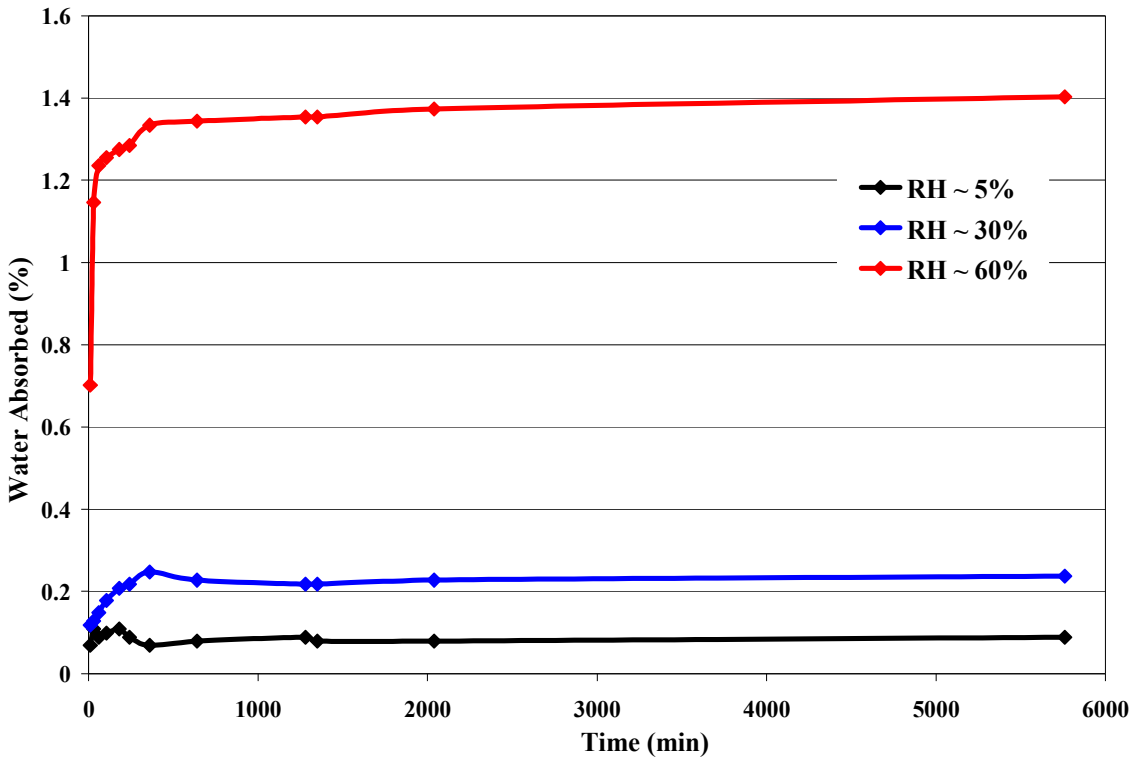

Figure 33. Percent water absorbed in poly (vinyl alcohol)-NMP plasticized film, at various humidity levels.

The amount of water absorbed by PVA polymer in powder form was reported to be as high as 20% by weight at 80% relative humidity [237]. However, the plasticized PVA films were reported to absorb less amount of water than PVA powder. Studying the water uptake in plasticized PVA and cellophane films, Creutz and Wilson [238] showed that a relative humidity of 57.5% is responsible for 5.1 % by weight water uptake in PVA films. Therefore, the water uptake level measured thermogravimetrically in this work is a factor of 3.5 smaller than the value reported by Creutz and Wilson [238]. The limited quantity of water inside the composite polymer (emeraldine base-PVA) chains may explain the poor performance of the composite polymer employed for carbon dioxide detection,

though the amount of water necessary for the carbon dioxide hydrolysis reactions is arguable.

3.2. Immersed Sensor

3.2.1. Experimental Results

Due to the deleterious effect of the presence of TSA residue within the polymer (*e.g.* see the above described electron localization leading to a lower potential conductivity) as well as the undesired transformations induced in emeraldine by the thermal process to remove the sulphonate residues, the use of TSA-doped emeraldine was discontinued and emeraldine hydrochloride was employed instead for the rest of the project.

The study revealing the limited amount of water absorbed in the PVA matrix generated the idea to immerse the sensor in water. In this arrangement, carbon dioxide was bubbled through the water. Since water became in this experimental set-up abundantly provided to the emeraldine base polymer chains, the presence of PVA matrix as a water pool was not necessary any more. Therefore, an emeraldine base in NMP film alone was deposited on a 15 micrometers spaced interdigitated electrode.

A graph showing the two impedance spectra, corresponding to a measurement in pure water of pH = 6 and carbonic acid solution of pH = 4.4 is displayed in Figure 34. During the impedance measurements in this configuration, the pH of the aqueous solutions in which the sensor was inserted was continuously monitored with a pH meter with no buffer employed to fix the pH.

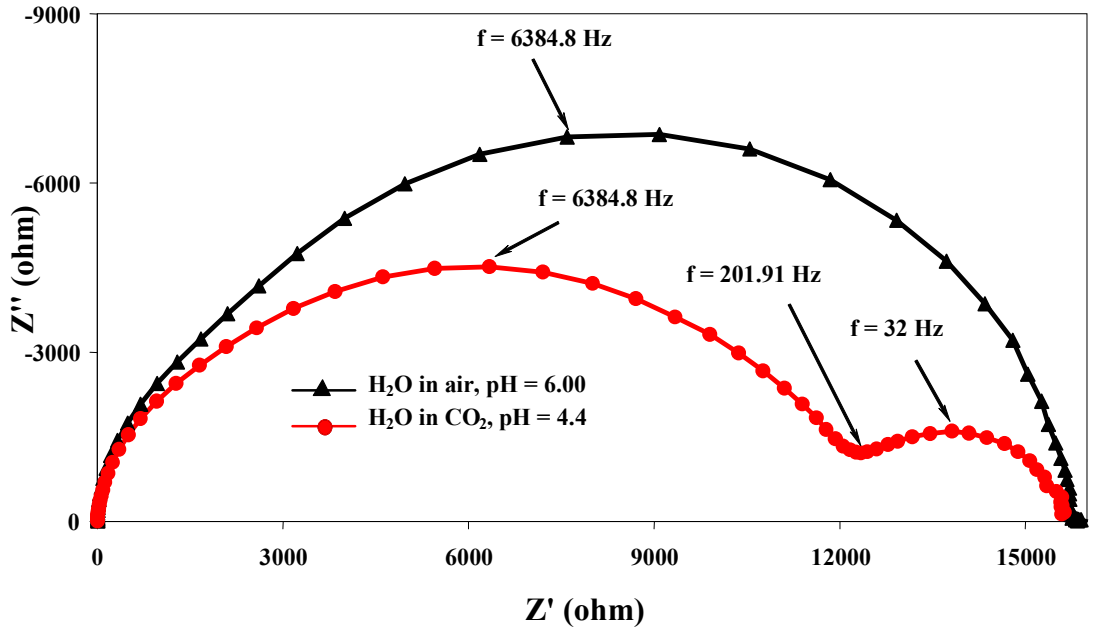

Figure 34. Impedance spectra in pure water and water where pure CO_2 was bubbled.

The above graph reveals that a change of medium from pure water of measured pH ≅ 6.00 to carbonic acid solution of measured pH ≅ 4.40, does not cause any change in total resistance of the thin emeraldine film since the two measurements present the same intercept on the horizontal axis [209]. A conductivity measurement performed with a DC technique would have measured only the total resistance. Impedance spectroscopy on the other hand is a powerful technique because it allows one to separate contributions from different conduction processes and determine the frequency interval over which each of them is dominant.

A spectrum collected in pure water shows only one mechanism active, with a characteristic peak frequency of 6385 Hz. When carbon dioxide is bubbled and subsequently carbonic acid dissociates producing protons and carbonium ions, the pH drops to ≅ 4.40 and the emeraldine film senses this new medium. Apart from the original

mechanism, which is still present, and display the same peak frequency of 6385 Hz, an additional mechanism having a characteristic peak frequency of 32 Hz becomes active at a frequency of 202 Hz.

In the following part of the project, attempts are made to characterize and interpret this behavior not yet reported in the literature.

3.2.1.1. Conductivity Response in Hydrochloric Acid Solutions

Figure 35 shows the resistance response of emeraldine base thin film sensor, in hydrochloric acid of various pHs. For each specific pH level the resistance displayed on graph represents the value provided by the equivalent circuit fit.

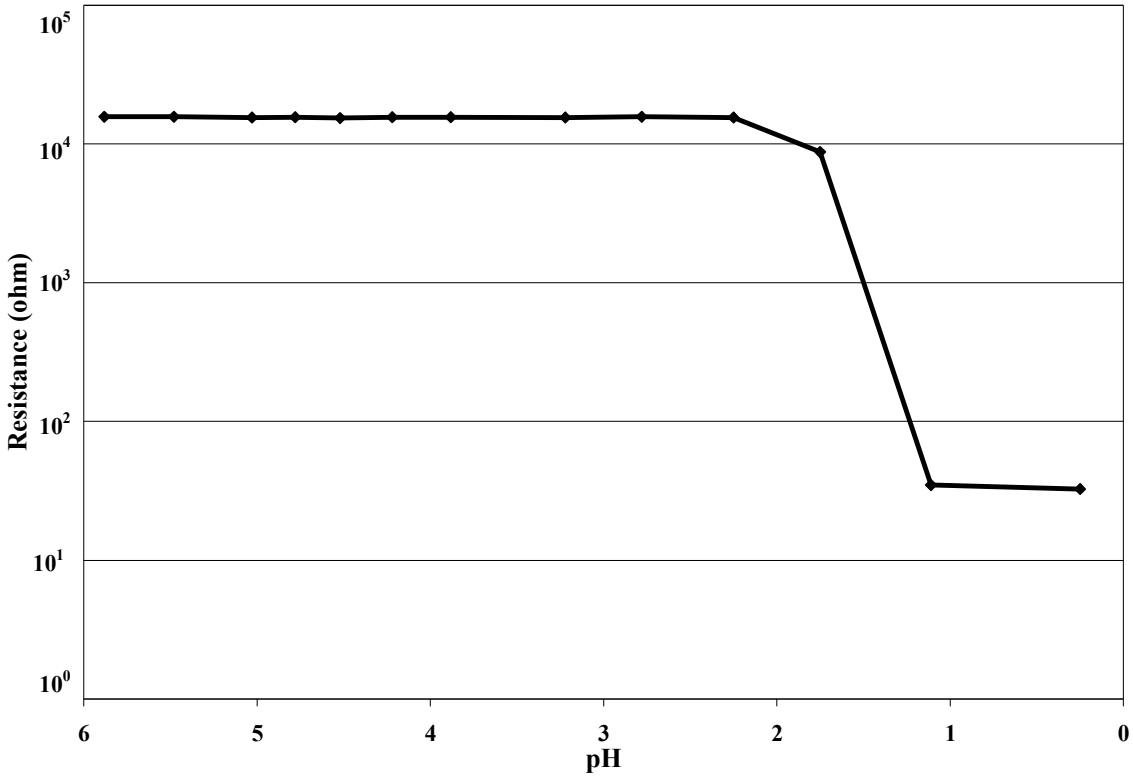

Figure 35. Total resistance of emeraldine base thin film vs. pH in aqueous HCl solutions.

A comparison between the conductivity response of the film calculated with equation (28) as a function of pH and the one published by MacDiarmid (*i.e.* adapted from the original reference, with the original data points preserved by DataThief software) is presented in Figure 36. However, the two polymers employed belonged to different classes and therefore caution should be followed when their properties are compared. MacDiarmid's polymer [161] in the form of compressed pellet was in the EB-I class, whereas the thin film cast from NMP utilized in the current project belonged to the EB-II class. Jozefowicz *et al.* [234] showed that for the emeraldine base in the class II, the onset of conductivity is even more difficult to accomplish and occurs at lower pHs. A comparison of the two responses reported by MacDiarmid *et al.* [161] and Jozefowicz *et al.* [234] is presented on the same graph in Figure 37.

Jozefowicz *et al.* [234] published just the "percent doping vs. pH" graph but also considered that the protonation first occurs in the amorphous part of the EB-II crystal structure, at pHs below 4, (*i.e*. a fact already suggested by MacDiarmid and Epstein [182] and supported by the already published X-ray data [206,222]). Moreover, Jozefowicz *et al.* [234] showed that the crystalline part of the EB-II transforms to the respective ES-II crystal structure only at pHs equal to or lower than 2.3, or respectively when the doping level in the polymer reaches 25%, in accordance to an early finding of MacDiarmid *et al*. [182].

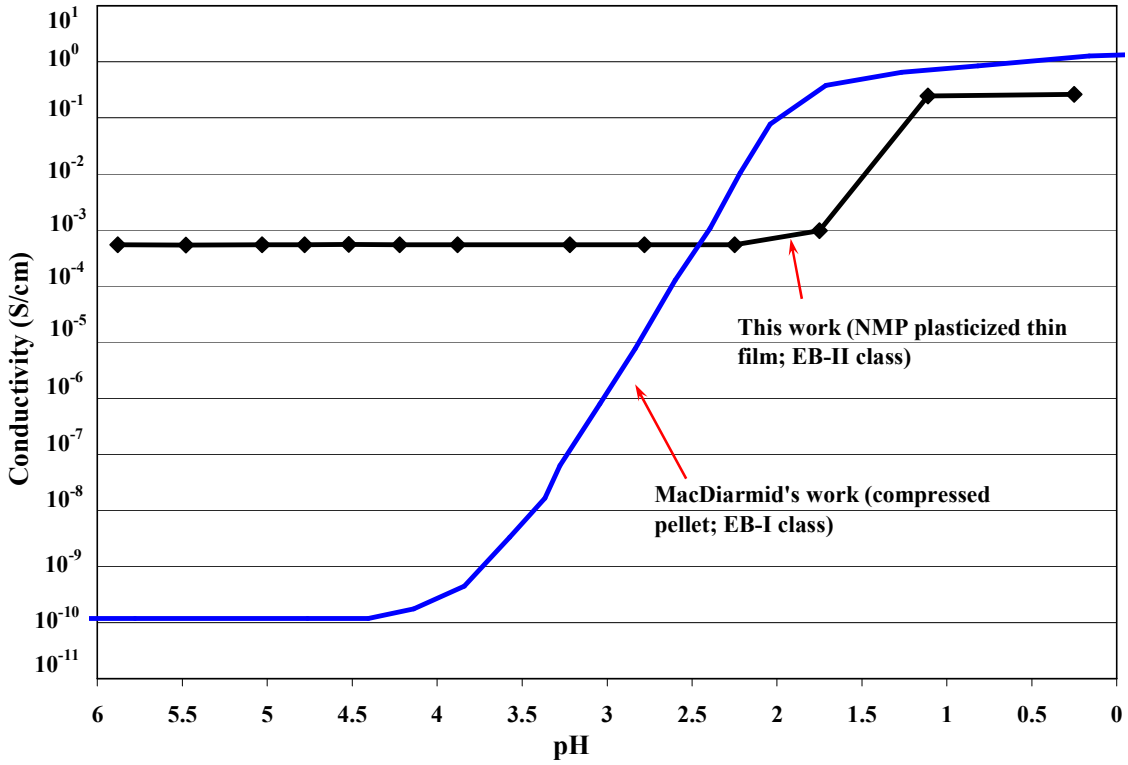

Figure 36. Comparison of the conductivity responses as a function of pH for the two classes of emeraldine base: the EB-I reported by MacDiarmid [161] and the EB-II employed in the current project.

Therefore, it is not surprising that Figure 36 shows that the emeraldine base thin film employed in the current project displayed an increase in conductivity at a pH level lower than the one published by MacDiarmid *et al.* [161]. The second semicircle (*i.e.* already mentioned in discussing Figure 34) starts forming at a pH level of HCl in water of 5.03 for the sensor employed in these measurements and grows as the pH level of the protonating solution is progressively lowered.

The appearance of the second semicircle is displayed in Figure 38. A zoom into the low frequency area is displayed in Figure 39, showing that the low frequency random noise align into a horizontal line at pH = 5.03, which gradually transforms into a semicircle as the pH level is further decreased.

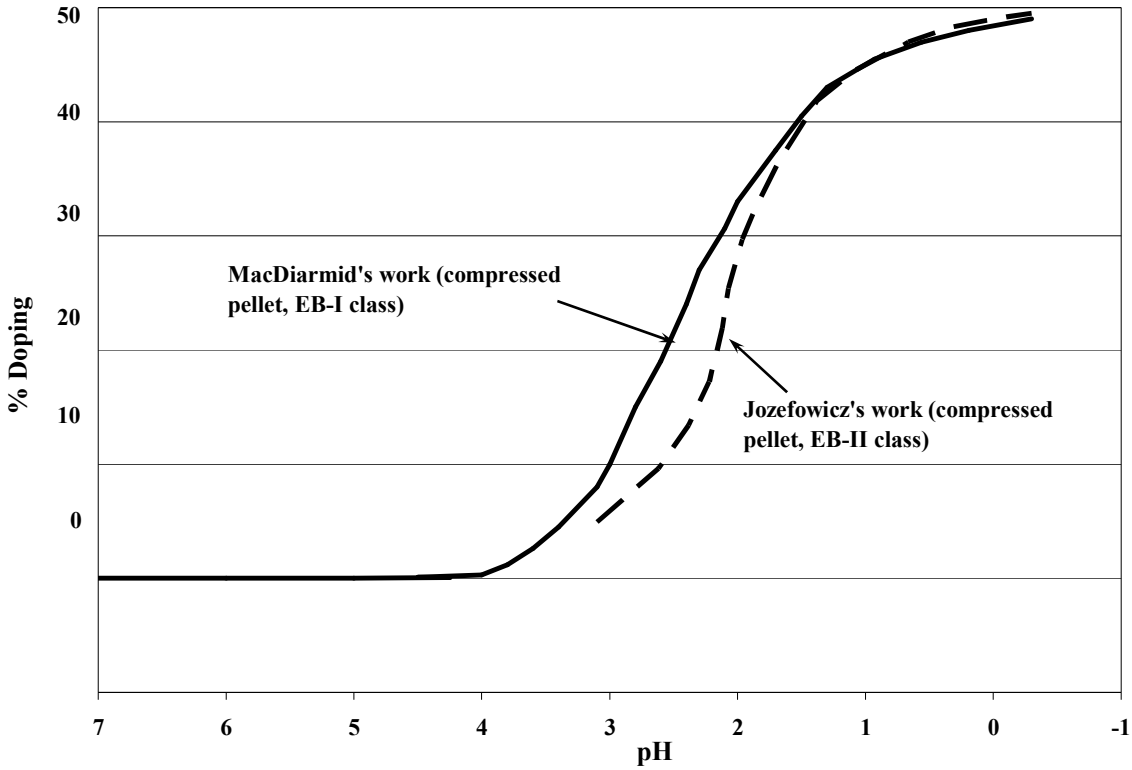

Figure 37. Comparison of the doping percentage vs. pH responses for the two classes of emeraldine base reported in the literature: MacDiarmid [161] and Jozefowicz [234]; The data points shown on the graph belong to MacDiarmid, being reproduced by DataThief software close to the one originally published.

In all this time, the total resistance of the sensor given by its intercept with the horizontal axis remains unchanged until the pH of the protonating bath reaches 2.25. A measurement of the resistance performed with a DC multimeter would indicate that the onset of conductivity increase does not occur until the pH of the solution reaches 2.25, since the sensor would have displayed the same total resistance over entire pH range employed. In fact, MacDiarmid *et al.* [160-162], Epstein and MacDiarmid [233] and Jozefowicz *et al.* [234], all measured the conductivity by the four-probe technique, which is a direct-current method of measurement.

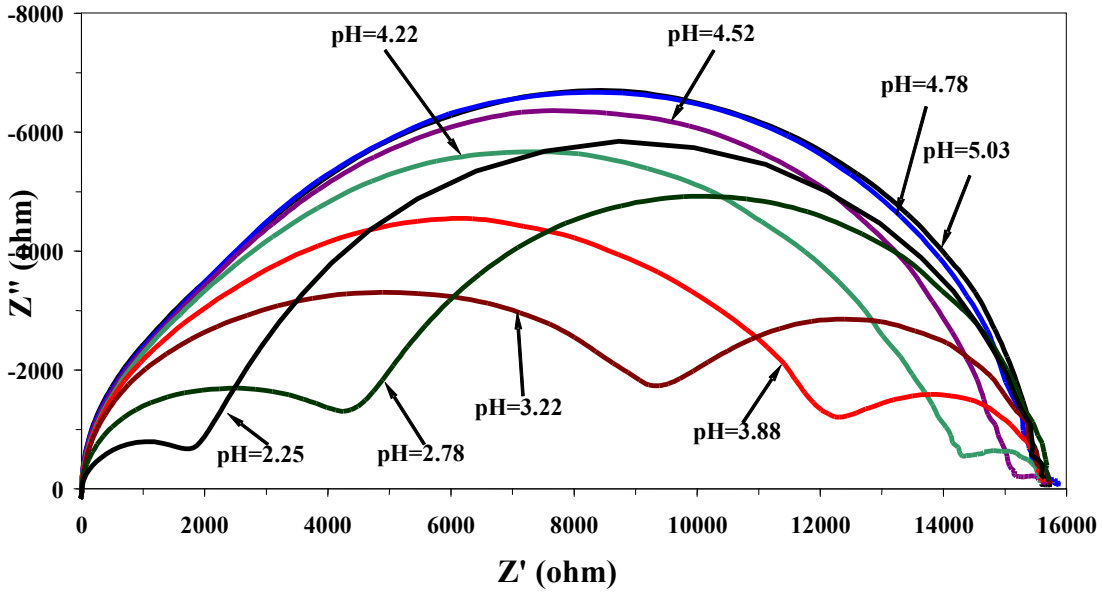

Figure 38. The formation and evolution of the second semicircle with variation of pH level.

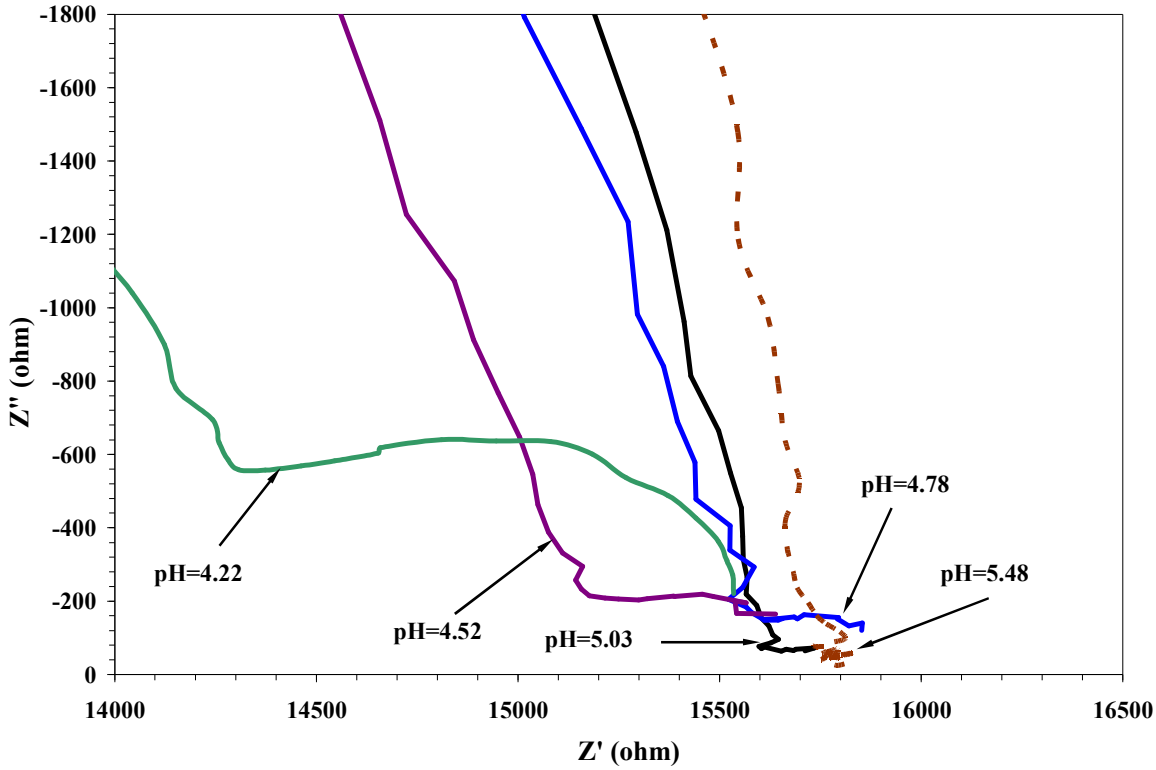

Figure 39. Appearance of the second semicircle as a horizontal line at pH=5.03 and its subsequent evolution with decreasing pH level.

The onset of increase in conductivity (decrease in resistance) of the emeraldine film at pH = 2.25 is displayed in Figure 40. At a pH level greater than 2.25, the total resistance of the film was essentially constant. Once the pH of the protonating bath reached 2.25, the resistance of the film started to decrease slowly. The slope in each pH domain is different, meaning that the protonation became accelerated as the pH progressively dropped, a fact expected since the amount of protons was increased by lowering the pH.

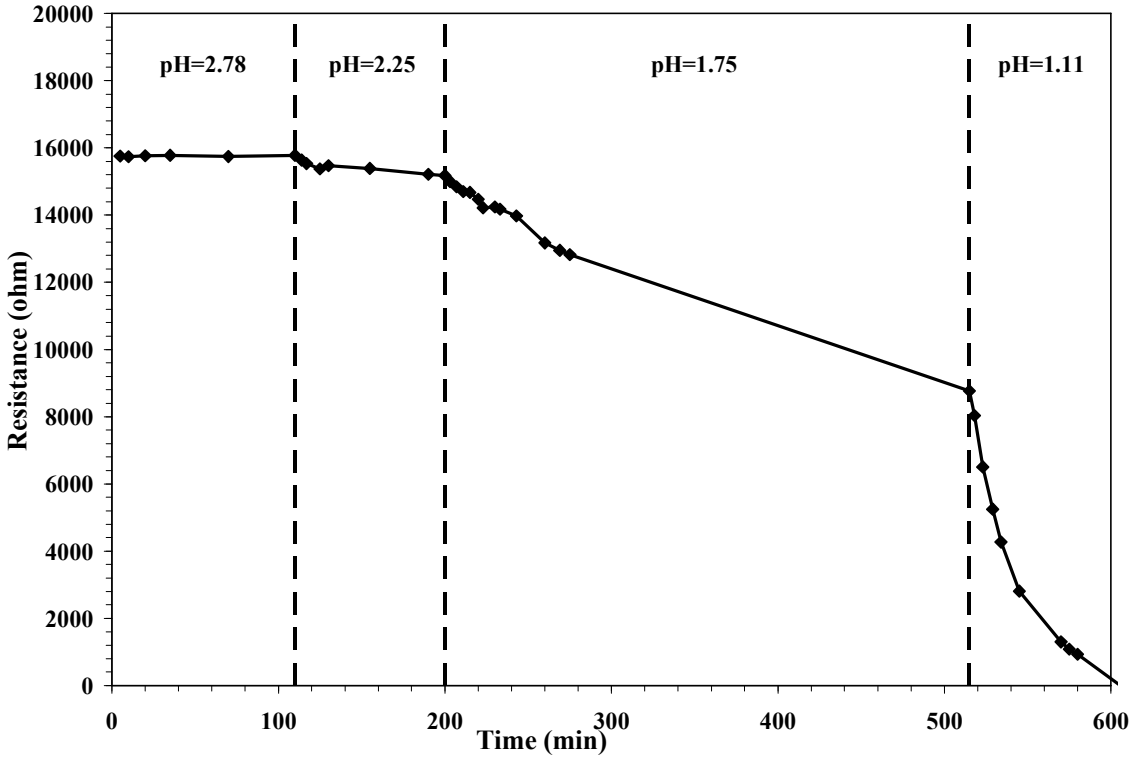

Figure 40. Resistance variation of the NMP-plasticized emeraldine base thin film with time at different pH levels, showing the onset of conductivity change at pH = 2.25.

A graph showing both pH and the resistance of the first semicircle as a function of hydrochloric acid concentration of protonating bath is presented in Figure 41. A correlation between the measurements performed with two different techniques (resistance measurements with interdigitated electrode and pH measurements with pH meter) is observed. The fact that the resistance response of the emeraldine film follows the titration curve of hydrochloric acid is an indication of the pH response of the polymer that extends beyond the pH level of 4.

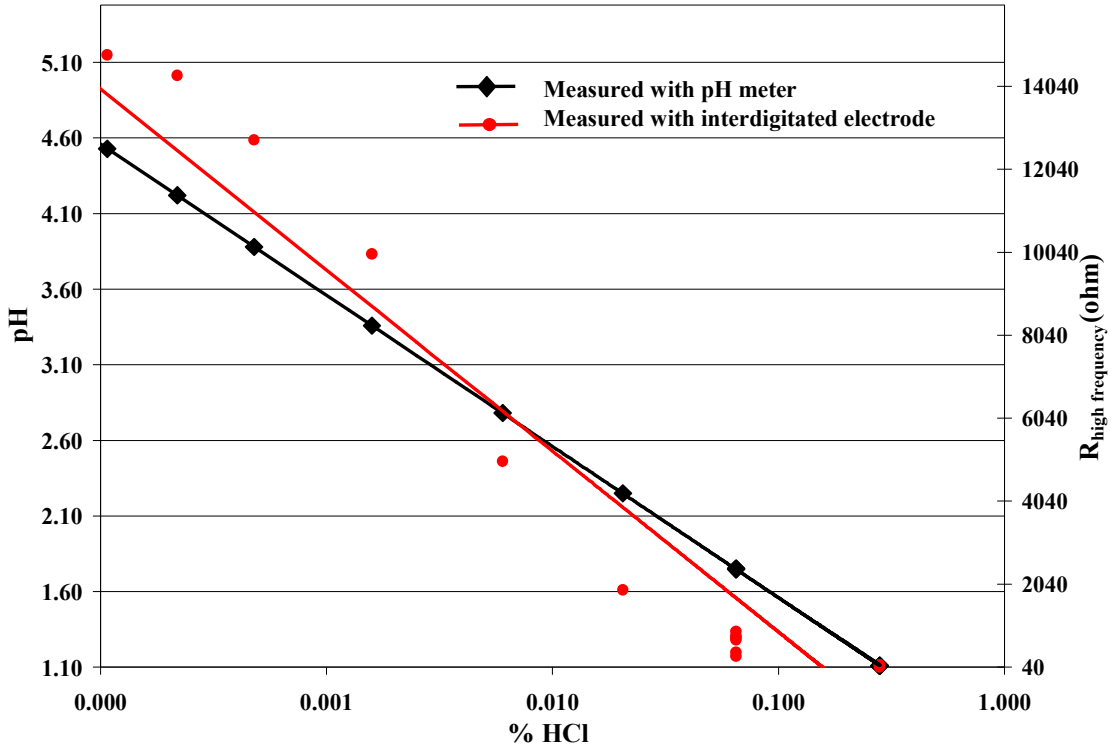

Figure 41. Titration curve of hydrochloric acid in water and resistance response ($R_{high\ frequency}$) of the emeraldine film as a function of hydrochloric acid concentration.

A plot of the capacitance values of the two semicircles given by the equivalent circuit fit, as a function of pH is displayed in Figure 42. It is interesting to note that the response can be separated in time dependent and time independent domains and the

border between the two is the pH of 2.25, the pH at which the onset in conductivity increase occurs. The conduction mechanism which forms the initial semicircle (that starts diminishing in magnitude as the pH is lowered below the value of 5) has associated with it a virtually constant capacitance in the pH interval in which the overall conductivity of the film is unchanged (*i.e.* pH between 2.25 and 5). The semicircle that starts forming at a pH lower than 5 displays a progressively lower capacitance in this pH interval. When the onset of conductivity change establishes, the capacitances associated with both mechanisms increase with time of exposure in the respective pH.

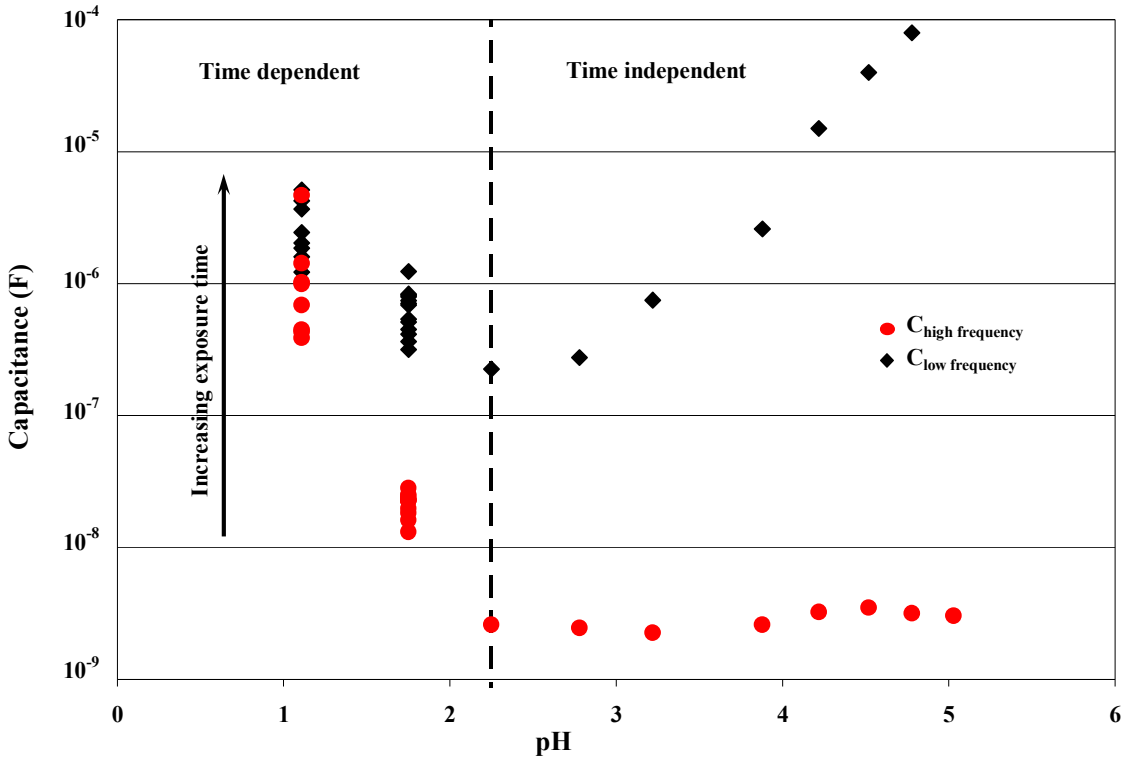

Figure 42. Capacitance as a function of pH associated with the sensor response in hydrochloric acid.

Graphs showing the behavior of capacitances as a function of time spent in pH = 1.75 and pH = 1.11 displayed in Figure 43 and Figure 44 show parabolic dependence of the capacitance as a function of square root of time, suggesting a diffusion controlled process in these pH ranges.

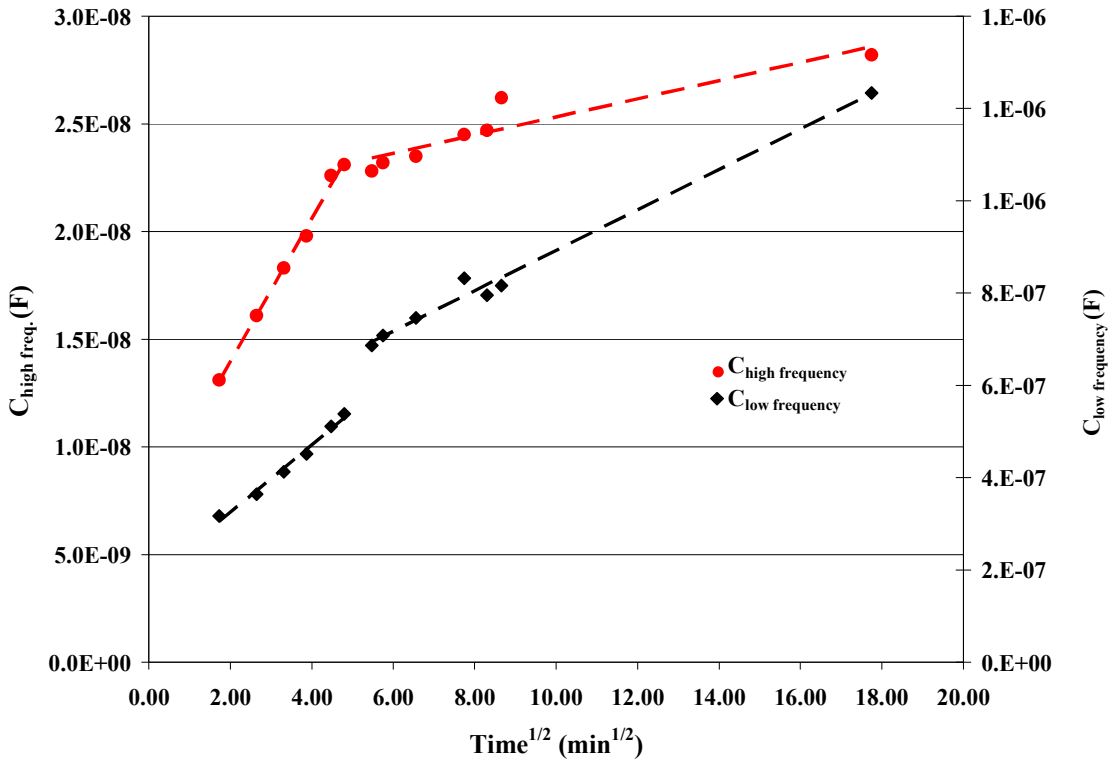

Figure 43. Capacitance vs. square root of time for the emeraldine base thin film equilibrated for various times in pH = 1.75

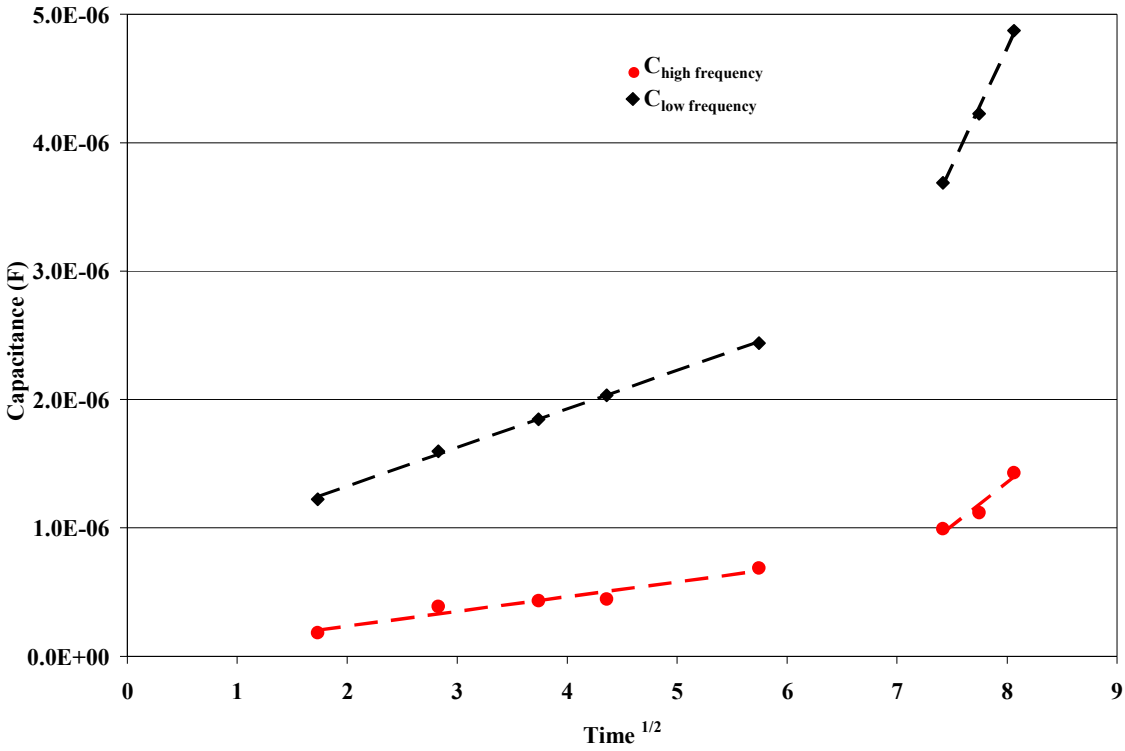

Figure 44: Capacitance vs. square root of time for the emeraldine base thin film equilibrated for various times in pH = 1.11

The time constant (slope of the lines) differs in the two pHs, indicating that the diffusion process (of chlorine ions) is pH dependent, as expected. Figure 43a in appendix display the time dependence of capacitances of the two conduction mechanisms in pH levels of 1.75 and 1.11 on the same graph. Figure 43 and Figure 44 show that even in the same pH level the time constant changes, suggestive to the fact that the achievement of equilibrium protonation in each pH is dependent on diffusion of counter ions near the charged portions of the emeraldine chain to maintain chain neutrality.

Impedance spectroscopy, due to the size and cost of equipment, is not amenable for use in a practical sensor. However, the impedance measurement at a fixed frequency would only require a simple oscillating circuit, which may be feasible for some

applications. The impedance of emeraldine base film at a specific frequency is defined [209] as:

$$|Z| = \sqrt{Z'^2 + Z''^2} \tag{30}$$

The impedance of two-different emeraldine base films measured at two different fixed frequencies (1 Hz and 3.2 kHz) in different pHs in hydrochloric acid is displayed in Figure 45.

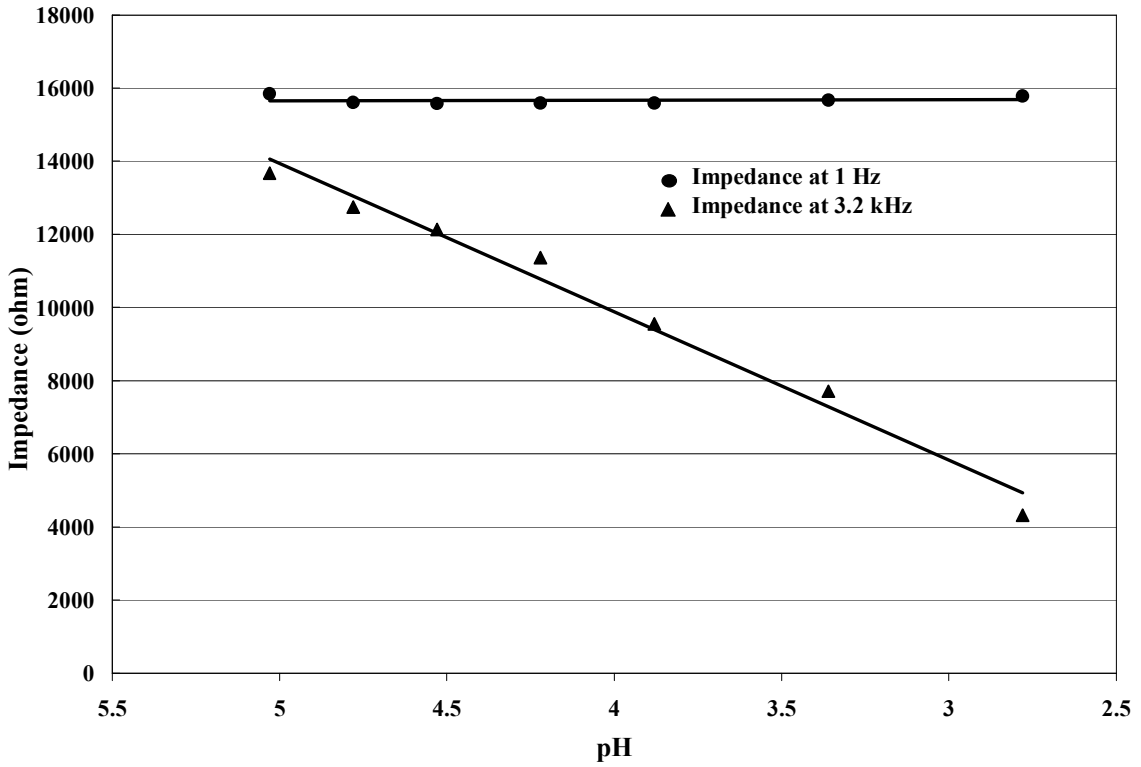

Figure 45. Impedance as a function of pH of hydrochloric acid solution for two fixed frequencies.

A graph showing the conductivity response of another emeraldine base thin film prepared from the same stock solution is inserted in appendix as Figure 43b. The later sensor having characteristic a conductivity of 4.78×10^{-3} S/cm (*i.e.* calculated with

equation (28)) right after equilibration in pure deionized water, displayed the onset of increase in conductivity at a pH of hydrochloric acid of 2.75, and started displaying the second semicircle at a higher pH (*i.e.* 5.85) than the sensor previously described. An explanation of this discrepancy could rest in local arrangements difference, (*i.e.* finely distributed, less scattered metallic islands in the insulating matrix, according to the morphological model of emeraldine base described before).

3.2.1.2. Conductivity Response in Carbonic Acid Solutions

The conductivity response of the sensor with time and pH level in various measurement conditions is presented in Figure 46 through Figure 48. Fitting the measured data is an ambiguous step since there is sometimes more than a single equivalent circuit that can fit the experimental data [209]. From the multitude of equivalent circuits tested, the sequence of R-C described in Figure 16 and Figure 18 depicted the measured data on both criteria of best visual fit and low fitting error. Figure 46 displays the sensor resistance variation as a function of time in the various testing conditions depicted on graph. The bubbling of 100% carbon dioxide in pure water lowers the pH to a level of 3.95-4.0.

The removal of the aqueous carbon dioxide can be accomplished by bubbling an inert gas through the solution, leading to an increase in pH displayed by carbonic acid solution with time. The argon gas coming from a tank displaying by manufacturer a purity of 99.9% lowered the pH of pure water to 4.65, indicating that some form of acidic impurity was present. The purification of the gas in this particular cylinder was accomplished by passing the gas through a 1 molar aqueous NaOH solution, an event that

led to the expected increase in the pH of aqueous solution. These two cycles are displayed on Figure 48 as "Ar-unpurified" and "Ar-purified" respectively.

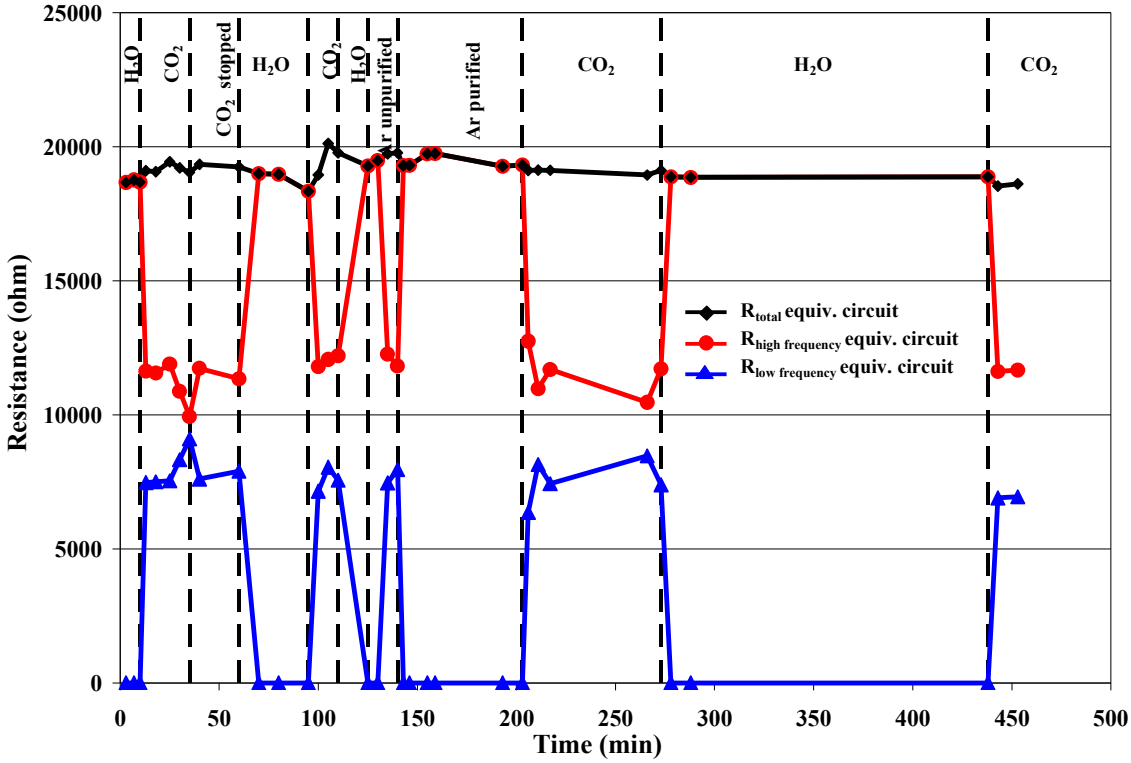

Figure 46. Sensor resistance in alternating cycles involving alternating bubbling of CO_2, purified and unpurified Ar through water. Graph labels: "H_2O"- pure water exposed to room atmosphere air, "CO_2", "Ar purified" and "Ar-unpurified"- bubbling of respective gas in pure water. The equivalent circuit model gives the data points on graph.

The bubbling of unpurified argon gas had the same effect of bubbling carbon dioxide, *i.e.* lowering the pH of solution and increase in the resistance of the low frequency semicircle, suggestive to the fact that the sensor does not detect carbon dioxide but is actually a pH based sensor.

On the graph in Figure 47 are displayed the resistances of the two semicircles obtained as a geometrical intercept with horizontal axis, as well as the total resistance obtained by adding these two values. At any pH greater than 5 the impedance spectra consist of a single semicircle, therefore the total resistances given by means of

geometrical and equivalent circuit considerations are equal. Moreover, the low frequency resistance is zero and high frequency resistance equals the total resistance. At pH values lower than 5, the total resistance given by the geometrical intercept is greater than the total resistance given by the equivalent circuit, due in fact to overlapping of the two semicircles. However the difference between $R_{low\ frequency}$ and $R_{high\ frequency}$ set of values obtained in equivalent circuit and geometrical considerations is systematic.

Figure 48 depicts the response of the sensor in the above mentioned conditions as a function of pH of aqueous solution. In addition, Figure 48 shows that the difference between the high and the low frequency semicircles is greater when the pH of the solution employed is higher. When the pH of the solution progressively decreases, the low frequency semicircle increases on the expense of the high frequency semicircle and the difference in resistance between the two diminishes.

The response time of the sensor to changes in pH level could not be accurately determined by impedance spectroscopy measurements since an impedance measurement takes about 3 minutes to complete, for a frequency sweep between 3.2×10^7 and 1 Hz.

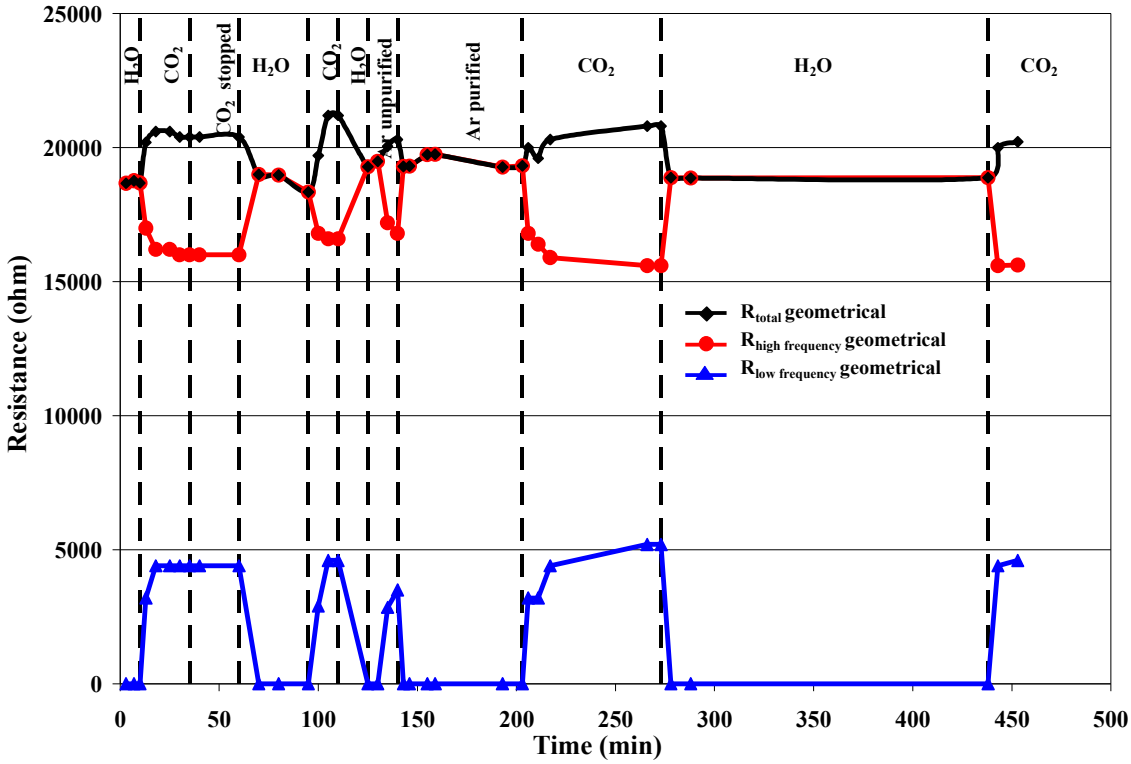

Figure 47. Sensor resistance in alternating cycles involving alternating bubbling of CO_2, purified and unpurified Ar through water. Graph labels: "H_2O"- pure water exposed to room atmosphere air, "CO_2", "Ar purified" and "Ar-unpurified"- bubbling of respective gas in pure water. The geometrical intercept gives the data points on graph.

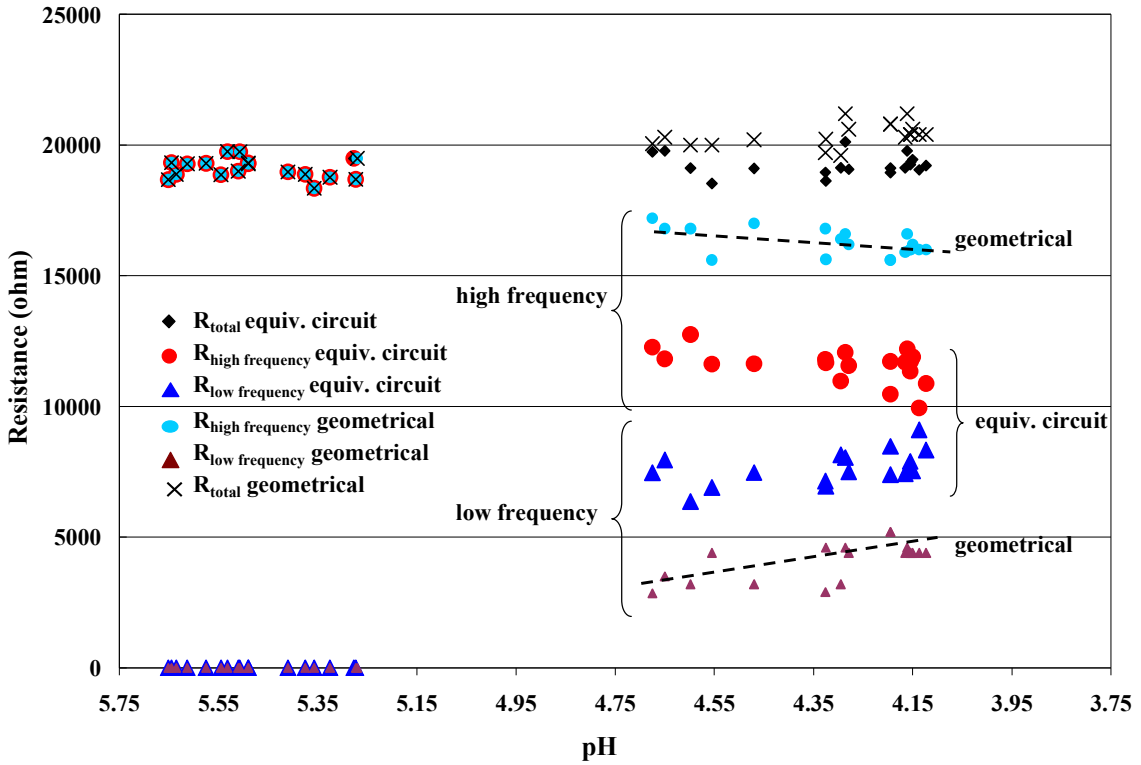

Figure 48. Sensor resistance as a function of pH, in alternating cycles involving alternating bubbling of CO_2, purified and unpurified Ar through water.

3.2.2. Complexation Effect Study

The carbon dioxide detection mechanism is not based on the overall conductivity change of the film. This is expected since the emeraldine base cannot be protonated at pHs greater than 4. Nevertheless, even if no protonation of imine sites is expected from carbonic acid, the carbonium ion (HCO_3^-) being a complexation agent could induce complexation to the imine sites. In fact, any protonation or complexation of the chain would produce the following events [213,215]:

1) an increase in the relative intensity of the peak centered at 1165 cm^{-1} (*i.e.* due to the N=Q=N stretching mode) with respect to the peak centered at 1503 cm^{-1} (*i.e.* attributed to C=C stretching mode in benzenoid ring);

2) a progressive shift of the 1165 cm^{-1} peak to lower wavelength;
3) an increase in intensity of the ~1308 cm^{-1} peak (*i.e.* attributed to C-N type stretching vibration).

Regarding the N=Q=N stretching mode, the fully protonated emeraldine salt has this peak centered at 1144 cm^{-1} but intermediate levels of protonation display this peak at intermediate wavelength between 1165 and 1144 cm^{-1}, whereas the unprotonated emeraldine base displays this peak centered at ~1165 cm^{-1}

The characteristic FTIR spectra of the dried film is presented below in Figure 49. The peak assignment displayed on graph is in excellent agreement with values reported by Chen *et al.* [215] for emeraldine base films. Figure 50 presents the comparison of the FTIR spectra between the dried film equilibrated in water and the same film immersed for 10 minutes in H_2CO_3 solution of pH = 3.95.

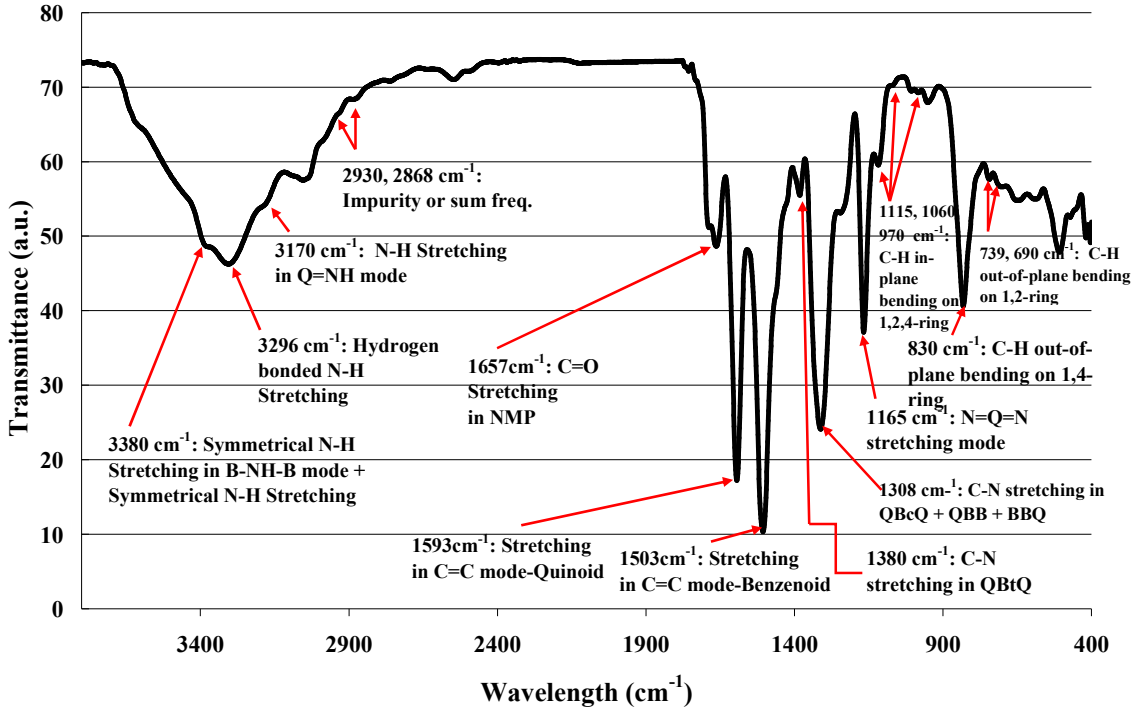

Figure 49. FTIR spectrum of the dried emeraldine base thin film.

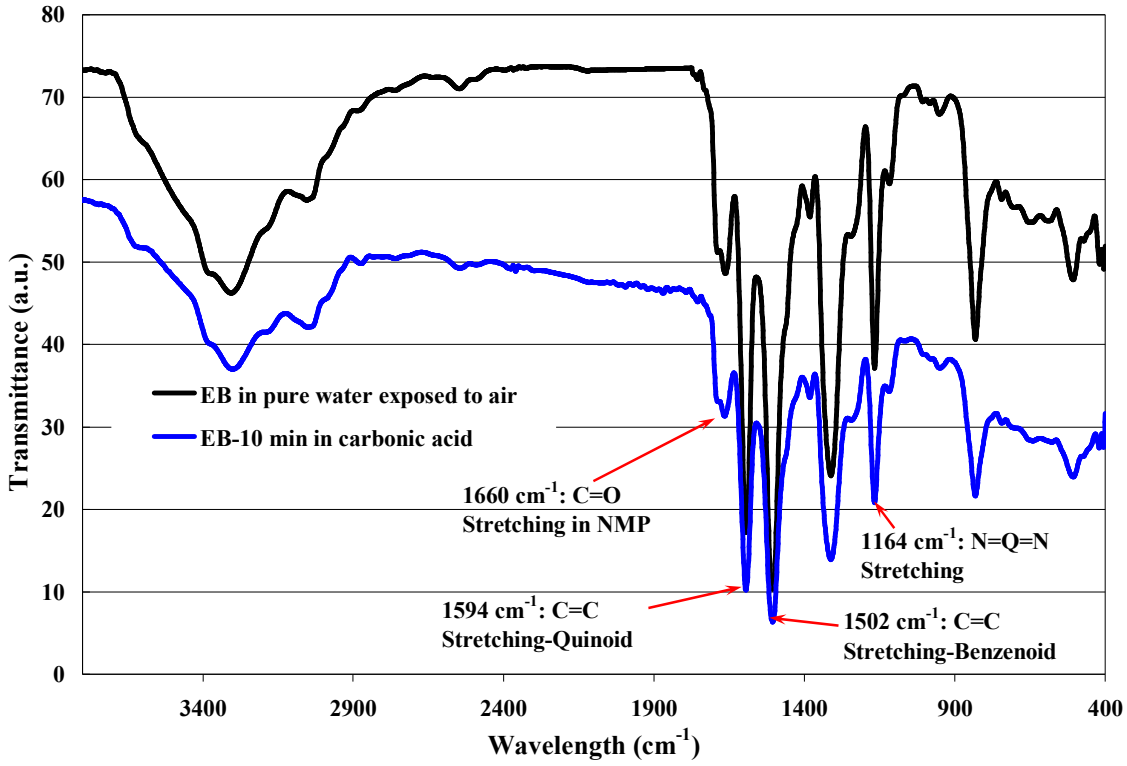

Figure 50. Comparison of the FTIR spectra between the dried film and the film immersed for 10 minutes in carbonic acid solution of pH = 3.95.

None of the above-described effects was observed in this work; therefore, no protonation or complexation of the imine sites could be detected by FTIR and attributed to the exposure of emeraldine base film to carbonic acid. Thus, the FTIR complements the impedance measurements, showing that no protonation and/or complexation of the emeraldine chain is possible with carbonic acid.

However, Chen *et al*. [215] observed that protonation in emeraldine base thin films is more difficult to accomplish than in the respective powder pellets, due to the plasticizing effect of NMP residue. In the next development it is necessary to assess whether the lack of protonation and/or complexation of imine sites is due to the inherent NMP content in the film (*i.e.* the residual NMP is expected to be somewhere between 10

and 18 %, according to numerous reports in the literature [145,160-162,167,212,215, 216]). Therefore an acid base treatment was performed on emeraldine base film in order to remove the residual NMP (*i.e.* displayed on the graph in Figure 49 by the ~1657 cm^{-1} C=O stretching vibration). The FTIR spectra were recorded at various pH levels during the acid exposure, to assess also the onset of conductivity in emeraldine film.

A comparison of the spectra taken at two pH levels in aqueous hydrochloric acid (*i.e.* 3.88 and 1.75) displayed in Figure 51 show that the two spectra are identical, therefore no protonation had begun at the pH of 1.75.

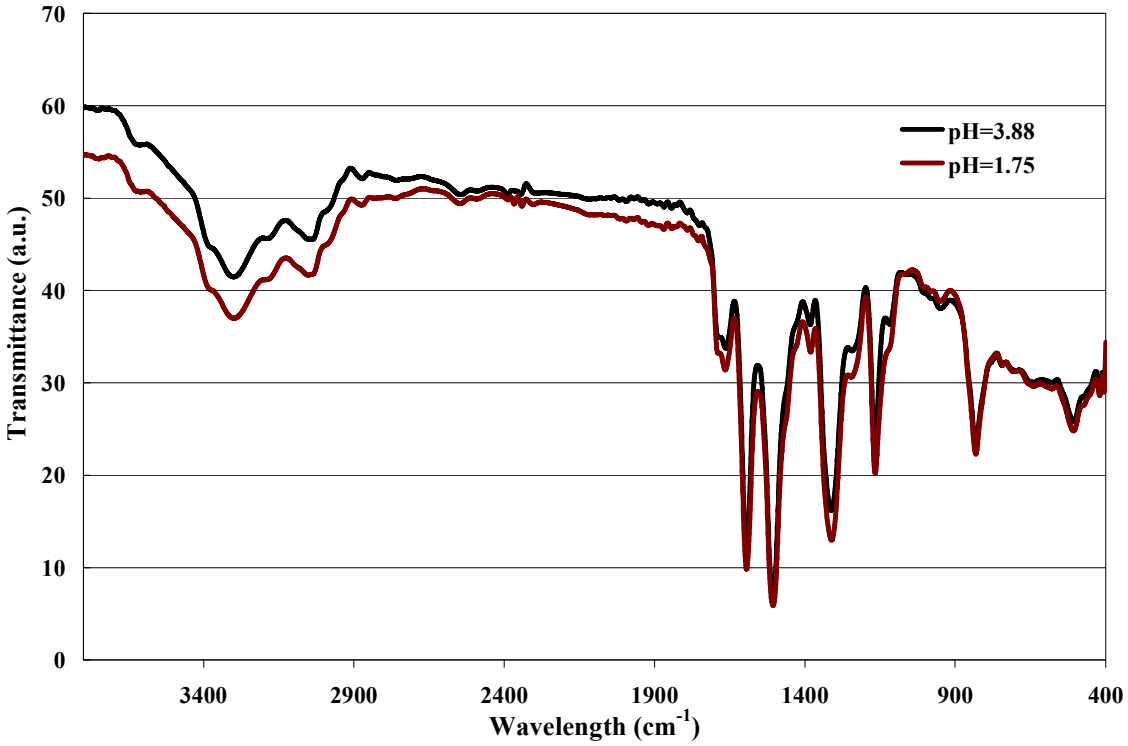

Figure 51. Comparison of the FTIR spectra for emeraldine base treated in HCl solution of pH = 3.88 and 1.75.

On the other hand, the exposure of emeraldine base to the next employed pH of 1.11 displayed in Figure 52 shows that the protonation in emeraldine base had started at a pH

intermediate between 1.75 and 1.11. This protonation event is indicated by the growing of both peaks centered at 1302 cm^{-1} and 1165 cm^{-1} and the shift of the 1165 cm^{-1} peak to 1142 cm^{-1}, as displayed in Figure 52. The peak at 1142 cm^{-1} becomes the highest peak in the spectrum, a fact already reported elsewhere [149,160,162,167,239]. Due to its dense morphology and a greater thickness compared to the film deposited on interdigitated electrode (which showed an onset of conductivity at pH = 2.25), no conductivity change was detected on FTIR spectra at pHs greater than 1.75 for this film deposited on glass slide, even though the films were deposited from the same stock solution.

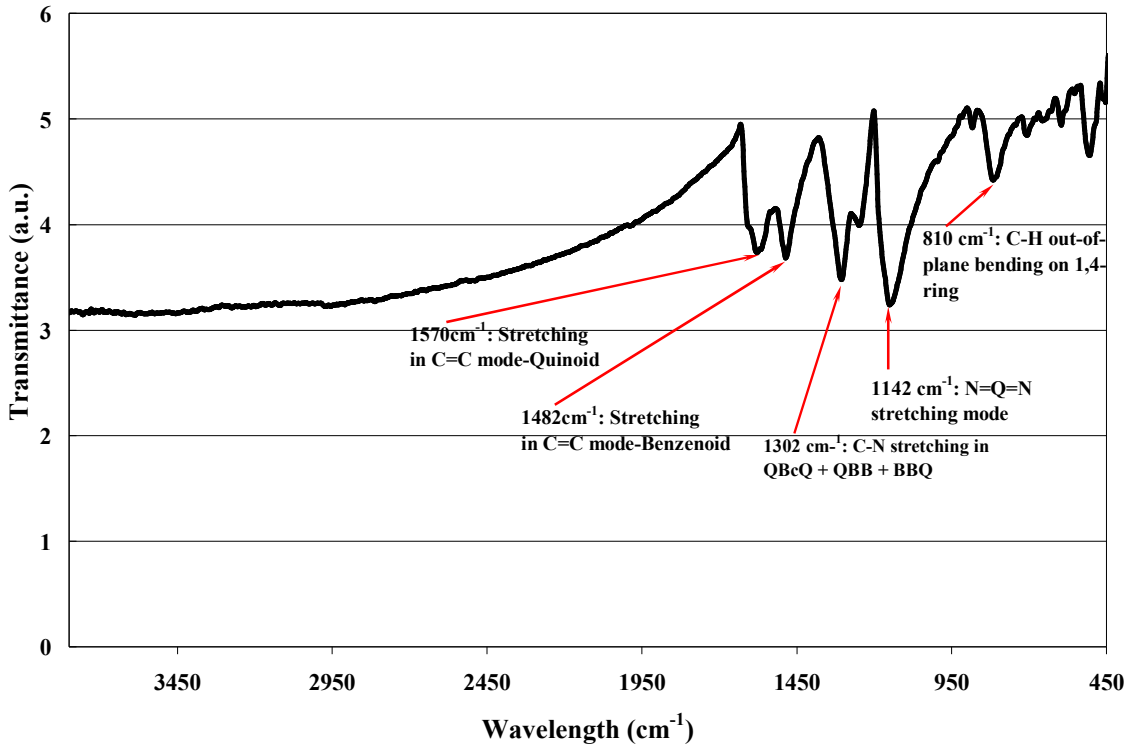

Figure 52. FTIR spectrum of the EB film treated in pH = 1.11.

A comparison of the FTIR spectra taken with the film equilibrated in pure water after the acid base treatment and for 10 minutes in carbonic acid solution of pH = 3.95 is

displayed in Figure 53. Inspecting the graph can be concluded that there is no indication that the complexation of imine sites occurred. The only accomplishment of the acid-base treatment is represented by the removal of the NMP residue, proved by the disappearance of the peak centered at ~1660 cm^{-1} and the persistence of a small shoulder centered at ~1665 cm^{-1} instead.

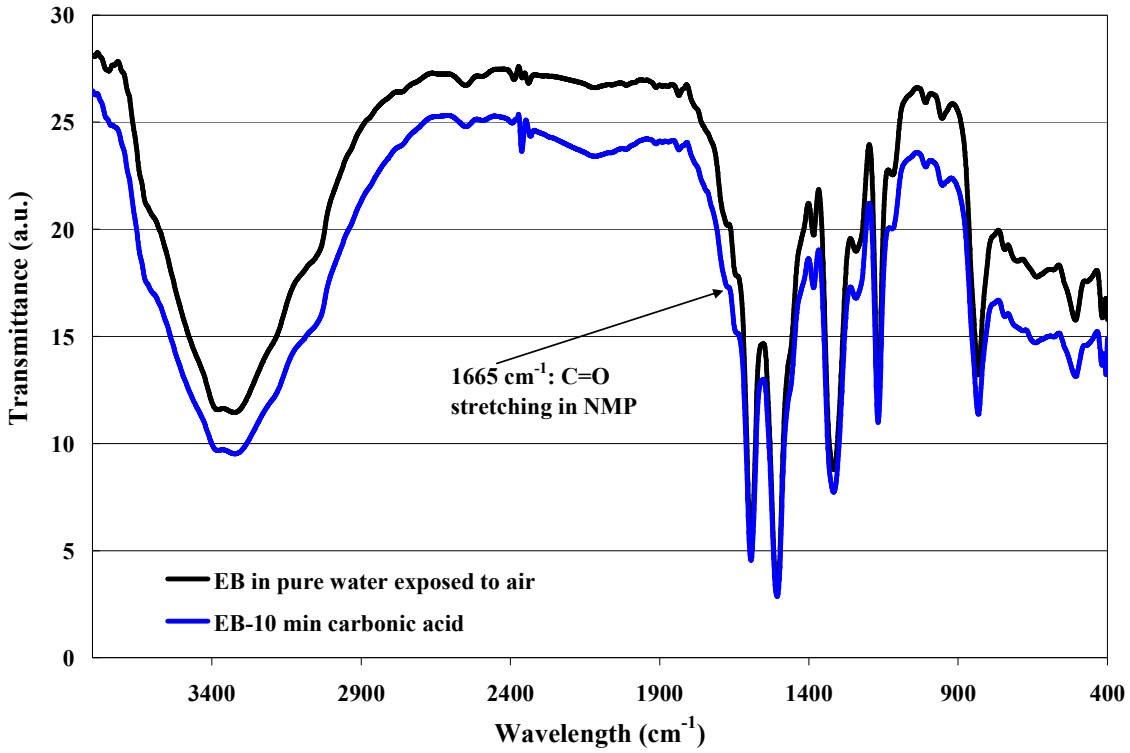

Figure 53. Comparison of the FTIR spectra between the films equilibrated in water and in carbonic acid solution of pH = 3.95 for 10 minutes. The spectra is recorded after the acid-base treatment of the film was accomplished.

3.2.3. Response of the Sensor in Ar-CO_2 mixtures

Having the sensor response assessed in hydrochloric solutions of various pHs, in aqueous solutions of saturated carbonic acid (pH ≅ 4), and in solutions of intermediate pH generated through bubbling of unpurified argon (pH ≅ 4.65), attempts were made to

assess the minimal concentration of carbon dioxide that the sensor could detect. Therefore, various mixtures of ultra pure carbon dioxide gas and purified argon gas were bubbled through pure deionized water and the respective pH generated measured.

The sensor employed for these measurements was the sensor whose conductivity response to hydrochloric acid is displayed in Figure 43b in appendix. Between the measurements in hydrochloric acid and in carbonic acid, 11 months interval elapsed. All this time the sensor was preserved in water in a sealed beaker to avoid evaporation. After 11 months of preservation, the conductivity displayed by the sensor in pure water of pH = 7 in which was equilibrated increased by a factor of 5.

The sensor tested in carbonic acid solutions of various pHs displayed a second semicircle formation at a pH of 5.85, generated by bubbling a mixture of Ar-0.015% CO_2 for 30 minutes in deionized water. The pH at which this sensor formed the second semicircle is in fact 0.83 pH units higher than the sensor described throughout the "immerse sensor part" of the current project. Figure 54 presents the resistance response of the sensor with various pH levels generated by bubbling the two-gases mixture in pure water.

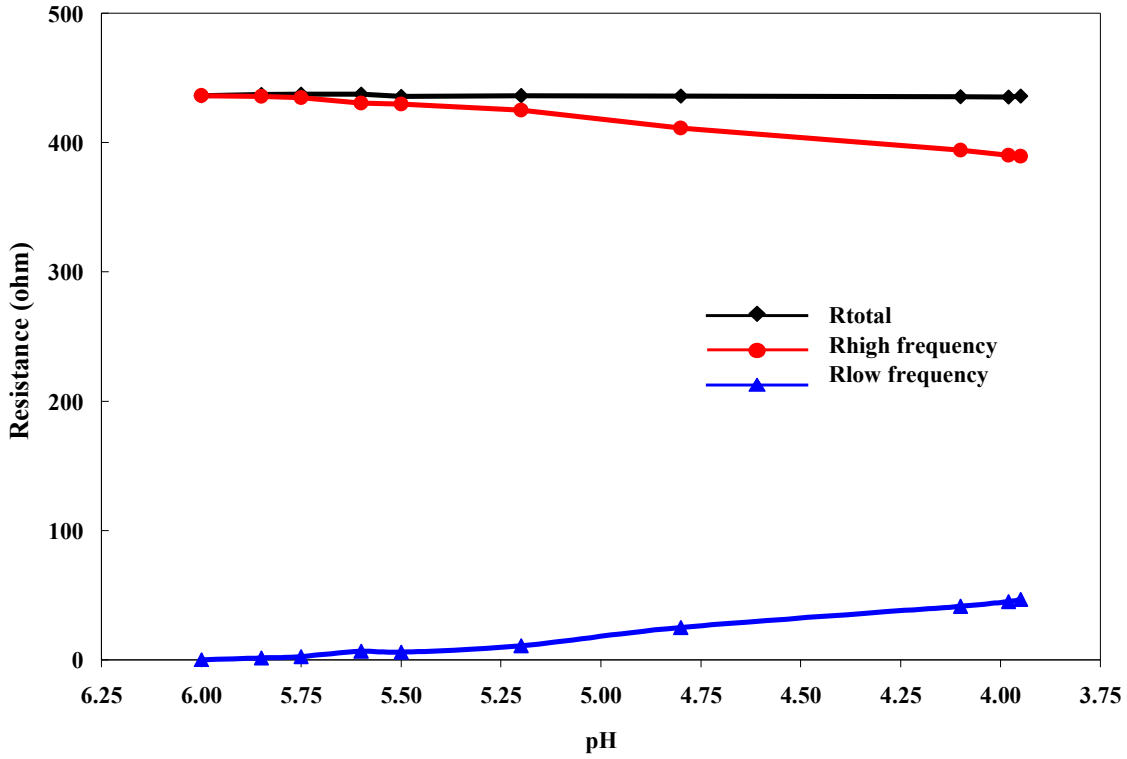

Figure 54. Resistance of emeraldine base thin film as a function of pH of carbonic acid, generated through bubbling of various mixtures of carbon dioxide and argon in deionized water.

The appearance of the second semicircle at 0.0150% CO_2 (*i.e.* 150 ppm CO_2) is displayed in Figure 55.

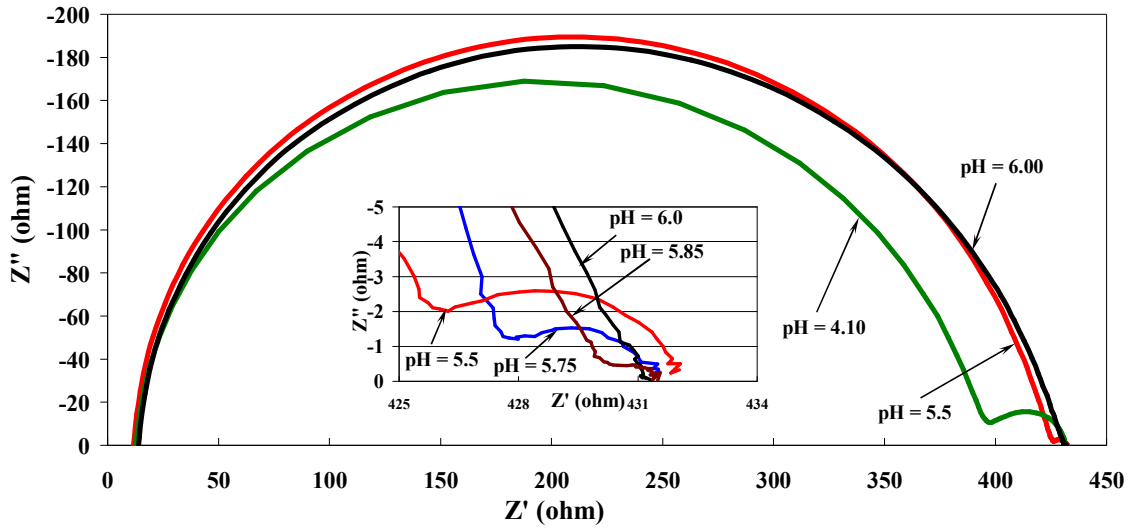

Figure 55. The appearance of the second semicircle at a pH of 5.85, generated by bubbling a mixture of Ar-0.015% CO_2 for 30 minutes in pure deionized water

Figure 56 displays the evolution of the resistance of the initial semicircle (denominated as $R_{high\ frequency,}$ measured with interdigitated electrode) with concentration of carbon dioxide in the gas mixture displayed on logarithmic scale. On the same graph is plotted the pH generated in the aqueous solution (measured with pH meter) as a function of CO_2 concentration. The measurements with these two techniques were performed simultaneously. The good correlation between these results is suggestive to a pH response of the emeraldine base thin film, a fact already observed in hydrochloric acid solutions (Figure 41).

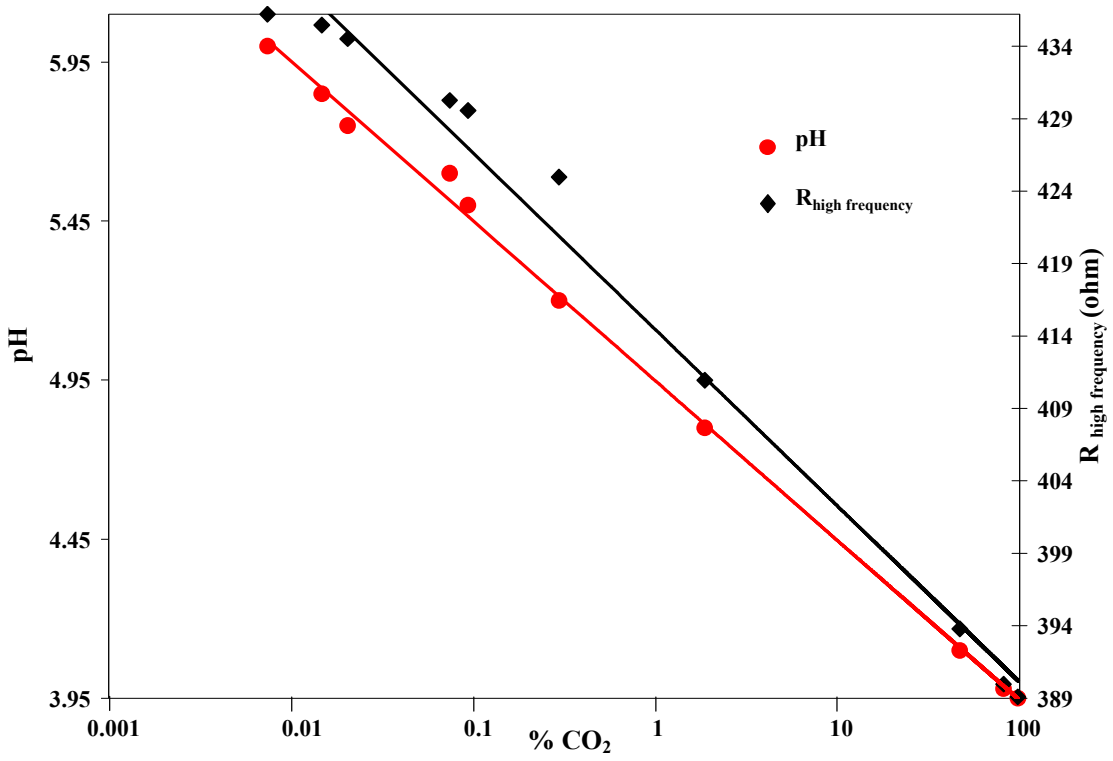

Figure 56. The high frequency resistance of the emeraldine thin film as a function of carbon dioxide concentration in Ar-CO_2 mixture (black) and pH response of solution to bubbling carbon dioxide (red)

The impedance of the emeraldine base film measured at two different fixed frequencies (1 Hz and 3.2 kHz) in carbonic acid (Ar-CO_2 bubbled through water) is shown in Figure 57. The two sets of measurements (in carbonic acid, Figure 57 and hydrochloric acid, Figure 45) were performed with two different interdigitated electrodes so the magnitudes of the resistances were different. The fixed frequency used to calculate the impedance was chosen to maximize the dynamic range of the sensor. In both cases the high frequency measurement produces a response not observable at 1 Hz, indicating that an oscillating circuit could be used to sense changes not detectable with DC measurements.

The appearance of the second semicircle may be consistent with the morphological model of emeraldine base reported in the literature [145,182,194,207]. The display of two semicircles on the impedance spectra would therefore be representative of protonation in the insulating matrix, and the resistance decrease of the original semicircle with lowering the pH (*e.g.* as displayed in Figure 38) would suggest the progressive increase in protonation in this initially insulating region. The overall conductivity of the film increases only when the level of protonation in this insulating region reaches a value that allows three-dimensional delocalization of electrons and electron hopping between metallic islands.

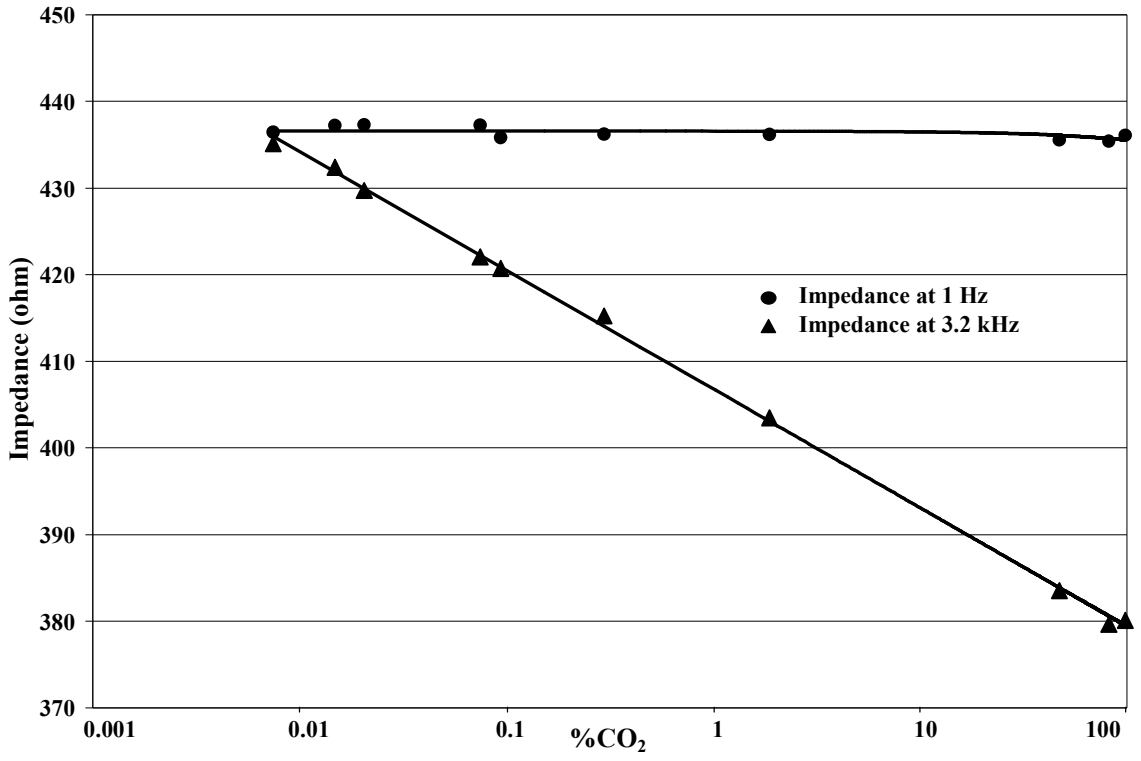

Figure 57. Impedance of emeraldine base thin film for two fixed frequencies as a function of carbon dioxide concentration in argon-CO_2 mixture; a correlation between the carbon dioxide concentration and pH generated in pure water is displayed in Figure 56.

At pHs greater than the level necessary for the onset of conductivity change, the film response is governed by the electron transfer mechanism (the virtually constant capacitance of the first semicircle in these pHs displayed in Figure 42 being suggestive to no limitation in the counter ion diffusion). When the onset of conductivity increase is established, the conduction mechanism is governed by both electron transfer (the shape of impedance curve is a semicircle, suggestive to an electron transfer as the slowest mechanism [209]) and diffusion (the first semicircle capacitance has a parabolic dependence, suggestive to a diffusion controlled process).

The formation of the second semicircle appears to depend on the initial conductivity of the emeraldine base film, since a film displaying an initial conductivity of 4.78×10^{-3} S/cm formed the second semicircle at a pH of 5.85.

3.2.4. Conclusions

The emeraldine base sensor developed in the second part of the project presents some interesting features, not yet reported in the literature. First, the appearance of the second semicircle in the impedance spectra, due to an activated conduction mechanism at pHs lower than 6.0 was not reported yet. The overall resistance of the film follows closely the curve depicted by Chiang, Huang and MacDiarmid [160-162]. The use of impedance spectroscopy makes the emeraldine base thin film act as a pH sensor even at pH levels where there is virtually no protonation and therefore no measurable increase in the film conductivity.

The emeraldine base can be used for detection of carbon dioxide in water equilibrium, but the response is governed by the pH change induced by the formation of carbonic acid.

The sensor needs water abundantly, which is insufficiently provided by the matrix of polyvinyl alcohol. Depending on the local arrangement in the emeraldine film, the onset of second semicircle appearance (*i.e.* the onset of protonation in the insulating region of the polymer) can occur at various pHs, a value as high as 5.85 being recorded with this type of sensor.

The sensor developed in the second part of this work can find its suitability in monitoring the pH change of liquid samples. The appearance of the second semicircle would be indicative of pH dropping below a specific threshold.

Single frequency AC impedance measurements allows for the use of emeraldine base polyaniline (and probably other conductive polymers) in pH sensing applications at protonation levels above the threshold for generation of a total conductivity change and thus expands opportunities for sensor development.

4. FUTURE WORK

Future research should be aimed towards analyzing the conductivity properties of emeraldine base prepared in different conditions given by powder fabrication history, molecular weight, NMP solution characteristics (water uptake, concentration), etc.

The current project cannot conclude if there is a direct correlation between the initial conductivity of the emeraldine film and the pH level at which the second semicircle starts forming, therefore future research should be accomplished in order to elucidate this behavior of emeraldine base. In addition, the extent of increase in conductivity during preservation in water should be evaluated for emeraldine films produced from stock powders with different fabrication history.

The effect of low pressure over the conductivity of emeraldine base should be carefully investigated since cycling the polymer between low pressure and atmospheric pressure could induce a conductivity variation and therefore preclude the use of vacuum pump as an experimental technique.

The usefulness of poly(vinyl alcohol) as a water pool should be further evaluated in order to assess whether the removal of NMP residue play a part in water uptake characteristics of PVA. This will allow the emeraldine base thin film to detect carbon dioxide without the need of inserting the sensor in water.

The fabrication of emeraldine base with 50% oxidation states should be attempted, by controlling the oxygen partial pressure during the polymerization reaction. Then the conduction properties of this material should be carefully investigated.

5. REFERENCES

[1] Meridian Diagnostics EMISA Test Specifications Sheet, E Coli O157:H7 (1988).

[2] Neogen Corporation, "Reveal for Salmonella Sensitivity Tests" Test Specifications Sheet, Salmonella (1998).

[3] J.P.E. Anderson, K.H. Domsch, "Measurement of Bacterial and Fungal Contributions to Respiration of Selected Agricultural and Forest Soils", Canadian J. Microbiol., 21 (1975) 314-321.

[4] J.P.E. Anderson, K.H. Domsch, "A Physiological Method for the Quantitative Measurement of Microbial Biomass in Soils", Soil Biol. Biochem., 10(3) (1978) 215-221.

[5] T. Harden, R.G. Joergensen, B. Meyer, V. Wolters, "Soil Microbial Biomass Estimated by Fumigation-Extraction and Substrate-Induced Respiration in Two Pesticide-Treated Soils", Soil Biol. Biochem. 25(6) (1993) 679-683.

[6] O. Dilly, J.C. Munch, "Microbial Biomass Content, Basal Respiration and Enzyme Activities During the Course of Decomposition of Leaf Litter in a Black Alser (Alnus Glutinosa L. Gaerten) Forest", Soil Biol. Biochem., 28(8) (1996) 1073-1081.

[7] T. Nordgren, E. Baath, B. Sonderstrom, "Evaluation of Soil Respiration Characteristics to Assess Heavy Metal Effects on Soil Microorganisms Using Glutamic Acid as a Substrate", Soil Biol. Biochem., 20(6) (1988) 949-954.

[8] K. Chander, P.C. Brookest, "Microbial Biomass Dynamics During the Decomposition of Glucose and Maize in Metal-Contaminated and Non-Contaminated Soils", Soil Biol. Biochem. 23(10) (1991) 917-925.

[9] P.A. Hartman, B. Swaminathan, M.S. Curiale, R. Firstanberg-Eden, A.N. Sharpe, N.A. Cox, D.Y.C. Fung, C. Goldschmidt, "Rapid Methods and Automation", in C. Vanderzant and D.F. Splittstosser (Eds.), Compendium of Methods for the Microbiological Examination of Foods (Am. Publ. Health Assoc., Arlington, VA, 1992), 665-746.

[10] C.H. Threlkeld, "Detection of Microbial Contamination Utilizing an Infrared CO_2 Analyzer", J. Food Sci., 47 (1982) 1222-1225.

[11] D.E. Townsend, A. Naqui, “Comparison of SimPlate Total Plate Count Test with Plate Count Agar Method for Detection and Quantitation of Bacteria in Food”, J. AOAC Int., 81(3) (1998) 563-569.

[12] C.F. Smith, D.E. Townsend, “A New Medium for Determining the Total Plate Count in Food”, J. Food Protection, 62(12) (1999) 1404–1410.

[13] S.Y. Chew, Y.H.P. Hsieh, “A Rapid CO_2 Evolution Method for Determining Shelf Life of Refrigerated Catfish“, J. Food Sci., 63(5) (1998) 768-771.

[14] Y.P. Hsieh, Y.H.P. Hsieh, “Simple System for a Rapid Determination of Carbon Dioxide Evolution Rates”, J. AOAC Internat., 81(3) (1998), 652-656.

[15] Y.P. Hsieh, Y.H.P. Hsieh, “Determination of Carbon Dioxide Evolution Rates Using a Novel Noninstrumental Microrespirometer”, J. AOAC Internat., 83(2) (2000) 277-281.

[16] H.H. Mobius, “Galvanic Solid Electrolyte Cells for the Measurement of CO_2 Concentrations”, J. Solid. State. Electrochem., 8 (2004) 94-109.

[17] N. Yamazoe, N. Miura, “Gas Sensors Using Solid Electroltes”, MRS Bulletin, June (1999), 37-43.

[18] R.W. Stow, R.F. Baer, B. Randall, “Rapid Measurement of the Tension of Carbon Dioxide in Blood”, Arch. Phys. Med. Rehabil., 38 (1957) 646-650.

[19] W. Severinghaus, A.F. Bradley, “Electrodes for Blood p_{O2} and p_{CO2} Determination”, J. Appl. Physiol., 13 (1958) 515-520.

[20] C.E.W. Hahn, “Electrochemical Analysis of Clinical Blood-Gases, Gases and Vapors”, Analyst, 123(6) (1998), 57R-86R.

[21] C.R. Caflisch, N.W. Carter, “A Micro p_{CO2} Electrode”, Anal. Biochem., 60 (1974) 252–257.

[22] A.K. Covington, R.A. Robinson, M. Sarbar, “Determination of Carbonate in Presence of Hydroxide; Part I: Analysis of First Derivative Potentiometric Curves”, Anal. Chim. Acta, 100 (1978) 367-374.

[23] A.K. Covington, R.A. Robinson, M. Sarbar, “Determination of Carbonate in Presence of Hydroxide; Part II: Evidence for the Existence of Novel Species from First Derivative Potentiometric Titration Curves”, Anal. Chim. Acta, 130 (1981) 93-102.

[24] A.K. Covington, R.N. Goldberg, M. Sarbar, "Computer Simulation of Titration Curves with Application to Aqueous Carbonate Solutions" Anal. Chim. Acta, 130 (1981) 103-109.

[25] D. de Beer, A. Glud, E. Epig, M. Kuhl, "A Fast Responding CO_2 Microelectrode for Profiling Sediments, Microbial Mats and Biofilms ", Limnol. Oceanogr., 42(7) (1997) 1590-1600.

[26] S. Hanstein, D. de Beer, H.H. Feele, "Miniaturized Carbon Dioxide Sensor Designed for Measurements Within Plant Leaves", Sens. Actuators B, 81 (2001) 107-114.

[27] S. Yao, M. Wang "Electrochemical Sensor for Dissolved Carbon Dioxide Measurement", J. Electrochem. Soc., 149 (1) (2002) H28-H32.

[28] H. Beyenal, C.C. Davis, Z. Lewandowski, "An Improved Severinghaus Type Carbon-Dioxide Microelectrode for Use in Biofilms", Sens. Actuators B 97 (2004) 202-210.

[29] T. Sekiguchi, Y. Nagai, T. Makino, K. Ohno, M. Nakamura, H. Hosaka, H. Sakio, S. Ohtsu, H. Takahashi, "Gastric P_{CO2} Monitoring System Based on a Double Membrane Type P_{CO2} Sensor", Sens. Actuators B, 49 (1998), 171-178.

[30] H. Suzuki, H. Arakawa, S. Sasaki, I. Karube, "Micromachined Severinghaus-Type Carbon Dioxide Electrode", Anal. Chem., 71 (1999) 1737–1743.

[31] W.J. Cai, C.E. Reimers "The Development of pH and p_{CO2} Micoelectrodes for Studying the Carbonate of Pore Waters Near the Sediment-Water Interface", Limnol. Oceanogr., 38 (1993) 1762-1773.

[32] Y.J. Zheng, K.M. Merz, Mechanism of the Human Carbonic Anhydrase II Catalyzed Hydration of Carbon Dioxide, J. Am. Chem. Soc. 114 (1992) 10498–10507.

[33] C. Cammaroto, L. Diliberto, M. Ferralis, R Manca, A. Sanna, M. Giordano, "Use of Carbonic Anhydrase in Electrochemical Biosensors for Dissolved CO_2", Sens. Actuators B, 48 (1998) 439–447.

[34] P. Zhao, W.J. Cai, "An Improved Potentiometric p_{CO2} Microelectrode, Anal. Chem. 69 (1997) 5052–5058.

[35] F.J.W. Roughton, A.M. Clark, "Carbonic Anhydrase", in: J.B. Summer, K. Myrback (eds.), "The Enzymes. Chemistry and Mechanism of Action": Part 2, Vol. 1, Academic Press, New York, 1951, pp. 1250-1265

[36] T. Komada, C.E. Reimers, S.E. Boehme, "Dissolved Inorganic Carbon Profiles and Fluxes Determined Using pH and p_{CO2} Microelectrodes", Limnol. Oceanogr., 43(5) (2001) 769–781.

[37] H.A. Himpler, S.F. Brand, M.J.D. Brand, "Conductimetric Gas Sensor for Carbon Dioxide" Anal. Chem., 50 (1978) 1623.

[38] C.M. Santegoeds, A. Schramm, D. de Beer, "Microsensors as a Tool to Determine Chemical Microgradients and Bacterial Activity in Wastewater Biofilms and Flocs", Biodegradation 9 (1998) 159–167.

[39] A.N. Bezbaruah, T.C. Zhang, "Fabrication of Anodically Electrodeposited Iridium Oxide Film pH Microelectrodes For Microenvironment Studies", Anal. Chem., 74 (2002) 5726–5733.

[40] P. Van Houdt, Z. Lewandowski, B. Little, Iridium Oxide pH Microelectrode", Biotechnol. Bioeng., 40 (1992) 601–608.

[41] T. Ishiji, K. Takashashi, A. Kira, "Amperometric Carbon Dioxide Gas Sensor Based on Electrode Reduction of Platinum Oxide", Anal Chem., 65 (1993) 2736-2739.

[42] W. J. Albery, P. Barron, "A Membrane Electrode for the Determination of CO_2 and O_2", J. Electroanal. Chem., 138 (1982) 79-87.

[43] F. Qian, J. Lu, Z. Zhou, C. Cha, "Combined Amperometric Sensors for Simultaneous Measurement of carbon Dioxide and Oxygen", Sens. Actuators B, 17 (1993) 77-83

[44] H. Suzuki, T. Hirakawa, T. Hooshi, H. Toyooka, "Micromachined Sensing Module for p_{O2}, p_{CO2} and pH and its Design Optimization for Practical Use", Sens. Actuators B, 76 (2001), 565-572.

[45] Z.B. Zhou, Q.H. Wu, C.C. Liu, "Microfabricated Thin-Film Microelectrode for Amperometric Determination of CO_2 in the Gas Phase", Sens. Actuators B, 21 (1994) 101-108.

[46] J. Evans, D. Pletcher, P.R. Warburton, T.K. Gibbs, "Amperometric Sensor for Carbon Dioxide: Design, Characteristics and Performance", Anal. Chem., 61 (1989) 577-580.

[47] J. Evans, D. Pletcher and P.R.G. Warburton, T.K. Gibbs, "A New Electrochemical Sensor for Carbon Dioxide Part 2. Study of the Sensor Chemistry", J. Electroanal. Chem., 262 (1989) 119-129.

[48] T. Ishiji, D.W. Chipman, T. Takahashi, K. Takahashi, "Amperometric Sensor for Measurement of Dissolved Carbon Dioxide in Seawater", Sens. Actuators B, 76 (2001) 265-269.

[49] R. Fasching, F. Keplinger, G. Hanreich, G. Hobst, G. Urban, F. Kohl, R. Chabicovsky, "A Novel Miniaturized Sensor for Carbon Dioxide Dissolved in Liquids", Sens. Actuators B, 78 (2001) 291-297.

[50] R. Fasching, F. Kohl, G. Urban, "A Miniaturized Amperometric CO_2 Sensor Based on Dissociation of Copper Complexes", Sens. Actuators B, 93 (2003) 197-204.

[51] J.D. Wadhawan, P.J. Welford, H.B. McPeak, C.E.W. Hahn, R.G. Compton "The Simultaneous Voltammetric Determination and Detection of Oxygen and Carbon Dioxide. A Study of The Kinetics of the Reaction Between Superoxide and Carbon Dioxide in Non-Aqueous Media Using Membrane-Free Gold Disc Microelectrodes", Sens. Actuators B, 88 (2003) 40-52

[52] J.L. Roberts, D.T. Sawyer, "Voltammetric Determination of Carbon Dioxide Using Dimethylsulfoxide as a Solvent", J. Electroanal. Chem., 9 (1965) 1–7.

[53] L.V. Haynes, D.T. Sawyer, "Electrochemistry of Carbon Dioxide in Dimethyl Sulfoxide at Gold and Mercury Electrodes", Anal. Chem., 39 (1967) 332.

[54] T.E. Teeter, P. Van Rysselberghe, "Reduction of Carbon Dioxide on Mercury Cathodes" J. Chem. Phys., 22 (1954) 759-760.

[55] J. Giner, "Electrochemical Reduction of CO_2 on Platinum Electrodes in Acid Solutions", Electrochim. Acta, 8(11) (1963), 857-865.

[56] J. Giner, "The Anodic Oxidation of Methanol and Formic Acid and The Reductive. Adsorption of CO_2 ", Electrochim. Acta, 9(1) (1964), 63-77.

[57] B.R. Eggins, J. McNeil, "Voltammetry of CO_2. Part 1. General Survey of Voltammetry at Different Electrode Materials in Different Solvents", J. Electroanal. Chem., 148 (1983) 17-24.

[58] P.J. Welford, B.A. Brookes, J.D. Wadhawan, H.B. McPeak, C.E.W. Hahn, R.G. Compton, "The Electro-Reduction Of Carbon Dioxide in Dimethylsulphoxide at Gold Microdisc Electrodes: Current/Voltage Wave Shape Analysis", J. Phys. Chem. B, 105 (2001) 5253–5261.

[59] A. Gennaro, A.A. Isse, E. Viannello, "Solubility and Electrochemical Determination of CO_2 in Some Dipolar Aprotic Solvents", J. Electroanal. Chem., 289 (1990) 203–215.

[60] J.L. Roberts Jr., D.T. Sawyer, “Electrochemistry of Oxygen and Superoxide Ion in Dimethylsulfoxide at Platinum Mercury and Gold Electrodes”, J. Electroanal. Chem., 12 (1966) 90–101.

[61] D.T. Sawyer, G. Chiericato Jr., C.T. Angelis, E.J. Nanni Jr., T. Tsuchiya, “Effects of Media and Electrode Materials on the Electroreduction of Dioxygen”, Anal. Chem., 54 (1982) 1720–1724.

[62] J. Sobkowsky, A. Wieckowski, P. Zelenay A. Czerwinski, “Electrochemical Reduction of CO_2 and Oxidation of Adsorbed Species on the Rhodium Electrodes”, J. Electroanal. Chem., 100 (1979) 781-790.

[63] C.E.W. Hahn, “Techniques for Measuring the Partial Pressures of Gases in the Blood. Part I-In Vitro Measurements”, J. Phys. E, 13 (1980) 470-482.

[64] C.E.W. Hahn “Techniques for Measuring the Partial Pressures of Gases in the Blood. Part II-In Vivo Measurements ”, J. Phys. E, 14 (1981) 783-797.

[65] C.E.W. Hahn, H. McPeak, A.M. Bond, D. Clark, “The Development of New Microelectrode Gas Sensors: An Odyssey. Part 1. O_2 and CO_2 Reduction at Unshielded Gold Microdisc Electrodes”, J. Electroanal. Chem., 393 (1995) 61-68.

[66] C.E.W. Hahn, H. McPeak, A.M. Bond, “The Development of New Microelectrode Gas Sensors: an Odyssey. Part 2. O_2 and CO_2 Reduction at Membrane-Covered Gold Microdisc Electrodes”, J. Electroanal. Chem., 393 (1995) 69-74.

[67] H. McPeak, A.M. Bond, C.E.W. Hahn, “The Development of New Microelectrode Gas Sensors: an Odyssey Part IV. O_2, CO_2 and N_2O Reduction at Unshielded Gold Microdisc Electrodes”, J. Electroanal. Chem., 487 (2000) 25-30.

[68] W.J. Albery, D. Clark, H.J.J. Drummond, A.J.M. Coombs, W.K. Young, C.E.W. Hahn, “Pulsed Titration Sensors Part 1: A Breath-by-Breath CO_2 Sensor ” J. Electroanal. Chem., 340 (1992) 99-110.

[69] W.J. Albery, D. Clark, W.K. Young and C.E.W. Hahn, “Pulsed Titration Sensors Part 2. A General Theoretical Model for the Breath-by-Breath CO_2 Sensor”, J. Electroanal. Chem., 340 (1992) 111-126.

[70] J.D. Wadhawan, P.J. Welford, E. Maisonhaute, V. Climent, N.S. Lawrence, R.G. Compton, H.B. McPeak, C.E.W. Hahn, “Microelectrode Studies of the Reaction of Superoxide with Carbon Dioxide in Dimethyl Sulfoxide”, J. Phys. Chem. B, 105 (2001) 10659-10668.

[71] Z.B. Zhou, W.J. Liu, C.C. Liu, "Non-Invasive, Real-Time and Dynamic Monitoring of CO_2 and O_2 Simultaneously Using Modulated Potential Pulse-Amperometry: Coulometry", Sens. Actuators B, 52 (1998) 219–225.

[72] J.L. Roberts, T.S. Calderwood, D.T. Sawyer, "Nucleophilic Oxygenation of Carbon Dioxide by Superoxide Ion in Aprotic Media To Form the $C_2O_6^{2-}$ Species", J. Am. Chem. Soc., 106 (1984) 4667-4670.

[73] J.R. Cain, L.C. Maxwell, "An Electrolytic Resistance Method for Determining Carbon in Steel", J. Ind. Eng. Chem., 11(9) (1919) 852-860.

[74] I.B. Holm-Jensen, "A New Gas Absorption Device Its Application to Titrimetric and Conductometric Micro Determinations of Carbon Dioxide in Air", Anal. Chim. Acta, 23 (1969) 13-27.

[75] R. H. Maffly, "A Conductometric Method for Measuring Micromolar Quantities of Carbon Dioxide" Anal. Biochem., 23 (1968) 252-262.

[76] D.B. James, "An Instrument for Gas Analysis", Biomed. Eng., 4(3) (1969) 126-133.

[77] K. Lis, H. Acker, D.W. Lubbers, M.Halle, "A p_{CO2} Surface Electrode Working on the Principle of Electrical Conductivity", Pflugers Arch., 381 (1979) 289-291.

[78] S. Bruckenstein, J.S. Symanski, "Continuous Conductometric Sensor for Carbon Dioxide", Anal. Chem., 58(8) (1986) 1766-1770.

[79] A.R. Varlan, W. Sansen, "Micromachined Conductometric p_{CO2} Sensor", Sensors and Actuators B, 44 (1997) 309-315.

[80] S. Bruckenstein, J.S. Symanski, "Analytical Applications of Gas Membrane Electrodes", J. Chem. Soc. Faraday Trans. 1, 82(4), (1986) 1105 – 1116**.**

[81] Y. Saikai, Y. Sadaoka, M. Matsuguchi, H. Yokouchi, K. Tamai, "Effect of Carbon Dioxide on the Electrical Conductivity of Polyethylene Glycol-Alkali Carbonate Complex Film", Mater. Chem. Phys., 42 (1995) 73-76.

[82] Z.B. Zhou, W.J. Liu, C.C. Liu, "Studies on The Biomedical Sensor Techniques for Real-Time and Dynamic Monitoring of Respiratory Gases, CO_2 and O_2", Sens. Actuators B, 65 (2000) 35–38.

[83] Z.B. Zhou, L.D. Feng, W.J. Liu, Z.G. Wu, "New Approach for Developing Transient Electrochemical Multi-Component Gas Sensors", Sens. Actuators B, 76 (2001) 605-609.

[84] B. van der Schoot, P. Bergveld, "The Coulometric Carbon Dioxide Sensor, a New Type of Chemical Transducer", Proceedings of the Second International Meeting on Chemical Sensors, Bordeaux, 1986, 665–668.

[85] W.J. Albery, M. Uttamlal, "A CO_2 Titration Electrode Part I: Theoretical Description", J. Appl. Electrochem., 24 (1994) 8-13.

[86] W.J. Albery, M. Uttamlal, M.S. Appleton, N.J. Freeman, B.B. Kebbekus, M.D. Neville, "A CO_2 Titration Electrode Part II: Development of the Sensor", J. Appl. Electrochem., 24 (1994) 14-17.

[87] T. Trapp, B. Boss, K. Cammann, E Schirmer, C. Berthold, "Development of a Coulometric CO_2 Gas Sensor", Sens. Actuators B, 50 (1998) 97-103.

[88] K. Wiegran, T. Trapp, K. Cammann, "Development of a Dissolved Carbon Dioxide Sensor Based on Coulometric Titration" Sens. Actuators B, (1999) 120-124.

[89] H.C. Chiu, A.C.C. Tseung, "Electrochemical CO_2 Sensor Based on CO_2 Reduction and Subsequent CO Oxidation on Pt/WO_3 Electrode", J. Electrochem. Soc. Lett., 2(10) (1999) 540-541.

[90] P. Bergveld, "Development, Operation and Application of the Field Effect Transistor as a Tool for Electrophysiology", IEEE Trans. Biomed. Eng., BME 19 (1972) 342-351.

[91] J. Shaw, "Bilayer Membrane for ISFETs to Eliminate CO_2 Mediated pH Sensitivity", Sens. Actuators B, 15-16 (1993) 81-85.

[92] H. H. Van Den Vlekkert, N. F. De Rooij, A. Van Den Berg, A. Grisel, "Multi-Ion Sensing System Based on Glass-Encapsulated pH-ISFETs and a Pseudo-REFET", Sens. Actuators B. 1 (1990) 395-400.

[93] M. Trojanowicz, Z. Augustowska, W. Matuszewski, G.Moraczewska, A. Hulanicki, "A Potassium-Selective Electrode With Solid Internal Contact", Talanta, 29 (1982) 113-117.

[94] X. Li, E.M.I. Verpoorte, D. J. Harrison, "Elimination of Neutral Species Interference at the Ion-Sensitive Membrane/Semiconductor Device Interface", Anal. Chem., 60 (1988) 493-498.

[95] P. Herman, Z. Murtaza, J.R. Lakowicz, "Sensing of Carbon Dioxide by a Decrease in Photoinduced Electron Transfer Quenching", Anal. Biochem., 272 (1999) 87–93.

[96] M.D. Marazuela, M.C. Moreno-Bondi, G. Orellana, "Enhanced Performance of a Fiber Optic Luminescence CO_2 Sensor Using Carbonic Anhydrase", Sens. Actuators B, 29 (1995) 126-131.

[97] O.S. Wolfbeis, L.J. Weis, M.J.P. Leiner, W.E. Ziegler, "Fiber Optic Fluorosensor for Oxygen and Carbon Dioxide", Anal. Chem., 60 (1988) 2028–2030.

[98] E. M. Hampe, D. M. Rudkevich, "Exploring Reversible Reactions between CO_2 and Amines", Tetrahedron, 59 (2003) 9619-9625.

[99] S.J. Yoon, H. Lee, "Substituent Effect in Amine-CO_2 Interaction Investigated by NMR and IR Spectroscopies", Chem Lett., 32(4) (2003) 324-325.

[100] Z.H. Lan, H.A. Mottola, "Carbon Dioxide-Enhanced Luminol Chemiluminescence in the Absence of Added Oxidant", Analyst, 121(2) (1996), 211-218.

[101] M.F. Choi, P. Hawkins, "Novel Dye-Solvent Solutions for the Simultaneous Detection of Oxygen and Carbon Dioxide", Anal. Chem. 67 (1995) 3897–3902.

[102] C.G. Cooney, B.C. Towe, R.C. Eyster, "Optical pH, Oxygen and Carbon Dioxide Monitoring Using a Microdialysis Approach", Sens. Actuators B, 69 (2000) 183-188.

[1031] B.H. Weigl, A. Holobar, N.V. Rodriguez, O.S. Wolfbeis, "Chemically and Mechanically Resistant Carbon Dioxide Optrode Based on a covalently Immobilised pH Indicator", Anal. Chim. Acta 282 (1993) 335–343.

[104] B.H. Weigl, O.S. Wolfbeis, "New Hydrophobic Materials for Optical Carbon Dioxide Sensors Based on Ion Pairing", Anal. Chim. Acta 302 (1995) 249–254.

[105] J. Dubendorfer, R.E. Kunz, G. Jobst, I. Moser, G. Urban, "Integrated Optical pH Sensor Using Replicated Chirped Grating Coupler Sensor Chips", Sens. Actuators B, 50 (1998) 210–219.

[106] E.M. Hampe, D.M. Rudkevich, "Reversible Covalent Chemistry of CO_2", Chem. Commun., (2002) 1450–1451.

[107] A. Mills, Q. Chang, N. McMurray, "Equilibrium Studies on Colorimetric Plastic Film Sensors for Carbon Dioxide", Anal. Chem. 64 (1992) 1383-1389.

[108] B.H. Weigl, O.S. Wolfbeis, "Sensitivity Studies on Optical Carbon Dioxide Sensors Based on Ion Pairing", Sens. Actuators B, 28 (1995) 151-156.

[109] J.W. Parker, O. Laksin, C. Yu, M.L. Lau, S. Klima, R. Fisher, I. Scott, B.W. Atwater, "Fiber Optic Sensors for pH and Carbon Dioxide Using a Self-Referencing Dye", Anal. Chem., 65 (1993) 2329–2334.

[110] A. Mills, C. Chang, "Fluorescent Plastic Thin Film Sensor for Carbon Dioxide", Analyst, 118(7) (1993) 839-843.

[111] N. Nakamura, Y. Amao, "An Optical Sensor for CO_2 Using Thymol Blue and Europium (III) Complex Composite Film", Sens. Actuators B, 92 (2003) 98–101.

[112] M. Rocchia, E. Garrone, F. Geobaldo, L. Boarino, M. J. Sailor, "Sensing CO_2 in a Chemically Modified Porous Silicon Film", Phys. Stat. Sol. (a), 197(2) (2003) 365– 369.

[113] C. von Bültzingslöwen, A.K. McEvoy, C. McDonagh, B.D. MacCraith, I. Klimant, C. Krause, O.S. Wolfbeis, "Sol–Gel Based Optical Carbon Dioxide Sensor Employing Dual Luminophore Referencing For Application in Food Packaging Technology", Analyst, 127(11) (2002) 1478–1483.

[114] O.S. Wolfbeis, L.J. Weis, M.J. P. Leiner, W.E. Ziegler, "Fiber-Optic Fluorosensor for Oxygen and Carbon Dioxide", Anal. Chem., 60 (1988) 2028-2030.

[115] M.D. Marazuela A, M.C. Moreno-Bondi, G. Orellana, "Enhanced Performance of a Fiber-Optic Luminescence CO_2 Sensor Using Carbonic Anhydrase", Sens. Actuators B, 29 (1995) 126-131.

[116] O. Fatibello-Filho, J. F. de Andrade, A.A. Suleiman, G.G. Guilbault, "Piezoelectric Crystal Monitor for Carbon Dioxide in Fermentation Processes", Anal. Chem., 61 (1989) 746-748.

[117] R. Zhou, S. Vaihinger, K.E. Geckeler, W. Gopel, "Reliable CO_2 Sensors with Silicon Based Polymers on Quartz Microbalance Transducers", Sens. Actuators B, 18-19 (1994) 415-420.

[118] M.T. Gomes, A.C. Duarte, J.P. Oliveira, "Comparison of Two Methods for Coating Piezoelectric Crystals", Anal. Chim. Acta, 300 (1995) 329-334.

[119] M.T. Gomes, A.C. Duarte, J.P. Oliveira, "Detection of CO_2 Using Quarts Crystal Microbalance", Sens. Actuators B, 26-27 (1995) 191-194.

[120] M. T. Gomes, A.C. Duarte, J. P. Oliveira, "The Utilization of a Piezoelectric Quartz Crystal for Measuring Carbon Dioxide in Wine " Anal. Chim. Acta, 327 (1996) 95-100.

[121] M.T.S.R. Games, T.A. Rocha, A.C. Duarte, J.A.B.P. Oliveira, "The Performance of a Tetramethylammonium Fluoride Tetrahydrate Coated Piezoelectric Crystal for Carbon Dioxide Detection", Anal. Chim. Acta, 335 (1996) 235–238.

[122] M.T.S.R. Gomes, T.A.P. Rocha, A.C. Duarte, J.A.B.P. Oliveira, "Quantification of CO_2 in Wines with Piezoelectric Crystals Coated with Tetramethylammonium Fluoride and Comparison with Other Methods", Analusis, 26 (1998) 179-182.

[123] M.T.S.R. Gomes, P.S.T. Nogueira, J.B.P. Oliveira, "Quantification of CO_2, SO_2, NH_3, and H_2S with a Single Coated Piezoelectric Quartz Crystal", Sens. Actuators B, 68 (2000) 218–222.

[124] M.S. Nieuwenhuizen, A.J. Nederlof, "A SAW Gas Sensor for Carbon Dioxide and Water. Preliminary Experiments", Sens. Actuators B, 2 (1990) 97-101.

[125] P. C. H. Li, M. Thompson, "Potential Carbon Dioxide Sensing Based on Recognition by Trans-(Carbonyl hydroxyl bis-(Triphenyl phosphine) Rhodium(I)) Deposited on Acoustic Wave Devices", Analyst, 119(9) (1994), 1947-1951.

[126] P.C.H. Li, M. Thompson, "Carbon Dioxide Recognition by Rhodium (I) Complexes Studied by Infrared and Nuclear Magnetic Resonance Spectroscopies and Acoustic Wave Sensor", Analyst, 120(10) (1995) 2529-2535.

[127] K. Korsah, C.L. Ma, B. Dress, "Harmonic Frequency Analysis of SAW Resonator Chemical Sensors: Application to the Detection of Carbon Dioxide and Humidity", Sens. Actuators B, 50 (1998) 110-116.

[128] A.E. Hoyt, A.J. Ricco, J.W. Bartholomew and G.C. Osbourn, "SAW Sensors for the Room Temperature Measurement of CO_2 and Relative Humidity", Anal. Chem., 70 (1998) 2137-2145.

[129] J.W. Grate, M. Klusty, R.A. McGill, M.H. Abraham, G. Whiting, J. Adonian-Haftvan, "The Predominant Role of Swelling-Induced Modulus Change of the Sorbent Phase in Determining the Responses of Polymer-Coated Surface Acoustic Wave Vapor Sensors", Anal. Chem., 64 (1992) 610-624.

[130] J. Lin, M. Heurich, V. Schlichting, E. Obermeier, "Characterization and Optimization of a CO_2 Sensitive Organically Modified Silicate with Respect to Its Use as a Gas Sensor", Sens. Actuators B, 13-14 (1993) 528-529.

[131] C.K. Chiang, C.R. Fincher Jr., Y.W. Park, A.J. Heeger, H. Shirakawa, E.J. Louis, "Electrical Conductivity in Doped Polyacethylene" Phys. Rev. Lett., 39 (1977) 1098-1101.

[132] C.M. Mikulski, P. J. Russo, M. S. Saran, A.G. MacDiarmid, A.F. Garito, A.J. Heeger, "Synthesis and Structure of Metallic Polymeric Sulfur Nitride, $(SN)_x$ and Its Precursor, Disulfur Dinitride, S_2N_2", J. Am. Chem. Soc. 97(22) (1975), 6358-6363.

[133] C.M. Mikulski, A.G. MacDiarmid, A.F. Garito, A.J. Heeger, "Stability of Polymeric Sulfur Nitride, $(SN)_x$ to Air, Oxygen, and Water Vapor", Inorg. Chem., 15(11) (1976) 2943-2945.

[134] R. D. Smith, J. R. Wyatt, J.J. DeCorpo, F.E. Saalfeld, M.J. Moran, A.G. MacDiarmid, "A Study of the Vapor Phase Species of Polymeric Sulfur Nitride, $(SN)_x$", J. Am. Chem. Soc. 99(6) (1977) 1726-1730.

[135] W. P. Su, J. R. Schrieffer, A. J. Heeger, "Solitons in Polyacethylene", Phys. Rev. Lett. 42 (1979) 1698-1701.

[136] W. P. Su, J. R. Schrieffer, A. J. Heeger, "Soliton Excitations in Polyacetylene", Phys. Rev. B, 22 (1980) 2099-2111.

[137] A.J. Heeger "Semiconducting and Metallic Polymers: the Fourth Generation of Polymeric Materials", Synth. Metals, 125 (2002) 23-42.

[138] A. J. Heeger, "Charge Transfer in Conductive Polymers", Faraday Discuss. Chem Soc., 88 (1989) 203-211.

[139] T.J. Lewis, "A Simple General Method for Charge Transfer in Polymers", Faraday Discuss. Chem Soc., 88 (1989) 189-201.

[140] G. Wegner, J. Ruhe, "The Structural Background of Charge-Carrier Motion in Conducting Polymers", Faraday Discuss. Chem Soc., 88 (1989) 333-349.

[141] S. Roth, H. Bleier, W. Pukacki, "Charge Transport in Conducting Polymers", Faraday Discuss. Chem Soc., 88 (1989) 223-233.

[142] A.J. Heeger, "Solitons in Conducting Polymers", Rev. Modern Phys. 60(3) (1989) 781-851.

[143] C.B. Duke, E.M. Conwell, A. Paton, "Localized Molecular Excitons in Polyaniline", Chem. Phys. Lett., 131(1-2) (1986) 82-86.

[144] R.R. Chance, D.S. Boudreaux, J.F. Wolf, L.W. Shacklette, R. Silbey, B. Themas, J.M. Andre, J.L. Bredas, "Polyaniline: A Theoretical Study", Synthetic Metals, 15 (1986), 105-114.

[145] F. Zuo, M. Angelopoulos, A.G. MacDiarmid, A.J. Epstein, "Transport Studies of Protonated Emeraldine Polymer: A Granular Polymeric Metal System", Phys. Rev. B, 36(6) (1987) 3475-3478.

[146] A. J. Epstein, A.G. MacDiarmid, "Polaron and Bipolaron defects in Polymers: Polyaniline", J. Molec. Electronics, 4 (1988) 161-165.

[147] R.P. McCall, J.M. Ginder, M.G. Roe, G.E. Asturias, E.M. Scherr, A.G. MacDiarmid, A.J. Epstein, "Massive Polarons in Large-energy-gap Polymers", Phys. Rev. B, 39(14) (1989) 10174-10178.

[148] T. Oshawa, T. Kabata, O. Kimura, K. Yoshino, "Polaronic Transitions in Electrochemical Polymerized Polyaniline", Synthetic Metals, 29 (1989) E203-E210.

[149] Y.H. Kim, C. Foster, J. Chiang, A.J. Heeger, "Localized Charge Excitations in Polyaniline: Infrared Photoexcitation and Protonation Studies", Synthetic Metals, 29 (1989) E285-E290.

[150] H.H.S. Javadi, F. Zuo, K.R. Cromack, M. Angelopoulos, A.G. MacDiarmid, A.J. Epstein, "Charge Transport in the "Emeraldine" Form of Polyaniline", Synthetic Metals 29 (1989) E409-E416

[151] Y.H. Kim, S.D. Phillips, M.J. Nowak, D. Spiegel, C.M. Foster, G. Yu, J.C. Chiang, A.J. Heeger, "Localization of Charge Excitations in Polyaniline", Synthetic Metals, 29 (1989) E291-E296.

[152] J.K. Avlyanov, S.A. Yakimov, T.A. Usmanov, "Kinetics and Deprotonation of Polyanilines", Synthetic Metals, 41-43 (1991) 635-639.

[153] Z.H. Wang, C. Li, E.M. Scherr, A.G. MacDiarmid, A.J. Epstein, "Three Dimensionality of "Metallic" States in Conducting Polymers: Polyaniline", Phys. Rev. Lett. 66(13) (1991) 1745-1748.

[154] J.G. Masters, Y. Sun, A.G. MacDiarmid, A.J. Epstein, "Polyaniline: Allowed Oxidation States", Synthetic Metals, 41-43 (1991) 715-718.

[155] Z.H. Wang, E.M. Scherr, A.G. MacDiarmid, A.J. Epstein, "Transport and EPR Studies of Polyaniline: a Quasi-on-dimensional Conductor with Three-dimensional "Metallic" States", Phys. Rev. B, 45(8) (1992), 4190-4202.

[156] E.T. Kang, K.G. Neoh, K.L. Tan, "The Protonation-Deprotonation Hysteresis in Polyaniline", Polymer, 37(6) (1996) 925-929.

[157] E.T. Kang, K.G. Neoh, K.L. Tan, "Protonation and Deprotonation of Polyaniline Films and Powders Revisited", Synthetic Metals 68 (1995) 141-144.

[158] E.T. Kang, Z.F. Li, K.G. Neoh, Y.Q. Dong, K.L. Tan, "Protonation and Deprotonation of Polyaniline Films and Powders: Effects of Acid and Base Concentrations on the Surface Intrinsic Oxidation States", Synthetic Metals, 92 (1998) 167-171.

[159] B. Wessling, H. Volk, "Conversion of Doped Polyaniline from the Amorphous to a Partially Crystalline State", Synthetic Metals, 16 (1986) 127-131.

[160] J.C. Chiang, A.G. MacDiarmid, "Polyaniline: Protonic Acid Doping of the Emeraldine Form to the Metallic Regime", Synthetic Metals, 13 (1986) 193-205.

[161] A.C. MacDiarmid, J.C. Chiang, A.F. Richter, A.J. Epstein, "Polyaniline: A New Concept in Conducting Polymers", Synthetic Metals, 18 (1987) 285-290.

[162] W.S. Huang, B.H. Humphrey, A.G. MacDiarmid, "Polyaniline, a Novel Conducting Polymer", J. Chem. Soc. Faraday Trans 1, 82 (1986) 2385-2400.

[163] A. J. Epstein, J.M. Ginder, F. Zuo, H.S. Woo, D.B. Tanner, A.F. Richter, M. Angelopoulos, W.S. Huang, A.G. MacDiarmid, "Insulator-to-Metal Transition in Polyaniline: Effect of Protonation in Emeraldine", Synthetic Metals, 21 (1987) 63-70.

[164] W.S. Huang, A.G. MacDiarmid, A.J. Epstein, "Polyaniline: Non-Oxidative Doping of the Emeraldine Base to the Metallic Regime", J. Chem. Soc., Chem. Commun., (1987) 1784-1786.

[165] A.J. Epstein, A.G. MacDiarmid, "Protonation of Emeraldine: Formation of a Granular Polaronic Polymer Metal", Mol. Cryst. Liq. Cryst., 160 (1988) 165-173.

[166] A. Ray, A.F. Richter, A.G. MacDiarmid, A.J. Epstein, "Polyaniline: Protonation/Deprotonation of Amine and Imine Sites", Synthetic Metals, 29 (1989) E151-E156.

[167] M. Angelopoulos, G.E. Asturias, S.P. Ermer, A. Ray, E.M. Scherr, A.G. MacDiarmid, "Polyaniline: Solution, Films and Oxidation States", Mol. Cryst. Liq. Cryst. 160 (1988) 151-163.

[168] G. E. Asturias, A.G. MacDiarmid, R.P. McCall, A.J. Epstein, "The Oxidation State of "Emeraldine" Base", Synthetic Metals, 29 (1989) E157-E162.

[169] S. Li, H. Dong, Y. Cao, "Synthesis and Characterization of Soluble Polyaniline", Synthetic Metals, 29 (1989) E329-E336.

[170] R.P. McCall, J.M. Ginder, J.M. Leng, H.Y. Ye, S.K. Manohar, J.G. Masters, J.E. Asturias, A.G. MacDiarmid, "Spectroscopy and Defect States in Polyaniline", Phys. Rev. B, 41(8) (1990) 5202-5213.

[171] A. Ray, G.E. Asturias, D.L. Kershner, A.F. Richter, A.G. MacDiarmid, A.J. Epstein, "Polyaniline: Doping, Structure and Derivatives", Synthetic Metals, 29 (1989) E141-E150.

[172] W.S. Huang, A.G. MacDiarmid, "Optical Properties of Polyaniline", Polymer, 34(9) (1993) 1833-1845.

[173] J.E. de Albuquerque, L.H.C. Mattoso, D.T. Balogh, R.M. Faria, J.G. Masters, A.G. MacDiarmid, "A Simple Method to Estimate the Oxidation State of Polyanilines", Synthetic Metals, 113 (2000) 19-22.

[174] J.E. de Albuquerque, L.H.C. Mattoso, R.M. Faria, J.G. Masters, A.G. MacDiarmid, "Study of the Interconversion of Polyaniline Oxidation States by Optical Absorption Spectroscopy", Synthetic Metals 146 (2004) 1-10.

[175] K. Ogura, H. Shiigi, "A CO_2 Sensing Composite Film Consisting of Base-Type Polyaniline and Poly (Vinyl Alcohol)", Electrochem. Solid State Lett., 2(9) (1999) 478-480.

[176] K. Ogura, H. Shiigi, M. Nakayama, A. Ogawa, "Thermal Properties of Poly(anthranilic acid) (PANA) and Humidity-Sensitive Composites Derived from Heat-Treated PANA and Poly (Vinyl Alcohol)", J. Polym. Sci Part A: Polym. Chem., 37 (1999) 4458-4465.

[177] K. Ogura, H. Shiigi, T. Oho, T. Tonosaki, "A CO_2 Sensor with Polymer Composite Operating at Ordinary Temperature", J. Electrochem. Soc, 147(11) (2000) 4351-4355.

[178] H. Shiigi, T. Oho, T. Tonosaki, K. Ogura, "CO_2 Sensitive Characteristics of Base-type Polyaniline / Poly (Vinyl Alcohol) Composites at Room Temperature and Effects of Coexisting Gases", Electrochemistry, 65(12) (2001) 997-1001.

[179] T. Tonosaki, T. Oho, H. Shiigi, K. Isomura, K. Ogura, "Highly Sensitive CO_2 Sensor with Polymer Composite Operating at Room Temperature", Analytical Sciences 17(supplement) (2001) i249-i252.

[180] T. Oho, T. Tonosaki, K. Isomura, K. Ogura, "A CO_2 Sensor Operating Under High Humidity" J. Electroanal. Chem., 522 (2002) 173-178.

[181] F. Koleli, T. Ropke, C.H. Hamann, "The Reduction of CO_2 on Polyaniline Electrode in a Membrane Cell", Synthetic Metals, 140 (2004) 65-68.

[182] A.G. MacDiarmid, A.J. Epstein, "Polyanilines: A Novel Class of Conducting Polymers", Chem, Soc. Faraday Discuss., 88 (1989) 317-332.

[183] A.G. MacDiarmid, G.E. Asturias, D.L. Kershner, S.K. Manohar, A. Ray, E.M. Scherr, Y. Sun, X. Tang, A.J. Epstein, "The Polyanilines: Processing, Molecular Weight, Oxidation States and Derivatives", Polym. Prepr., 30(1) (1989) 147-148.

[184] E.M. Scherr, A.G. MacDiarmid, S.K. Manohar, J.G. Masters, Y. Sun, X. Tang, M.A. Druy, P.J. Glatkowski, V.B. Cajipe, J.E. Fischer, K.R. Cromack, M.E. Jozefowicz, J.M. Ginder, R.P. McCall, A.J. Epstein, "Polyaniline: Oriented Films and Fibers", Synthetic Metals, 41-43 (1991) 735-738.

[185] A.G. Green, A.E. Woodhead, "Aniline Black and Allied Compounds-Part 1", J. Chem. Soc., 97 (1910) 2388-2403.

[186] E.W. Paul, A.J. Ricco, M.S. Wrighton, "Resistance of Polyaniline Films as a Function of Electrochemical Potential and the Fabrication of Polyaniline-based Microelectronic Devices", J. Phys. Chem., 89 (1985) 1441-1447.

[187] Y. Wei, G.-W. Jang, K.F. Hsueh, E.M. Scherr, A.G. MacDiarmid, A.J. Epstein, "Thermal Transitions and Mechanical Properties of Films of Chemically Prepared Polyaniline", Polymer, 33(2) (1992) 314-322.

[188] A.G. MacDiarmid, A.J. Epstein, "The Concept of Secondary Doping as Applied to Polyaniline", Synthetic Metals, 65 (1994), 103-116.

[189] A.G. MacDiarmid, A.J. Epstein, "Secondary Doping in Polyaniline", Synthetic Metals, 69 (1995) 85-92.

[190] W. Zheng, A.G. MacDiarmid, "Conformational Effects in Doped Polyaniline: Protonation of Amine and Imine Sites vs. Protonation of Only the Imine Sites", Polym. Prepr., 36(2) (1995) 73-74.

[191] J.P. Travers. M. Nechtschein, "Water Effects in Polyaniline; A New Conduction Process", Synthetic Metals, 21 (1987) 135-141.

[192] M. Nechtschein, C. Santier, J.P. Travers, J. Chroboczek, A. Alix, M. Ripert, "Water Effects on Polyaniline: NMR and Transport Studies", Synthetic Metals, 18 (1987) 311-316.

[193] A. Alix, V. Lemoine, M. Nechtschein, J.P. Travers, C. Menardo, "Water Absorption Study in Polayniline", Synthetic Metals 29 (1989) E457-E462.

[194] M. Angelopoulos, A. Ray, A.G. MacDiarmid, A.J. Epstein, "Polyaniline: Processing from Aqueous Solutions and Effect of Water Vapor on Conductivity", Synthetic Metals, 21 (1987) 21-30.

[195] S.P. Armes, M. Aldissi, S. Agnew, S. Gottesfeld, "Synthesis and Characterization of Aqueous Colloidal Dispersions of Poly (Vinyl Alcohol) / Polyaniline Particles", Mol. Cryst. Liq. Cryst., 190 (1990) 63-74.

[196] K. Ogura, M. Kokura, M. Nakayama, "A Conductive and Humidity Sensitive Composite Film Derived from Poly (o-Phenilenediamine) and Poly (Vinyl Alcohol)", J. Electrochem. Soc., 142(9) (1995) 152-153.

[197] K. Ogura, H. Shiigi, M. Nakayama, "A New Humidity Sensor Using Composite Film Derived from Poly (o-Phenilenediamine) and Poly (Vinyl Alcohol)", J. Electrochem. Soc., 143(9) (1996) 2925-2930.

[198] K. Ogura, H. Shiigi, M. Nakayama, A. Fujii, "Thermogravimetric/Mass and Infrared Spectroscopic Properties and Humidity Sensitivity of Polyaniline Derivatives / Poly (Vinyl Alcohol) Composites", J. Electrochem. Soc., 145(10) (1998) 3351-3357.

[199] K. Ogura, T. Saino, M. Nakayama, H. Shiigi, "The Humidity Dependence of the Electrical Conductivity of a Soluble Polyaniline-Poly (Vinyl Alcohol) Composite Film", J. Mater Chem., 7(12) (1997) 2363-2366.

[200] S.A. Chen, W.G. Fang, "Electrical Conductive Polyaniline-Poly (Vinyl Alcohol) Composite Films: Physical Properties and Morphological Structures", Macromolecules, 24 (1991) 1242-1248.

[201] T. Nagaoka, H. Nakao, T. Suyama, K. Ogura, "Polyaniline-Poly (Vinyl Alcohol) Dispersions for Controlled Ion Exchange of Organic Sulfonates", Analyst, 122 (1997) 1399-1404.

[202] H. Nakao, T. Nagaoka, K. Ogura, "Ion-Exchange Ability of Polyaniline-Poly (Vinyl Alcohol) Colloids with Various Anions", Analytical Sciences, 13 (1997) 327-331

[203] J. Stejskal, P. Kratochvil, "Polayniline Dispersions 5. Poly (Vinyl Alcohol) and Poly (N-Vinyl Pyrrolidone) as Steric Stabilizers", Langmuir, 12 (1996) 3389-3392.

[204] J. Stejskal, M. Spirkova, P. Kratochvil, "Polyaniline Dispersions 4. Polymerization Seeded by Polyaniline Particles", Acta Polymer., 45 (1994) 385-388.

[205] Y. Cao, P. Smith, A.J. Heeger, "Counter-ion Induced Processibility of Conducting Polyaniline", Synthetic Metals, 55-57 (1993) 3514-3519.

[206] M.E. Jozefowicz. , R. Laversanne, H.H.S. Javadi, A.J. Epstein, J.P. Pouget, X. Tang, A.G. MacDiarmid, "Multiple Lattice Phases and Polaron-Lattice-Spinless-Defect Competitions in Polyaniline", Phys. Rev. B, 39(17) (1989) 12958-12961.

[207] H.H.S. Javadi, M. Angelopoulos, A.G. MacDiarmid, A.J. Epstein, "Conduction Mechanism of Polyaniline: Effect of Moisture", Synthetic Metals, 26 (1988)1-8.

[208] F. Zuo, M. Angelopoulos, A.G. MacDiarmid, A.J. Epstein, "A.C. Conductivity of Emeraldine Polymer ", Phys. Rev B, 39(6) (1989) 3570-3578.

[209] J. R. Macdonald, W.B. Johnson, in: J. Ross Macdonald (Ed.), Impedance Spectroscopy Emphasizing Solid Materials and Systems, John Wiley and Sons, New York, 1987, pp. 16.

[210] A. Revzin, R.G. Tompkins, M. Toner, "Surface Engineering with Poly(ethylene glycol) Photolithography to Create High-Density Cell Arrays on Glass", Langmuir, 19 (2002) 9855-9862.

[211] M.A.M.J. van Zandvoort, D.L.J. Vossen, G. van Ginkel, R. Torre, P. Bartolini, M. Ricci, J. Thomas-Oates, H. Zuilhof, "Spectral Characterization of Fluorescent 5-Iodoacetamidotetramethylrhodamine and its N-Acetylcysteine Derivative", Phys. Chem. Chem. Phys., 1 (1999) 4571-4582.

[212] W. Zheng, M. Angelopoulos, A.J. Epstein, A.G. MacDiarmid, "Concentration Dependence of Aggregation of Polyaniline in NMP Solutions of Resulting Cast Films", Macromolecules, 30 (1997) 7634-7637.

[213] J. Tang, X. Jing, B. Wang, F. Wang, "Infrared Spectra of Soluble Polyaniline", Synthetic Metals 24 (1988) 231-238.

[214] L. Ding, X. Wang, R.V. Gregory, "Thermal Properties of Chemical Synthesized Polyaniline (EB) Powder", Synthetic Metals, 104 (1999) 73-78.

[215] S.A. Chen, H.T. Lee, "Polyaniline Plasticized with 1-Methyl–2-Pyrrolidone: Structure and Doping Behavior", Macromolecules, 26 (1993) 3254-3261.

[216] W. Zheng, M. Angelopoulos, A.J. Epstein, A.G. MacDiarmid, "Experimental Evidence for Hydrogen Bonding in Polyaniline: Mechanism of Aggregate Formation and Dependency on Oxidation State", Macromolecules, 30 (1997) 2953-2955.

[217] M. Angelopoulos, R. Dipietro, W.G. Zheng, A.G. MacDiarmid, "Effect of Selected Processing Parameters on Solution Properties and Morphology of Polyaniline and Impact on Conductivity", Synthetic Metals, 84 (1997) 35-39.

[218] R. Mathew, B.R. Mattes, M.P. Espe, "A Solid NMR Characterization of Cross-Linked Polyaniline Powder", Synthetic Metals, 131 (2002) 141-147.

[219] R. Mathew, D. Yang, B.R. Mattes, M.P. Espe, "Effect of Elevated Temperature on the Reactivity and Structure of Polyaniline", Macromolecules, 35 (2002) 7575-7581.

[220] E.J. Oh, Y. Min, J.M. Weisinger, S.K. Manohar, E.M. Scherr, P.J. Prest, A.G. MacDiarmid, A.J. Epstein, "Polyaniline: Dependency of Selected Properties on Molecular Weight", Synthetic Metals, 55-57 (1993) 977-982.

[221] A.J. Milton, A.P. Monkman, "A Comparative Study of Polyaniline Films Using Thermal Analyses and IR Spectroscopy", J. Phys. D, Appl. Phys. 26 (1993) 1468-1474.

[222] J.P. Pouget, M.E. Jozefowicz, A.J. Epstein, X. Tang, A.G. MacDiarmid, "X-ray Structure of Polyaniline", Macromolecules, 24 (1991) 779-789.

[223] J.P. Pouget, M. Laridjiani, M.E. Jozefowicz, A.J. Epstein, E.M. Scherr, A.G. MacDiarmid, "Structural Aspects of the Polyaniline Family of Electronic Polymers", Synthetic Metals, 51 (1992) 95-101.

[224] M.E. Jozefowicz, A.J. Epstein, J.P. Pouget, J.G. Masters, A. Ray, Y. Sun, X. Tang, A.G. MacDiarmid, "X-Ray Structure of Polyanilines", Synthetic Metals, 41-43 (1991) 723-726.

[225] L.F. Warren, J.A. Walker, D.P. Anderson, C.G. Rhodes, L.J. Buckley, "A Study of Conducting Polymer Morphology", J. Electrochem. Soc., 136 (1989) 2286-2295.

[226] S. M. Long, K.R. Brennan, A. Saprigin, R.S. Kohlman, A.J. Epstein, M. Angelopoulos, S.L. Buchwalter, A. Rossi, W. Zheng, A.G. MacDiarmid, "Aggregation and Interchain "Self" Doping in Emeraldine Base", Synthetic Metals, 84 (1997) 809-810.

[227] J.Y. Shimano, A.G. MacDiarmid, "Phase Segregation in Polyaniline: A Dynamic Block Copolymer", Synthetic Metals, 119 (2001) 365-366.

[228] J.Y. Shimano, A.G. MacDiarmid, "Polyaniline, a Dynamic Block Copolymer: Key to Attaining its Intrinsic Conductivity?", Synthetic Metals, 123 (2001) 251-262.

[229] Y.M. Lee, J.H. Kim, J.S. Kang, S.Y. Ha, "Annealing Effects of Dilute Polyaniline/NMP Solution", Macromolecules, 33 (2000) 7431-7439.

[230] M.E. Jozefowicz, A.J. Epstein, J.P. Pouget, J.G. Masters, A. Ray, A.G. MacDiarmid, "X-Ray Structure of the Polyaniline Derivative Poly(o-toluidine): The Structural Origin of Charge Localization", Macromolecules., 24 (1991) 5863-5866.

[231] S.A. Chen, K.-R. Chuang, C.-I. Chao, H.-T. Lee, "White-Light Emission from Electroluminescence Diode with Polyaniline as the Emitting Layer", Synthetic Metals, 82(3) (1996) 207-210.

[232] M. Wan, J.J. Yang, "Mechanism of Proton Doping in Polyaniline", Appl. Polym. Sci., 55 (1995) 399-405.

[233] A.J. Epstein, A.G. MacDiarmid "Novel Concepts in Electronic Polymers: Polyaniline and its Derivatives", Makromol. Chem, Macromol. Symp., 51 (1991) 217-234.

[234] M.E. Jozefowicz, A.J. Epstein, X. Tang, "Protonic Acid Doping of Two Classes of the Emeraldine Form of Polyaniline", Synthetic Metals, 46 (1992) 336-337.

[235] H. Reiss, "Theoretical Analysis of Protonic Acid Doping of the Emeraldine Form of Polayniline", J. Phys. Chem., 92 (1988) 3657-3662.

[236] H. Reiss, "Note on the Theory of Protonic Acid Doping of Polyaniline", Synthetic Metals, 30 (1989) 257-263.

[237] J. Hammerschmidt, "Studies of Polyvinyl Alcohol under Temperature and Humidity Control", University of Minnesota.

[238] E. Creutz, R.R. Wilson, "Absorption of Water by Films of Cellophane and Polyvinyl Alcohol", J. Chem. Phys., 14(12) (1946) 725-728.

[239] J. Tang, X. Jing, B. Wang, F. Wang, "Infrared Spectra of Soluble Polyaniline", Synthetic Metals, 24 (1988) 231-238.

6. APPENDIX

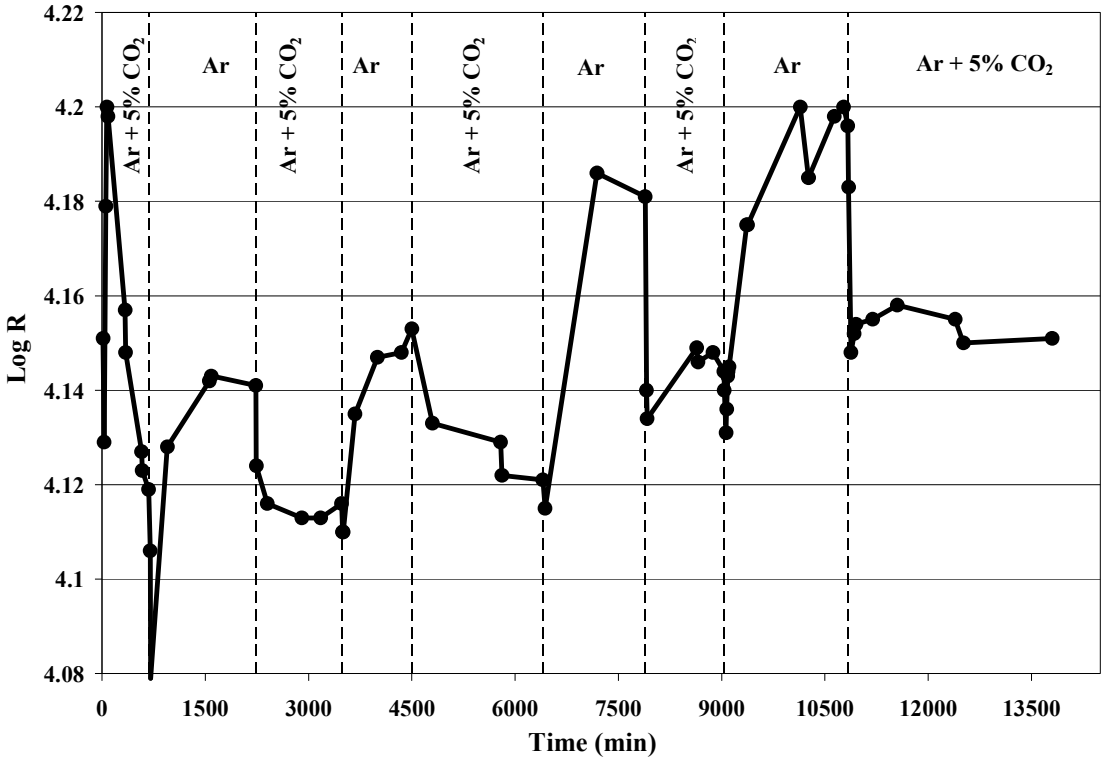

Figure 21a. Time variation of the resistance of the composite film in Ar and Ar + 5% CO_2 in a fixed humidity level given by the supersaturated solution of NaCl in water (RH ≅ 60%)-cycle 2 in table 4.

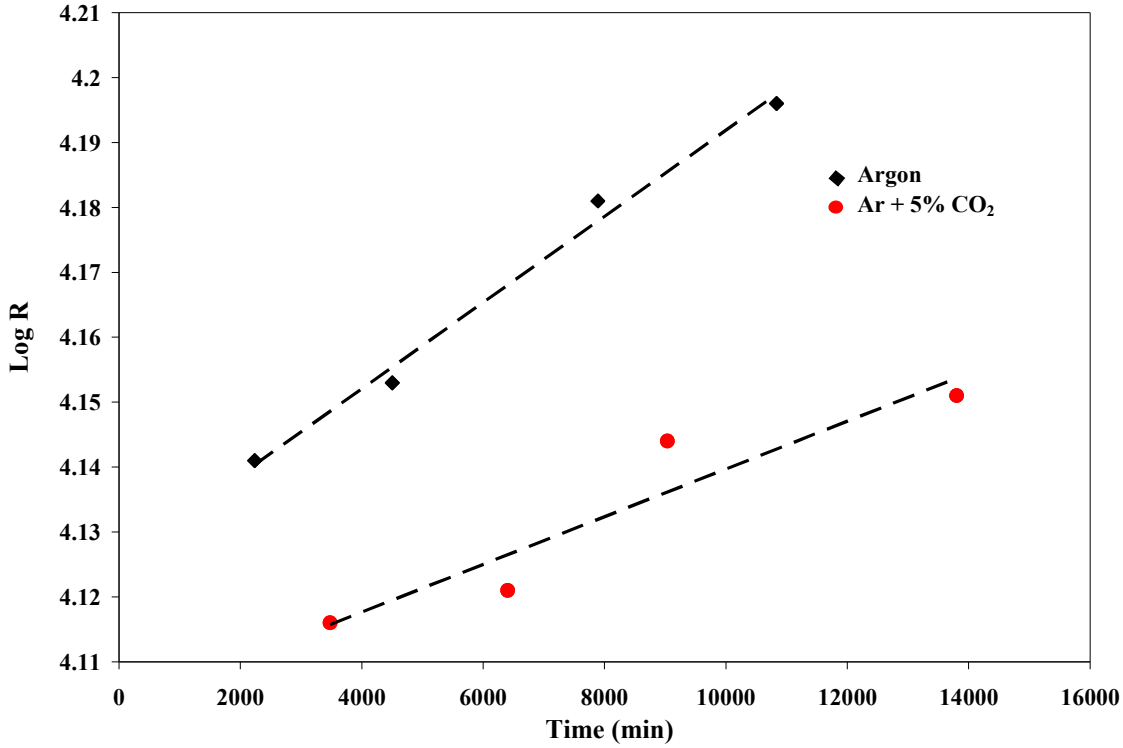

Figure 22a. Trend of the resistance response of the composite film in Ar and Ar + 5% CO_2 at a fixed humidity level given by the supersaturated solution of NaCl in water RH ≅ 60%-cycle 2 in table 4.

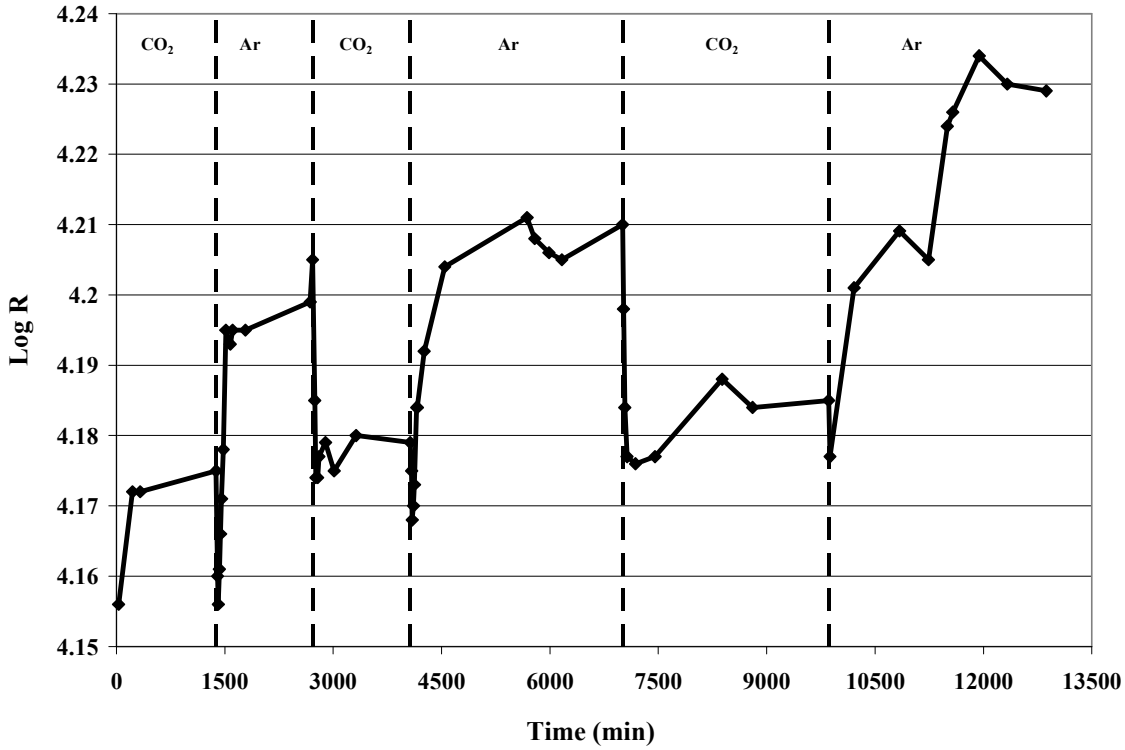

Figure 21b. Time variation of the resistance of the composite film in Ar and Ar + 5% CO_2 in a fixed humidity level given by the supersaturated solution of $MgCl_2$ in water (RH ≅ 30%)-cycle 3 in table 4.

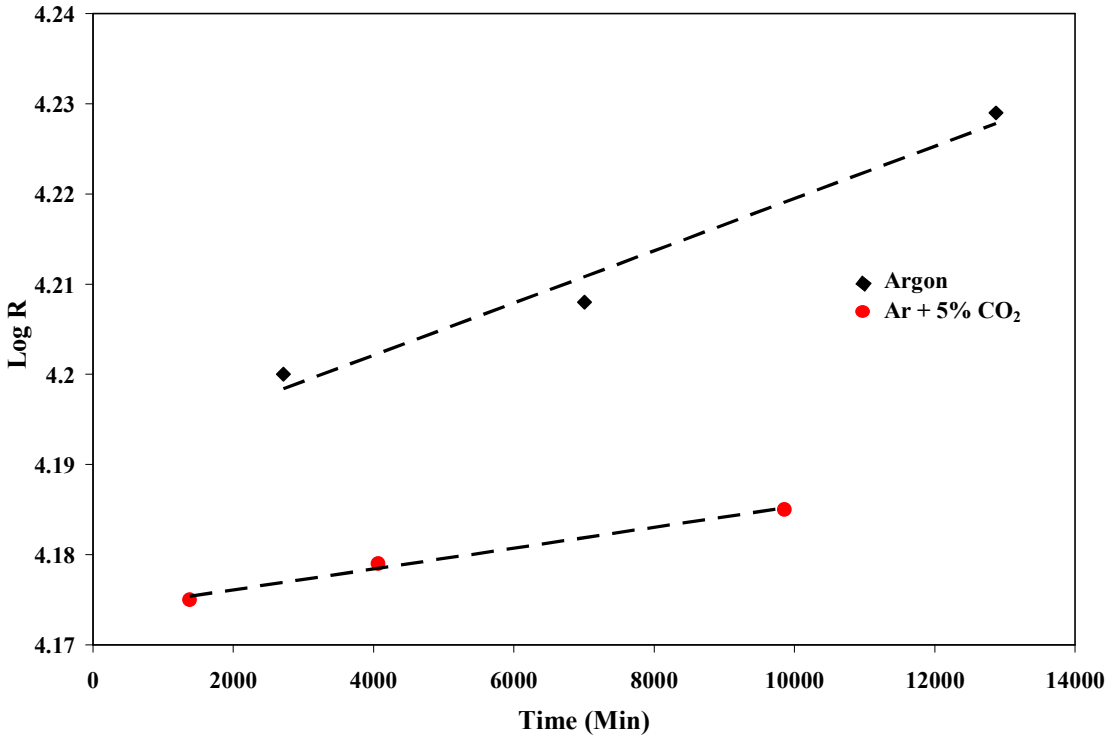

Figure 22b. Trend of the resistance response of the composite film in Ar and Ar + 5% CO_2 at a fixed humidity level given by the supersaturated solution of $MgCl_2$ in water (RH ≅ 30%)-cycle 3 in table 4.

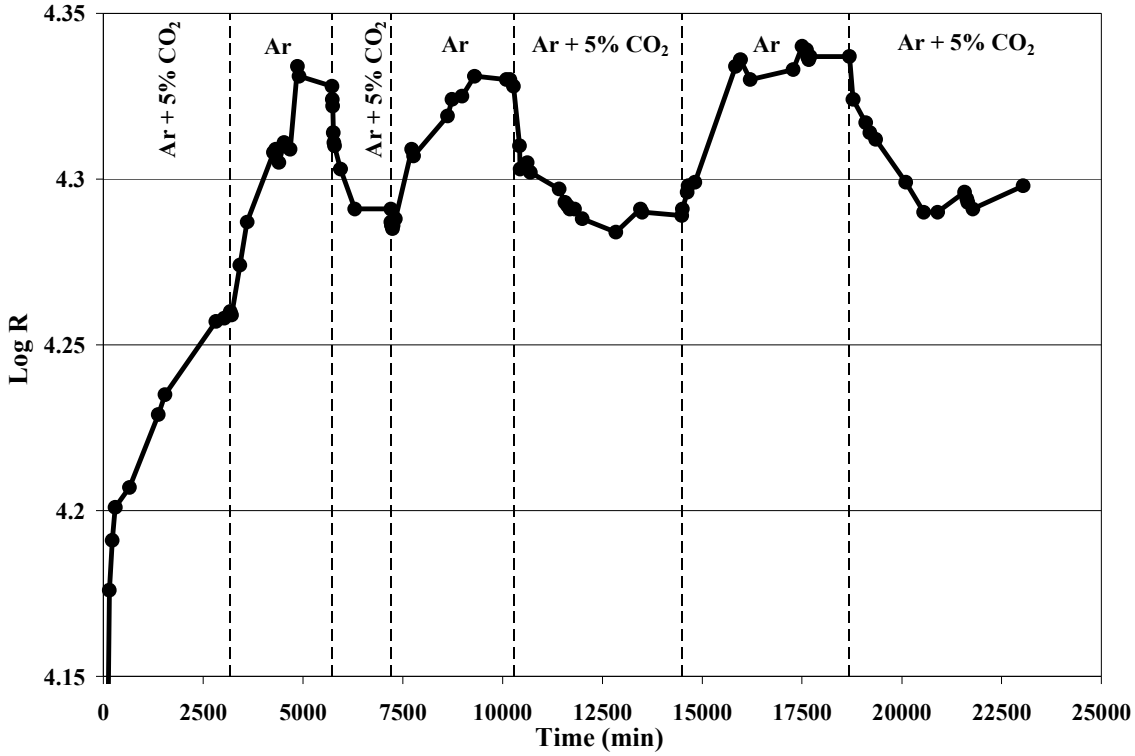

Figure 21c. Time variation of the resistance of the composite film in Ar and Ar + 5% CO_2 in a fixed humidity level given by the supersaturated solution of LiCl in water (RH ≅ 4.5%)-cycle 4 in table 4.

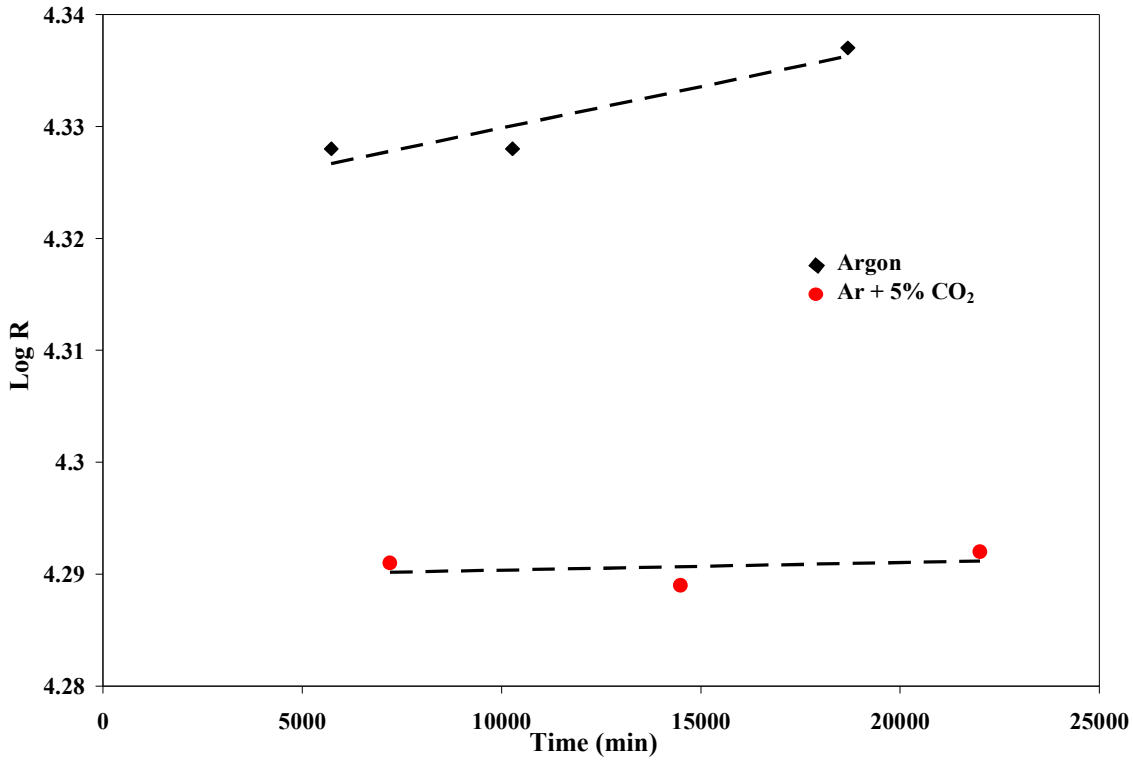

Figure 22c. Trend of the resistance response of the composite film in Ar and Ar + 5% CO_2 at a fixed humidity level given by the supersaturated solution of LiCl in water (RH ≅ 4.5%)-cycle 4 in table 4.

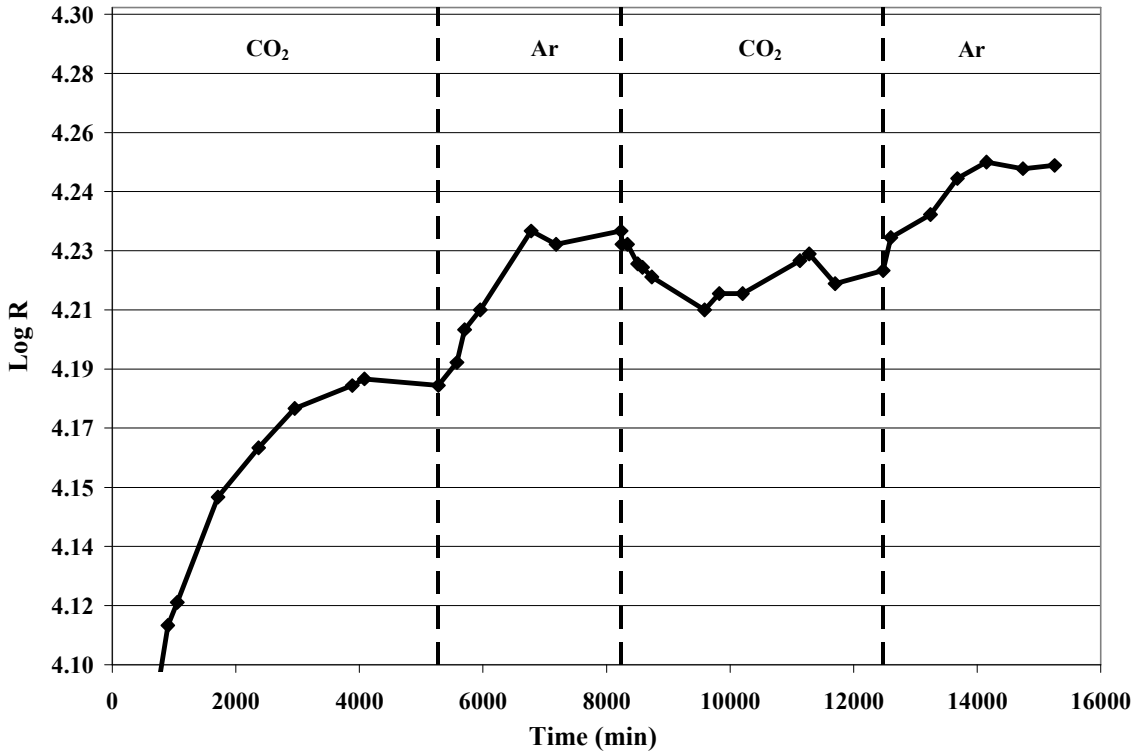

Figure 21d. Time variation of the resistance of the composite film in Ar and Ar + 5% CO_2 in a fixed humidity level given by the supersaturated solution of LiBr in water (RH ≅ 1.5%)-cycle 5 in table 4.

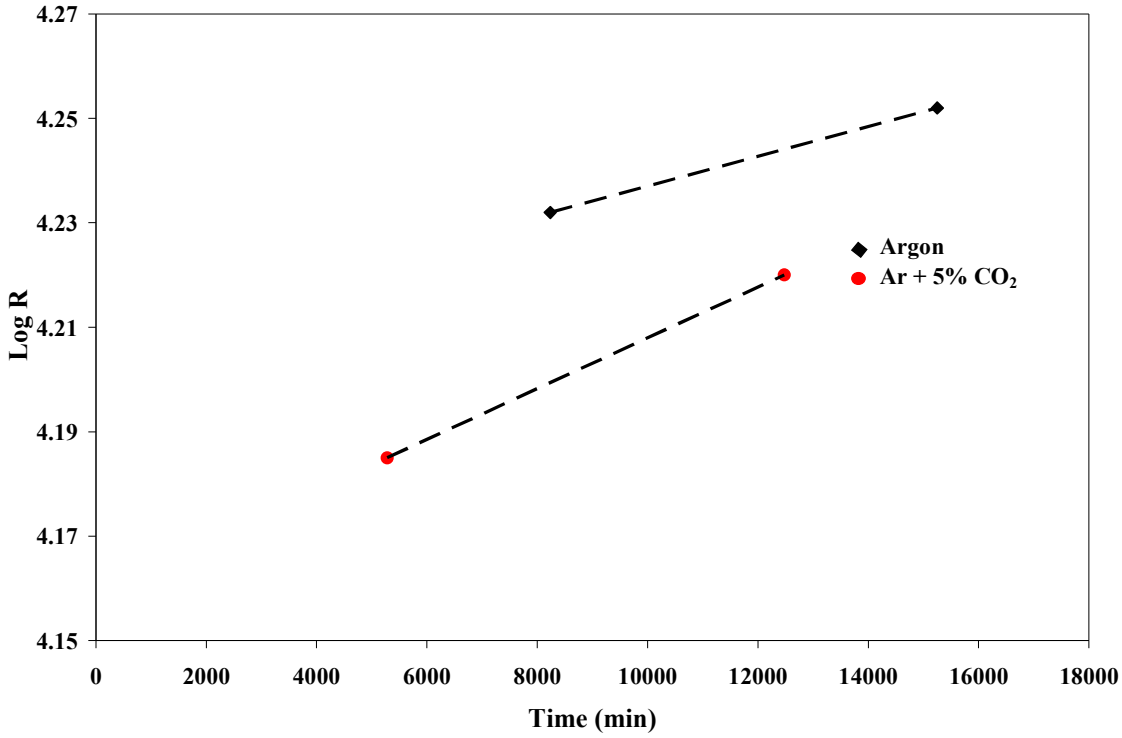

Figure 22d. Trend of the resistance response of the composite film in Ar and Ar + 5% CO_2 at a fixed humidity level given by the supersaturated solution of LiBr in water (RH ≅ 1.5%)-cycle 5 in table 4.

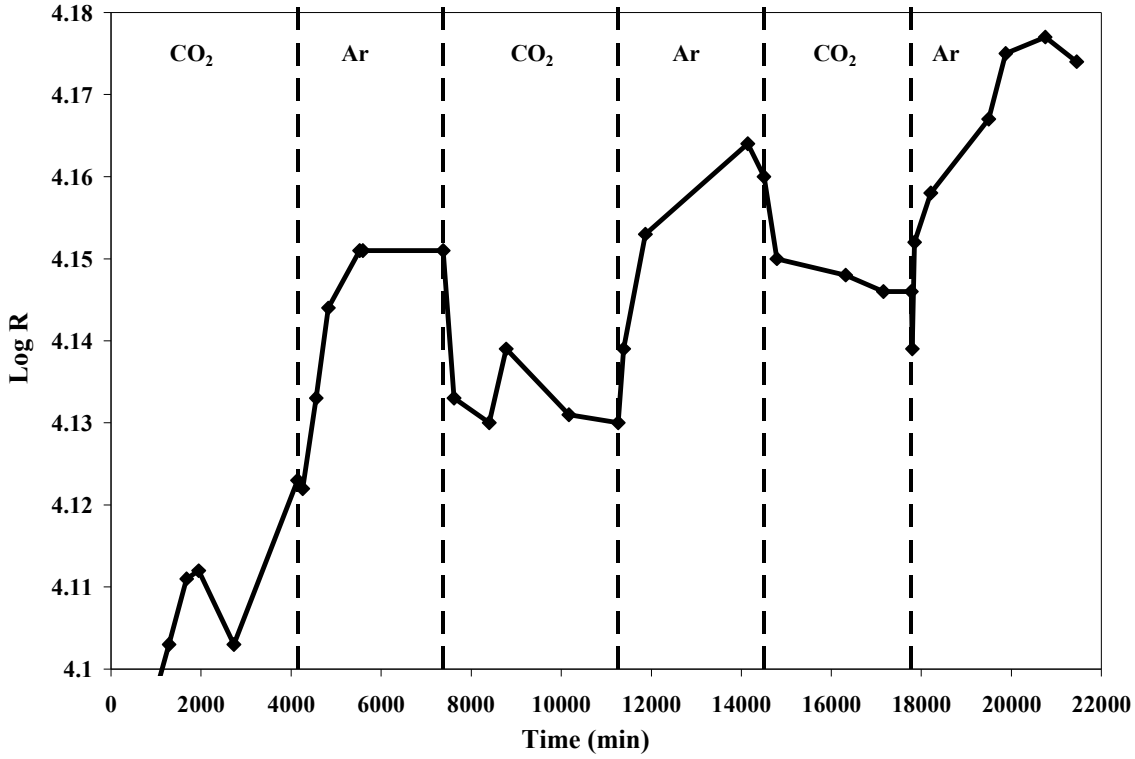

Figure 21e. Time variation of the resistance of the composite film in Ar and Ar + 5% CO_2 in a fixed humidity level given by the supersaturated solution of $MgCl_2$ in water (RH ≅ 30%)-cycle 6 in table 4.

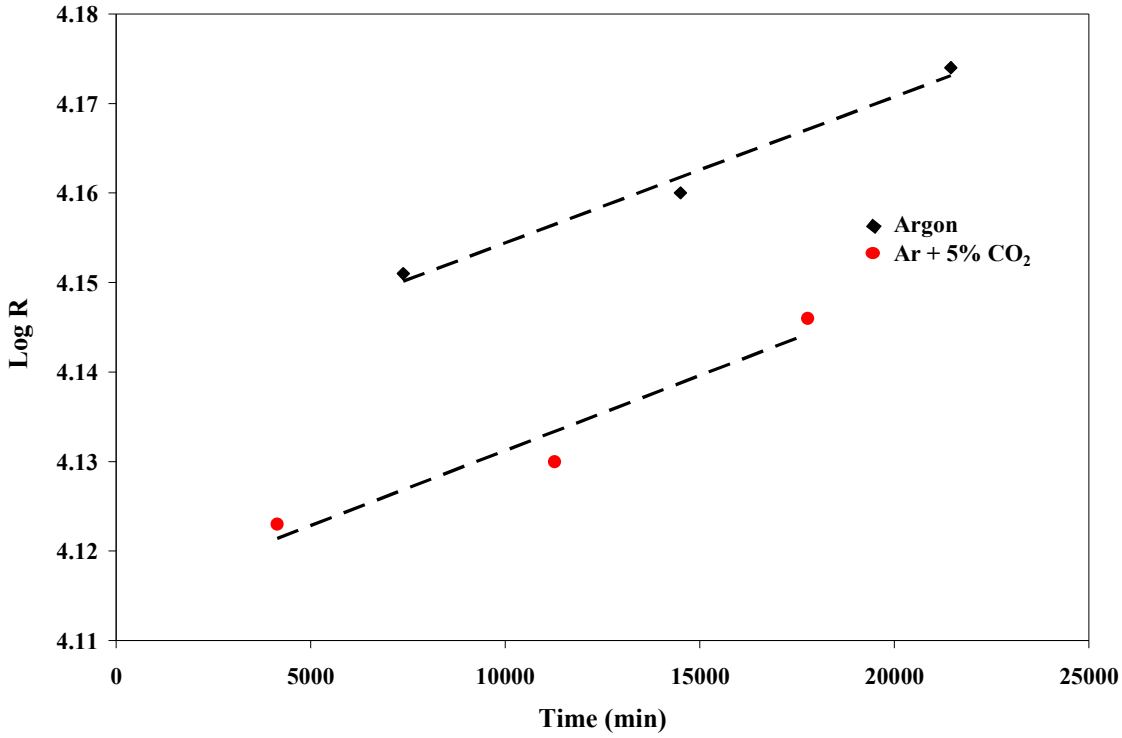

Figure 22e. Time variation of the resistance of the composite film in Ar and Ar + 5% CO_2 in a fixed humidity level given by the supersaturated solution of $MgCl_2$ in water (RH ≅ 30%)-cycle 6 in table 4.

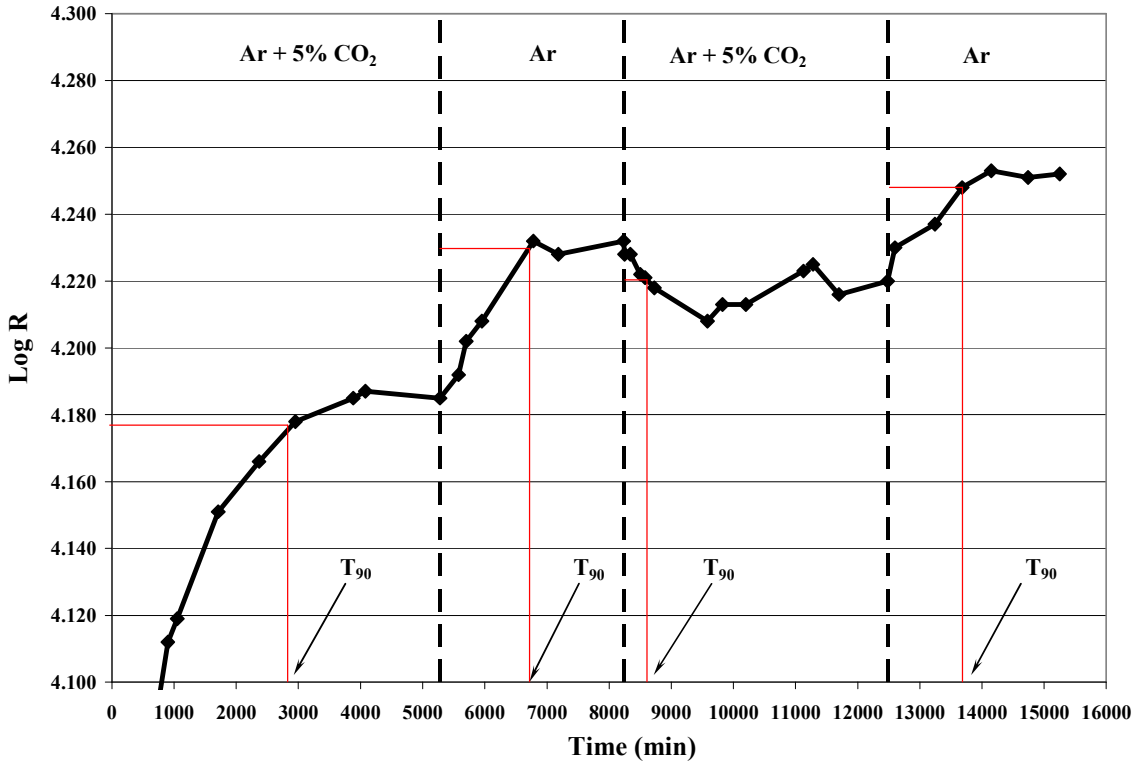

Figure 25a. Example of t_{90} estimation-cycle 5 in table 4.

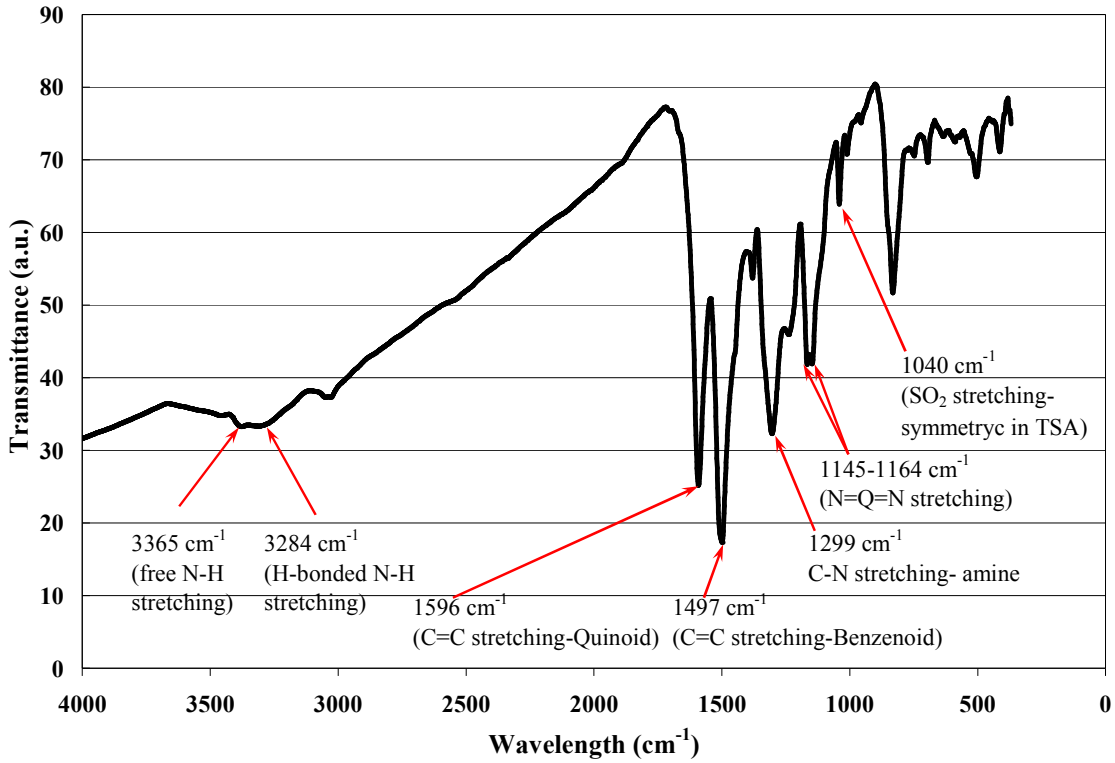

Figure 26a. FTIR spectra for an Emeraldine Base treated at 100°C for 1 hour in helium atmosphere.

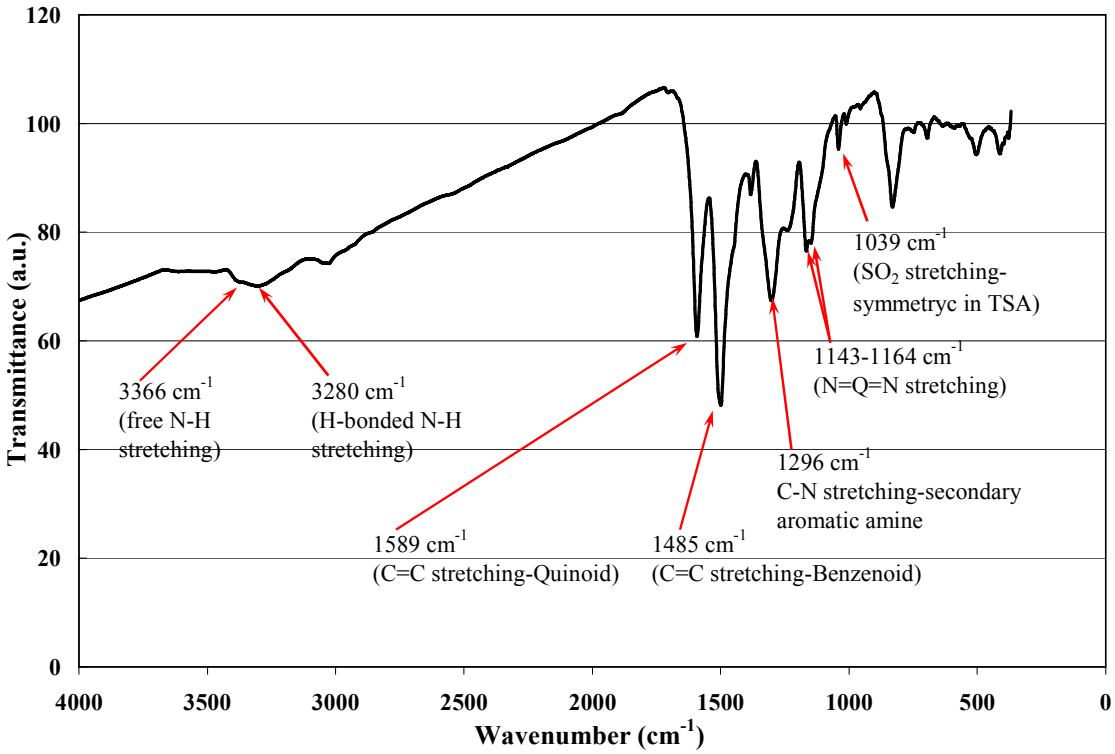

Figure 26b. FTIR spectra for an Emeraldine Base treated at 150°C for 1 hour in helium atmosphere.

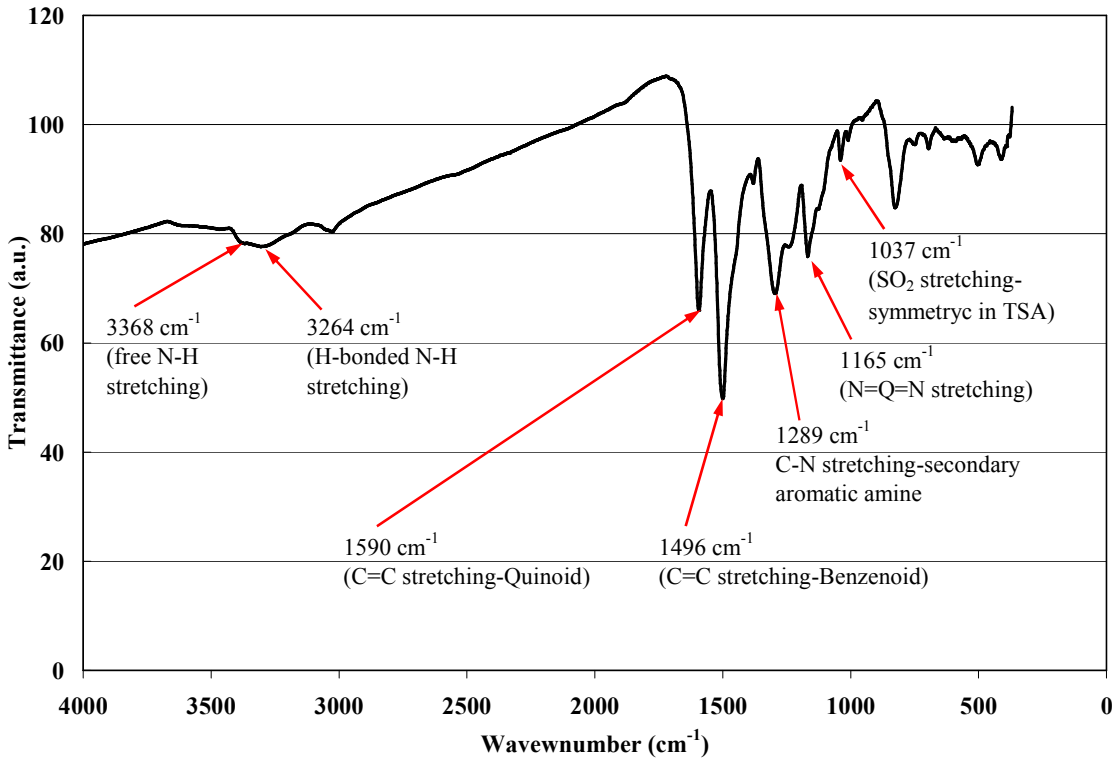

Figure 26c. FTIR spectra for an Emeraldine Base treated at 200°C for 1 hour in helium atmosphere.

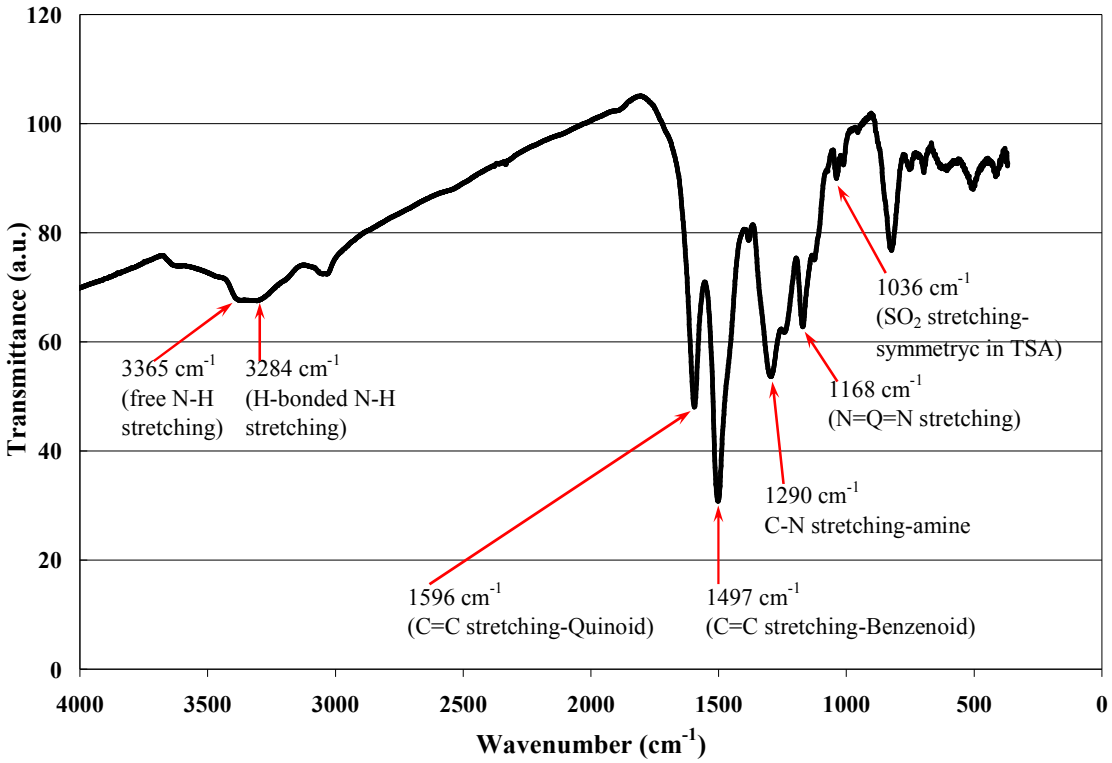

Figure 26d. FTIR spectra for an Emeraldine Base treated at 250°C for 1 hour in helium atmosphere.

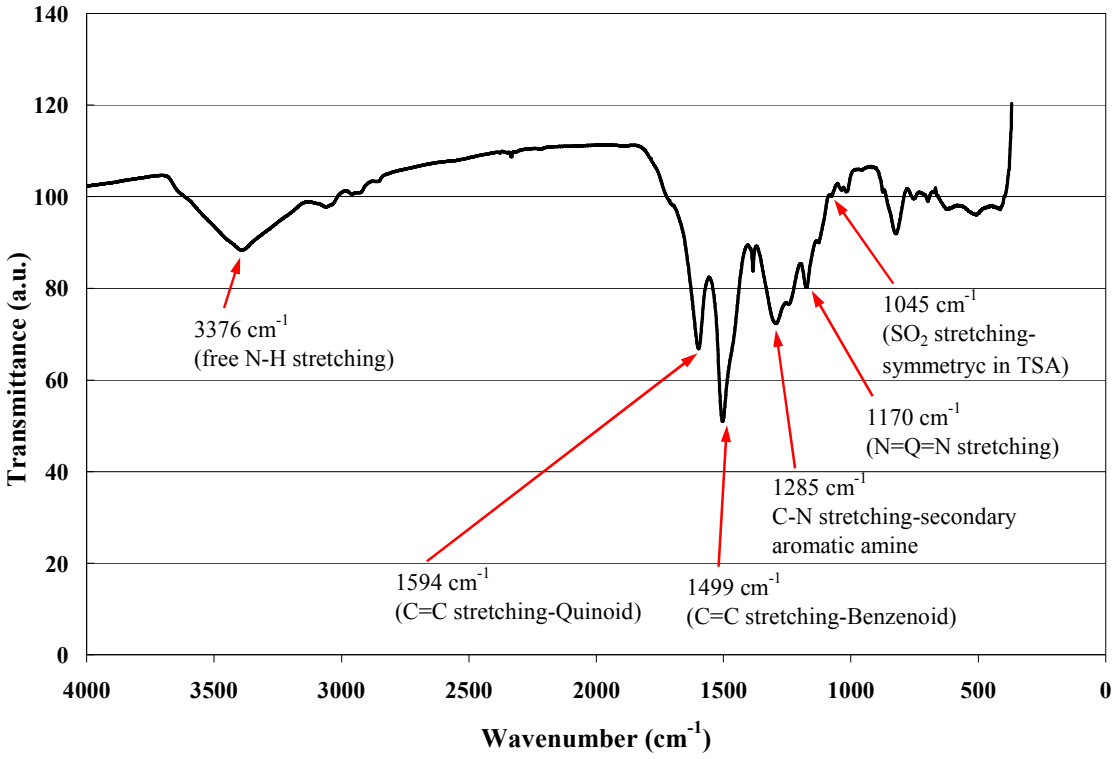

Figure 26e. FTIR spectra for an Emeraldine Base treated at 300°C for 1 hour in helium atmosphere.

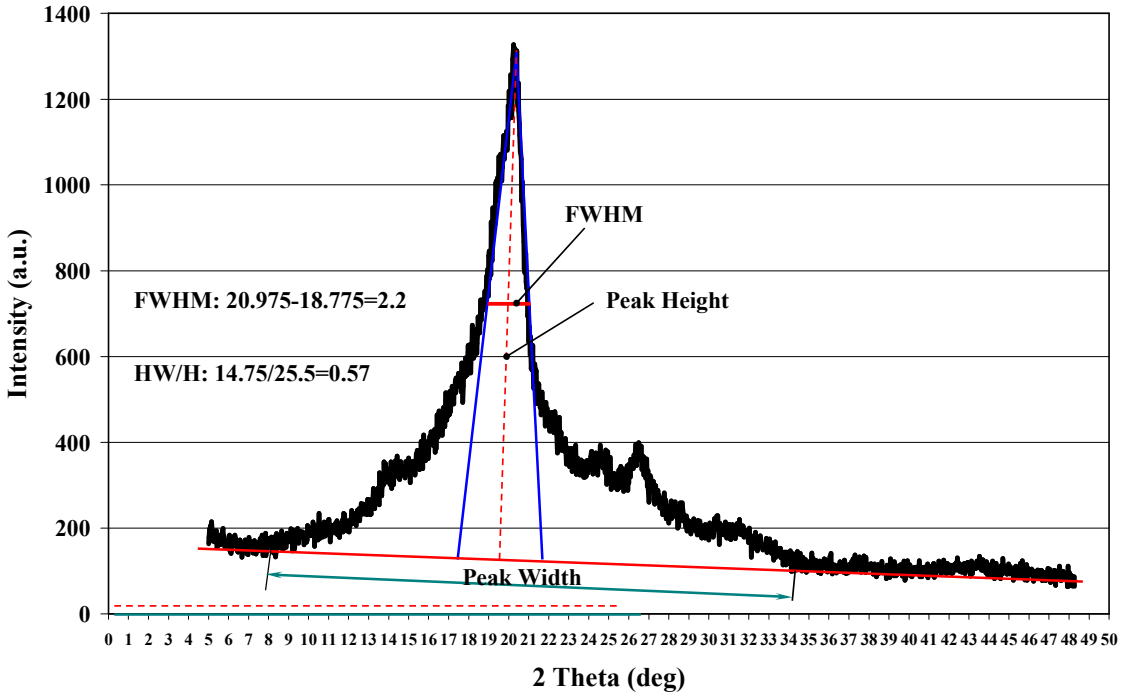

Figure 29a. Method of calculating the FWHM and HW/H for an XRD pattern of emeraldine base powder heat treated at 100ºC.

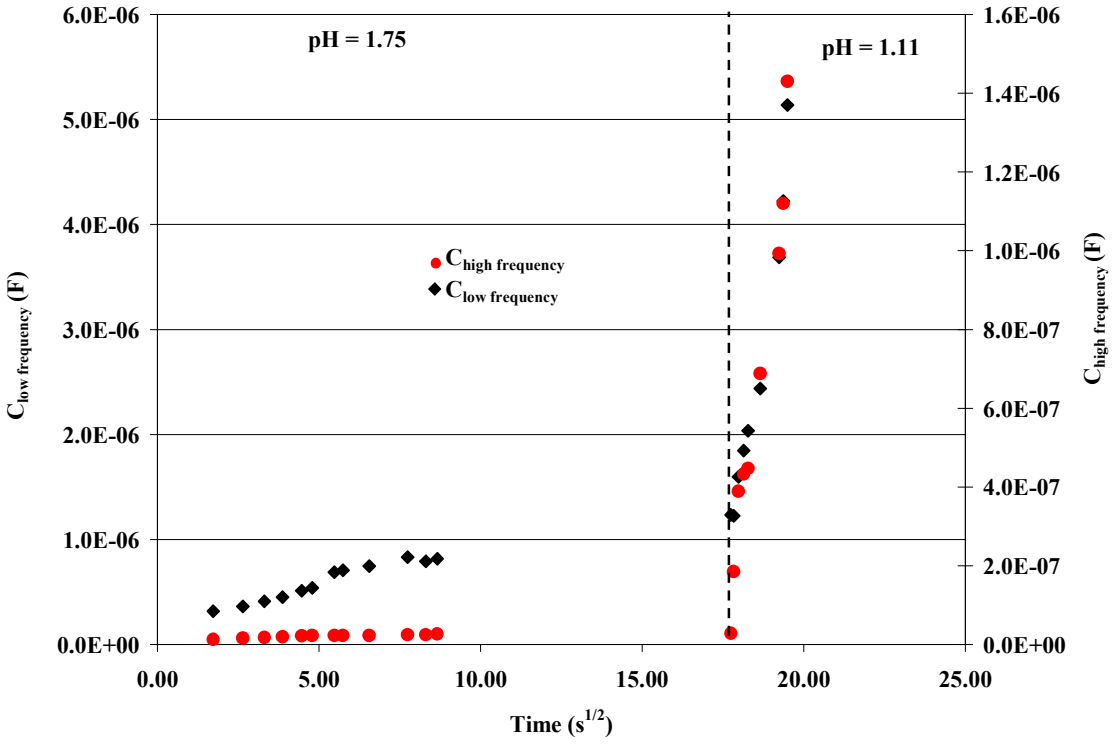

Figure 43a. Capacitance vs. time in pH = 1.75 and pH = 1.11.

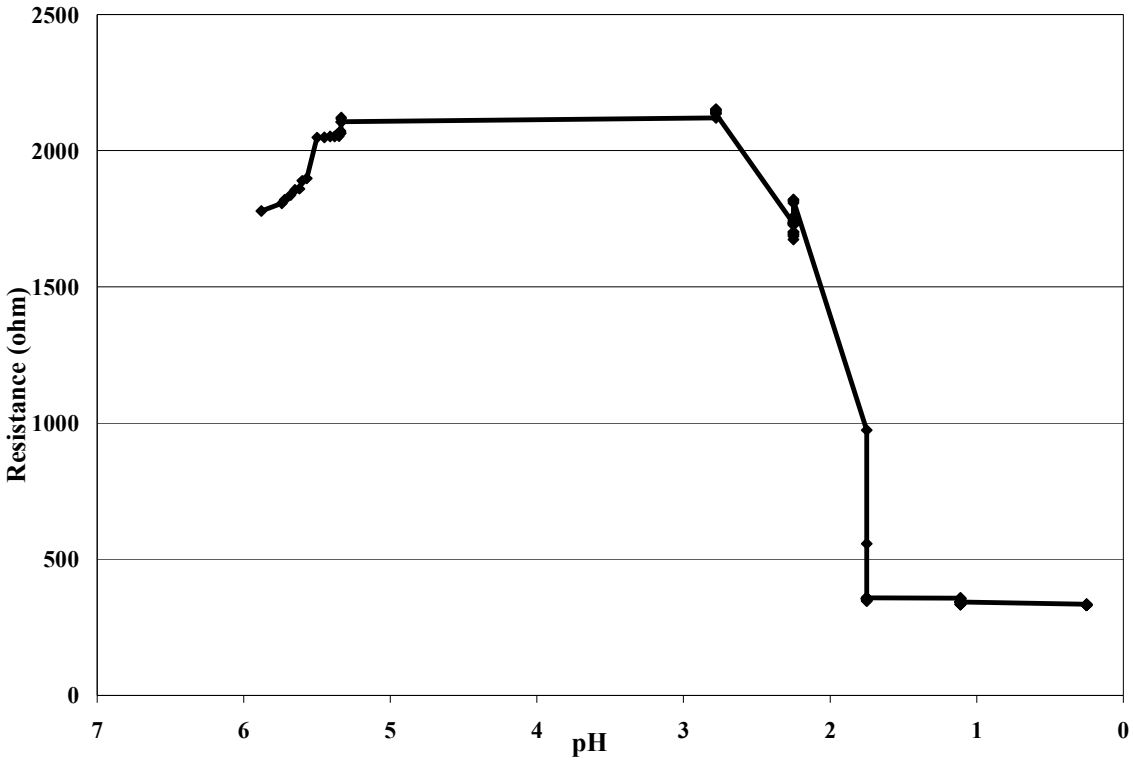

Figure 43b. Total resistance of emeraldine base thin film vs. pH in aqueous HCl solutions.